Towards a systematic study of $\{D_1, D_2\}$–$\{D, D^*\}$ scattering and exotic vector states

Dissertation

zur
Erlangung des Doktorgrades (Dr. rer. nat.)

der
Mathematisch-Naturwissenschaftlichen Fakultät

der
Rheinischen Friedrich-Wilhelms-Universität Bonn

vorgelegt von
Leon Alexander von Detten
aus
Dernbach

Bonn, Mai 2024

Angefertigt mit Genehmigung der Mathematisch-Naturwissenschaftlichen Fakultät
der Rheinischen Friedrich-Wilhelms-Universität Bonn

Gutachter 1:	Professor Dr. Christoph Hanhart
Gutachter 2:	Professor Dr. Dr. h.c. Ulf-G. Meißner

Tag der Promotion:	13.06.2024
Erscheinugsjahr:	2024

Abstract

As one of the four known fundamental forces in nature, the strong interaction is crucial for the formation of matter. Established in the early 1970s, the underlying field theory of quantum chromodynamics is embedded in our current Standard Model of particle physics, describing the strong interaction between quarks and gluons. However, due to its non-perturbative nature at low momentum transfer, we nowadays face a wide range of phenomena that still need to be understood.

Especially in recent years, various collider experiments reported numerous states that show properties inconsistent with quark-model predictions. So far there exists not only significant tension between the parameters extracted from different exclusive measurements for these so-called exotic states, but there is in some cases even no consensus on the actual number of states that contribute. One reason for this is that the experimental data are analyzed for the channels individually and parameterized by a simple sum of Breit-Wigner functions - in particular omitting relevant threshold effects. In this work, we aim towards a systematic study of the vector states above 4.2 GeV, consistent with the principles of analyticity and unitarity.

The first chapter introduces the theoretical framework relevant to our analyses. In the second chapter, we present our initial study of the energy range from 4.2 to 4.35 GeV, which hosts most predominantly the $Y(4230)$. New data published in 2022 and 2023 clearly highlight the asymmetric lineshape in $J/\psi\pi^+\pi^-$ at the $D_1\bar{D}$ threshold. We demonstrate that the experimental data of eight final states are consistent with the assumption that the $Y(4230)$ is a $D_1\bar{D}$ hadronic molecule. This is achieved by including interference with the well-known conventional charmonium state $\psi(4160)$, as well as taking the relevant thresholds into account.

In the third chapter we lay the foundation to significantly extend the studied energy range. While our first analysis focused solely on the intermediate $D_1\bar{D}$ channel, heavy quark spin symmetry also calls for potential bound states in $D_1\bar{D}^*$ and $D_2\bar{D}^*$. We present the necessary formalism for the future study of the full coupled channel dynamics.

Contents

1. Theoretical foundation

1.1. Standard Model

The Standard Model of particle physics is a quantum field theory describing the fundamental forces of nature [1–3], however, so far excluding gravity. The strong, electromagnetic, and weak interactions are covered by a $\mathrm{SU(3)_c} \otimes \mathrm{SU(2)_L} \otimes \mathrm{U(1)}_Y$ gauge group.

Due to various experiments, there is overwhelming evidence that fermions appear in 3 families [4]. The first generation of leptons consists of electron (e) and electron-neutrino(ν_e), the second of muon (μ) and muon-neutrino (ν_μ), and the third of tauon (τ) and tauon-neutrino (ν_τ). For the quarks they are filled by up- (u) and down- (d), charm- (c) and strange- (s), top- (t) and bottom-quark (b). Moreover, several gauge bosons, corresponding to the generators of the gauge group, need to be introduced to allow for local gauge symmetry. There are 8 gluons (g) for the strong-, the $W^\pm$ and Z boson for the weak- and the photon (γ) for the electromagnetic interaction.

Although the $W^\pm$ and Z bosons are observed experimentally to be massive particles, a corresponding mass term would break the $\mathrm{SU(2)}_L$ symmetry. To avoid this their masses are generated dynamically by the Higgs mechanism, introducing the only scalar field to the Standard Model, the Higgs boson [5]. Coupling to quark and lepton fields via the Yukawa interaction, the Higgs potential has a degenerate minimum with a non-zero vacuum expectation value, such that symmetry gets spontaneously broken. This generates an effective mass of the $W^\pm$ and Z boson, as well as for quarks and leptons.

Observed phenomena like e.g. neutrino oscillations indicate a non-zero mass for neutrinos as well, although the exact mechanism is not known yet [6]. At present the Standard Model Lagrangian has 19 free parameters which numerical values were established by experiments; consisting of 3 lepton masses, 6 quark masses, 3 CKM mixing angles and 1 CP violating phase, 3 gauge couplings for the strong, electromagnetic and weak interaction, as well as the Higgs vacuum expectation value and its mass.

1.2. Quantum Chromodynamics

The field theory describing the strong interaction of quarks and gluons is called quantum chromodynamics (QCD) [3, 7, 8]. The Lagrangian density $\mathcal{L}_{\mathrm{QCD}}$ is constructed from local $\mathrm{SU}(3)_c$ gauge invariance with quarks q^a, antiquarks $\bar{q}^a$ and gluons A^a_μ as degrees of freedom

$$\begin{aligned} \mathcal{L}_{\mathrm{QCD}} &= -\frac{1}{4} G^a_{\mu\nu} G^{a\,\mu\nu} + \bar{q}^a (i \not{D}^{ab} - m_q \delta^{ab}) q^b \\ q &= (u, d, s, c, t, b)^T \\ \bar{q} &= (\bar{u}, \bar{d}, \bar{s}, \bar{c}, \bar{t}, \bar{b}) \,, \end{aligned} \tag{1.1}$$

where a, b denotes the SU(3) flavor index. The interaction with the gauge fields is contained in the covariant derivative

$$D^{ab}_\mu = \partial_\mu \delta^{ab} + i g T_c^{ab} A^c_\mu \,. \tag{1.2}$$

with T_c^{ab} denoting the $\mathrm{SU}(3)_c$ generators in the adjoint representation. $G^a_{\mu\nu}$ denotes the gluon field strength tensor

$$G^a_{\mu\nu} = \partial_\mu A^a_\nu - \partial_\nu A^a_\mu - g f^{abc} A^b_\mu A^c_\nu \,, \tag{1.3}$$

where the structure constants f^{abc} are defined by the algebra $[T_a, T_b] = i f_{abc} T_c$. Quarks and antiquarks transform under the fundamental and anti-fundamental representation

$$\begin{aligned} q \to & U(x) q = \exp\left(-i \phi^a(x) \frac{T_a}{2} \right) q \\ \bar{q} \to & \bar{q} U^\dagger(x) = \bar{q} \exp\left(i \phi^a(x) \frac{T_a}{2} \right) \,. \end{aligned} \tag{1.4}$$

In general there is an additional $\mathrm{SU}(3)_c$ gauge invariant term of mass dimension 4

$$\mathcal{L}^\theta_{\mathrm{QCD}} = \frac{g^2 \theta}{32\pi^2} \epsilon^{\mu\nu\rho\sigma} G^a_{\mu\nu} G^a_{\rho\sigma} \,. \tag{1.5}$$

Due to the Levi-Civita tensor the QCD-θ term $\mathcal{L}^\theta_{\mathrm{QCD}}$ transforms odd under parity, while it is invariant under charge conjugation. This introduces a CP violating term, which has not been observed experimentally, leading to the upper bound $\theta_{\mathrm{QCD}} \leq 2.5 \times 10^{-10}$ [9]. Up to now it is unclear, why its contribution is so small, contradicting the expectations from naturalness. However, for the present work it can be safely neglected and QCD can be assumed to respect CP symmetry.

One of the major differences between QCD and QED occurs in the renormalization of the coupling constants. To one loop, the QCD β-function is given by

$$\beta(g_R) = -\frac{g_R^3}{16\pi^2} \left(\frac{11}{3} C_A - \frac{2}{3} N_F \right) \,, \tag{1.6}$$

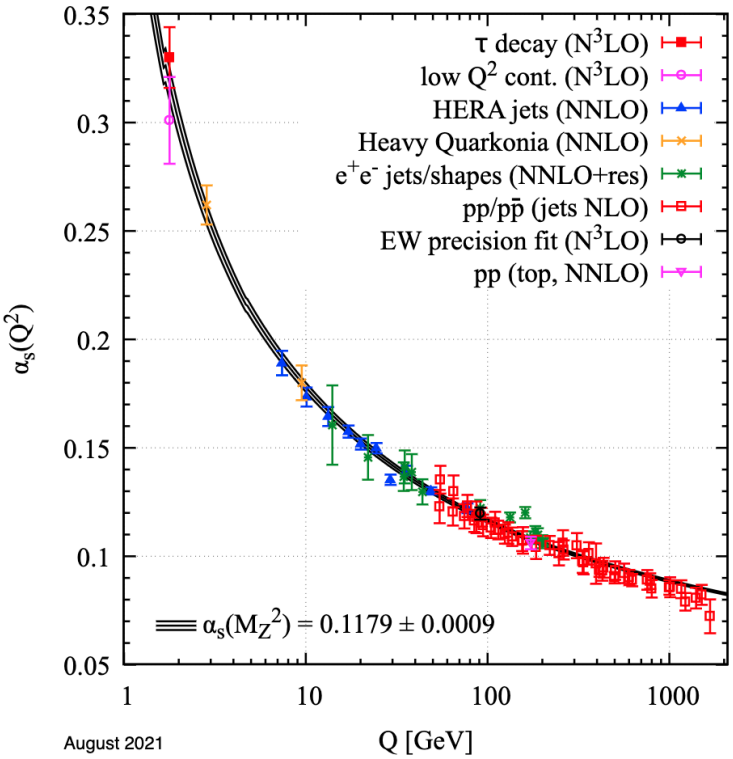

Figure 1.1.: Summary of measurements of α_s as a function of the energy scale Q. Figure taken from Ref. [4].

where $f^{ace}f^{bce} = C_A\delta^{ab} = 3\delta^{ab}$ in QCD and N_F denoting the number of quark flavors. The solution of the resulting renormalization-group equation up to 1-loop can be expressed as

$$\alpha_s(q^2) = \frac{2\pi}{\beta_0}\frac{1}{\log\left(\frac{q^2}{\Lambda_{\mathrm{QCD}}}\right)}, \tag{1.7}$$

with $\beta_0 = 11 - 2N_F/3$. It follows that $\alpha_s(q^2)$ decreases for increasing q^2. This phenomenon is known as asymptotic freedom. Apart from quark masses, which have their origin from the Higgs mechanism, the energy scale $\Lambda_{\mathrm{QCD}} \approx 200$ MeV is the only fundamental parameter of QCD. Hadronic bound states can be classified in terms of irreducible representations of the SU(N_F) group.

1.3. Effective Field Theories of QCD

As formulated by Weinberg in Ref. [10], writing down the most general Lagrangian, containing all terms consistent with the assumed symmetries will result in the most

general S-matrix consistent with analyticity, perturbative unitarity, cluster decomposition and assumed symmetries. The Lagrangian contains an infinite number of operators that need to be arranged by some power counting scheme. Given the characteristic energy scale of hadronic processes $\Lambda_\chi \approx 1$ GeV, the strong interacting quarks can be categorized into two groups. The low energy regime involving the three light quarks with $m_q \ll \Lambda_\chi$, namely up, down and strange, can be described by low-energy effective field theories like Chiral Perturbation Theory [11–16]. From the three remaining quarks with $m_Q > \Lambda_\chi$ the top quark is too heavy and decays before it hadronizes. To perturbatively describe the charm and bottom quarks, which can form metastable hadrons like D and B mesons, one can use Heavy Quark Effective Theory (HQET) by expanding in $\Lambda_{\mathrm{QCD}}/m_c$ or $\Lambda_{\mathrm{QCD}}/m_b$ respectively [17–20].

1.3.1. Chiral Perturbation Theory

Defining the projection operators

$$P_{R/L} = \frac{1}{2}\left(1 \pm \gamma_5\right), \text{ such that } q^{R/L} = P_{R/L} q\,, \tag{1.8}$$

one can decompose the quark fields of the QCD Lagragian into right- and left-handed chiral components

$$L_{\mathrm{QCD}} = -\frac{1}{4} G^a_{\mu\nu} G^{a\,\mu\nu} + \sum_f \quad \bar{q}^R_f i \not{D} q^R_f + \bar{q}^L_f i \not{D} q^L_f - m_f \bar{q}^R_f q^L_f - m_f \bar{q}^L_f q^R_f\,. \tag{1.9}$$

Considering only the light quarks $f = u, d, s$ and working in the limit of vanishing quark masses

$$\mathcal{L}^{m\to 0}_{\mathrm{QCD}} = -\frac{1}{4} G^a_{\mu\nu} G^{a\,\mu\nu} + \sum_f \quad \bar{q}^L_f i \not{D} q^L_f + \bar{q}^R_f i \not{D} q^R_f\,, \tag{1.10}$$

one observes that the right- and left-handed chiral components decouple. In this form, $\mathcal{L}^{m\to 0}_{\mathrm{QCD}}$ is invariant under independent SU(3) flavor rotations as well as U(1) transformations for $q_{R/L}$

$$\vec{q}_{R/L} \mapsto e^{-i\alpha_a^{R/L}\frac{\lambda_a}{2}}\, e^{-i\alpha^{R/L}}\, \vec{q}_{R/L}\,. \tag{1.11}$$

This symmetry group

$$\mathrm{U(3)_L} \otimes \mathrm{U(3)_R} \simeq \mathrm{SU(3)_V} \otimes \mathrm{SU(3)_A} \otimes \mathrm{U(1)_V} \otimes \left(\mathrm{U(1)_A}\right)\,, \tag{1.12}$$

is called *chiral symmetry*. Noether's theorem states that every continuous symmetry of the action is associated with a conserved current

$$j^\mu = \frac{\delta \mathcal{L}}{\delta(\partial^\mu q)} \delta_q \,. \tag{1.13}$$

Here it is convenient to define corresponding vector and axial-vector currents

$$\begin{aligned}
V_a^\mu &= \bar{q}\gamma^\mu \frac{\lambda_a}{2} q, & \partial_\mu V_a^\mu &= i\bar{q}\left[M, \frac{\lambda_a}{2}\right] \\
V^\mu &= \bar{q}\gamma^\mu q, & \partial_\mu V^\mu &= 0 \\
A_a^\mu &= \bar{q}\gamma^\mu\gamma_5 \frac{\lambda_a}{2} q, & \partial_\mu A_a^\mu &= i\bar{q}\left\{M, \frac{\lambda_a}{2}\right\} q \\
A^\mu &= \bar{q}\gamma^\mu\gamma_5 q, & \partial_\mu A^\mu &= 2i\bar{q}\gamma_5 M_q + \frac{N_f g^2}{32\pi^2}\epsilon_{\mu\nu\rho\sigma} G_a^{\mu\nu} G_a^{\rho\sigma} \,,
\end{aligned} \tag{1.14}$$

where $M = \mathrm{diag}(m_u, m_d, m_s)$ denotes the quark mass matrix. While the vector-current V_a^μ is also conserved for all quark masses being equal, for $m_q \to 0$ the first three currents are conserved. However, the singlet vector-current is always broken due to the *axial anomaly* [21]. As no mass-degenerate states of opposite parity are found experimentally and the Vafa-Witten theorem states, that no vector-like symmetry can be broken [22], one needs to assume that only $\mathrm{SU(3)_V}$ instead of $\mathrm{SU(3)_R} \otimes \mathrm{SU(3)_L}$ is approximately realized as a symmetry of hadrons. Therefore, chiral symmetry is spontaneously broken $\mathrm{U(3)_R} \otimes \mathrm{U(3)_L} \mapsto \mathrm{SU(3)}_V \otimes \mathrm{U(1)_V} \otimes \mathrm{U(1)_A}$. As a consequence eight massless Goldstone bosons $\pi^0, \pi^\pm, K^0, \bar{K}^0, K^\pm, \eta_8$ emerge, although the presence of axial anomaly is shifting the mass of the experimentally observed η' upwards. Due to the actual non-vanishing quark masses, chiral symmetry is also explicitly broken, resulting in a non-zero mass of the Goldstone bosons. For now, we assumed that $m_u, m_d, m_s \ll \Lambda_{\mathrm{QCD}}$, however, as $m_s \gg (m_u + m_d)/2$ one observes that the isospin symmetry concerning just u and d works significantly better.

With these considerations one can now establish a field theory with the Goldstone bosons as degrees of freedom. As demonstrated the massless QCD lagrangian is invariant under the compact Lie group $G = \mathrm{U(3)_R} \otimes \mathrm{U(3)_L}$, while we assume that the ground state of our theory is only invariant under a subgroup H of G. Consequently a state ϕ of its Hilbert space $\mathcal{H}$ transforms under a non-linear realization φ of G

$$\varphi(g, \phi) \in \mathcal{H} \,. \tag{1.15}$$

Denoting $\phi = 0$ as the ground state, a requirement on the mapping is that the ground state for all elements in $h \in H = \mathrm{SU}(N)_V$ is mapped onto itself, ie. $\varphi(h, 0) = 0$. However, every other $g \notin H$ generates a non-trivial state $\varphi(g, 0) = \Pi$ that correspond to the Goldstone bosons. So it is sufficient to look at the quotient group G/H as it

is maps isomorphically on the Goldstone bosons. Defining $\tilde{g} = (\tilde{L}, \tilde{R}) \in G$, we want to relate the left coset $\tilde{g}H$ with the SU(N) matrix $U = \tilde{R}\tilde{L}^\dagger$. Multiplying g on the left coset $\tilde{g}H$

$$g\tilde{g}H = (L, R\tilde{R}\tilde{L}^\dagger)H = (\mathbb{1}, R\tilde{R}\tilde{L}^\dagger L^\dagger)(L, L)H = (\mathbb{1}, R(\tilde{R}\tilde{L}^\dagger)L^\dagger)\,, \tag{1.16}$$

we find that the representative of the transformed coset is $(\mathbb{1}, R\tilde{R}\tilde{L}^\dagger L^\dagger)$. Therefore U must transform under

$$U = \tilde{R}\tilde{L}^\dagger \mapsto U' = R(\tilde{R}\tilde{L}^\dagger)L^\dagger\,. \tag{1.17}$$

A possible realization is given by

$$\begin{aligned} U =& \exp\left(i\frac{\sqrt{2}\Phi}{f_\pi}\right) \\ \Phi =& \begin{pmatrix} \frac{\pi^0}{\sqrt{2}} + \frac{\eta_8}{\sqrt{6}} & \pi^+ & K^+ \\ \pi^- & -\frac{\pi^0}{\sqrt{2}} + \frac{\eta_8}{\sqrt{6}} & K^0 \\ K^- & \bar{K}^0 & -\frac{2\eta_8}{\sqrt{6}} \end{pmatrix}, \end{aligned} \tag{1.18}$$

with $f_\pi = 92$ MeV denoting the pion decay constant in the chiral limit. In order to establish a proper field theory one needs to introduce a power counting to characterize the importance of different terms. As the momenta of the Goldstone bosons are small in comparison to the hadronic scale Λ_χ, an expansion in orders of p_Φ/Λ_χ is sensible. Due to Lorentz symmetry only terms even in the momenta will contribute to a pure Goldstone boson lagrangian

$$\mathcal{L}_\chi = \sum_n \mathcal{L}_\chi^{(2n)}, \qquad \mathcal{L}_\chi^{(2n)} = \mathcal{O}((p_\Phi/\Lambda_\chi)^n)\,. \tag{1.19}$$

For $n = 0$ the lagrangian can not contain derivatives and only terms proportional to $U^\dagger U = \text{const.}$ are possible. The most general, chirally invariant Lagrangian at lowest order $\mathcal{O}((p_\Phi/\Lambda_\chi)^2)$ can be written as

$$\mathcal{L}_\chi^{(2)} = \frac{{f_\pi}^2}{4}\langle \partial_\mu U \partial^\mu U^\dagger \rangle\,, \tag{1.20}$$

where $\langle ... \rangle$ denotes the trace in flavor space. External scalar s and pseudoscalar sources p can be included via

$$\chi = 2B_0(s + ip), \qquad \text{with } \chi \mapsto R\chi L^\dagger\,.$$

This also allows to include the explicit symmetry breaking by the non-zero quark masses. The chiral symmetry breaking quark mass term is given by

$$\mathcal{L}_M = -\bar{q}_R M q_L - \bar{q}_L M^\dagger q_R\,. \tag{1.21}$$

With the mass matrix M being constant, $\mathcal{L}_M$ would be invariant, if M transformed like

$$M \mapsto RML^\dagger \,. \tag{1.22}$$

Introducing the mass-term analogous to a scalar source with the correct transformation properties, the full leading order lagrangian is given by

$$\mathcal{L}_\chi^{(2)} = \frac{{f_\pi}^2}{4}\langle \partial_\mu U \partial^\mu U^\dagger \rangle + \frac{{f_\pi}^2 B_0^2}{2}\langle MU^\dagger + UM^\dagger \rangle \,. \tag{1.23}$$

which gives the so called Gell-Mann–Oakes–Renner relation [23]. The free parameter B_0 can be determined by relating the derivative of the ground state energy density with respect to the light-quark mass m_q in pure QCD to the effective field theory

$$\left.\frac{\partial \langle 0|\mathcal{H}_{\mathrm{QCD}}|0\rangle}{\partial m_q}\right|_{m_q=0} = \left.\frac{\partial \langle 0|\mathcal{H}_{\chi}|0\rangle}{\partial m_q}\right|_{m_q=0} , \tag{1.24}$$

which at leading order evaluates to

$$B_0 = -\frac{\langle 0|\bar{q}q|0\rangle}{3{f_\pi}^2} \,. \tag{1.25}$$

1.3.2. Heavy Quark Effective Theory

By observing that a heavy quark bound inside a hadron with momentum p is nearly on-shell and approximately moves with the velocity v of the hadron, on can decompose its momentum p as

$$p^\mu = m_Q v^\mu + k^\mu \,, \tag{1.26}$$

where k^μ is the momentum of the light degrees of freedom. The fluctuations inside a hadron due to the exchange of soft gluons are of order $k^\mu = \Lambda_{\mathrm{QCD}}$, such that the velocity of the heavy quark can be expressed by

$$v_Q^\mu = v^\mu + \mathcal{O}\left(\frac{\Lambda_{\mathrm{QCD}}}{m_Q}\right) \,. \tag{1.27}$$

allowing for a pertubative expansion in $\Lambda_{\mathrm{QCD}}/m_Q$.

Here it is possible to decompose a solution of the Dirac equation into velocity eigenstates

$$\psi(x) = e^{-im_Q v\cdot x}\left[P_+ + P_-\right] Q(x) = e^{-im_Q v\cdot x}\left[Q_v(x) + \tilde{Q}_v(x)\right] \,, \tag{1.28}$$

with the corresponding projectors

$$P_\pm = \frac{1 \pm \not{v}}{2} \quad \text{fulfilling } P_+ + P_- = \mathbb{1},\ P_\pm^2 = \mathbb{1} \text{ and } \not{v} P_\pm = \pm P_\pm \,. \tag{1.29}$$

Thus, the kinetic- and mass-term of the QCD Lagrangian can be expressed as

$$\bar{\psi}(i\not{D} - m_Q)\psi = i\bar{Q}_v v \cdot DQ_v + \bar{\tilde{Q}}_v(-iv\dot{D} - 2m_Q)\tilde{Q}_v + i\bar{Q}_v \not{D}\tilde{Q}_v + i\bar{\tilde{Q}}_v \not{D} Q_v \,. \quad (1.30)$$

If $p^\mu = m_Q v^\mu$ were exactly fulfilled the small component $\tilde{Q}_v$ is equal to zero, as the Dirac equation then implies that $(1 - \not{v})\psi = 0$. For convenience one defines

$$D_\perp^\mu = D^\mu - v^\mu(v\dot{D})\,, \quad (1.31)$$

so (1.30) becomes

$$\mathcal{L} = i\bar{Q}_v v \cdot DQ_v + \bar{\tilde{Q}}_v(-iv \cdot D - 2m_Q)\tilde{Q}_v + i\bar{Q}_v \not{D}_\perp \tilde{Q}_v + i\bar{\tilde{Q}}_v \not{D}_\perp Q_v \,. \quad (1.32)$$

The field $\tilde{Q}$ has a mass of $2m_Q$, while Q is a massless excitation relative to the reference energy $E \approx m_Q$, describing fluctuations in the heavy quark momentum that keep the velocity fixed. As $\tilde{Q}$ is a heavy degree of freedom, one can integrate it out using the equations of motion

$$(iv \cdot D + 2m_Q)\tilde{Q}_v = i\not{D}_\perp Q_v \,, \quad (1.33)$$

resulting in

$$\begin{aligned} \mathcal{L} =& i\bar{Q}_v v \cdot DQ_v + \bar{Q}_v i\not{D}_\perp \frac{1}{2m_Q + iv \cdot D} i\not{D}_\perp Q_v \\ =& i\bar{Q}_v v \cdot DQ_v + \frac{1}{2m_Q}\sum_{n=0}^{\infty} \bar{Q}_v i\not{D}_\perp \left(-\frac{iv \cdot D}{2m_Q}\right)^n i\not{D}_\perp Q_v \,. \end{aligned} \quad (1.34)$$

The leading $1/m_Q$ correction can be expanded as [24]

$$\begin{aligned} \mathcal{L}_{1/m_Q} &= i\bar{Q}_v v \cdot DQ_v + \frac{1}{2m_Q}(-O_1 + O_2 - O_3) \\ O_2 - O_1 &= \bar{Q}_v D_\mu (g^{\mu\nu} - v^\mu v^\nu) D_\nu Q \\ O_3 &= \bar{Q}_v \sigma^{\mu\nu} G_{\mu\nu} Q_v \,, \end{aligned} \quad (1.35)$$

where $O_2 - O_1$ corresponds to the non-relativistic kinetic energy for $v = (1, 0, 0, 0)^T$ and O_3 describes the chromomagnetic coupling between gluons and the heavy quarks. Including the gluon field strength tensor G^a and light-quark fields q one arrives at the full HQET Lagrangian

$$\begin{aligned} \mathcal{L}_{\text{HQET}} =& -\frac{1}{4} G^a_{\mu\nu} G^{a\,\mu\nu} + \bar{q}(i\not{D} - m_q)q + i\bar{Q}_v v \cdot DQ_v \\ &+ \frac{1}{2m_Q}\sum_{n=0}^{\infty} \bar{Q}_v i\not{D}_\perp \left(-\frac{iv \cdot D}{2m_Q}\right)^n i\not{D}_\perp Q_v \,. \end{aligned} \quad (1.36)$$

Considering Eq. (1.34) in the limit $m_Q \to \infty$ only the leading order term remains

$$\mathcal{L}_\infty = i\bar{Q}_v v \cdot D Q_v \,. \tag{1.37}$$

It is apparent that eq. (1.37) contains no Dirac matrices, resulting in a SU(2) spin symmetry group that leaves $\mathcal{L}_\infty$ invariant. In the rest frame the SU(2) generators S^i can be chosen as

$$S^i = \frac{1}{2}\begin{pmatrix} \sigma^i & 0 \\ 0 & \sigma^i \end{pmatrix}, \qquad \left[S^i, S^j\right] = i\epsilon^{ijk} S^k \,, \tag{1.38}$$

with σ denoting the Pauli matrices. An infinitesimal SU(2) transformation

$$Q_v \to (1 + i\vec{\epsilon}\cdot\vec{S})Q_v \tag{1.39}$$

leaves the Lagrangian invariant

$$\delta\mathcal{L}_\infty = \bar{Q}_v \left[iv\cdot D, i\vec{\epsilon}\cdot\vec{S}\right] Q_v = 0 \,, \tag{1.40}$$

meaning that the interactions of the heavy quark leave its spin s_h unchanged. By extension, as the total angular moment J is conserved, the angular momentum of the light degrees of freedom $j_\ell = J - s_\mathrm{h}$ is conserved as well. Consequently particles with the same j_ℓ form multiplets like D, D^* or B, B^* for $j_\ell^P = \frac{1}{2}^-$ as well as for example $h_c, \chi_{c0}, \chi_{c1}$ and χ_{c2} in the doubly heavy systems, that are degenerate at leading order. At next to leading order only O_3 of equation (1.35) transforms non-trivially under spin rotation, which leads to the observed hyperfine splitting of the masses

$$\begin{aligned} m_{D^*} - m_D &\approx 140 \text{ MeV} \\ m_{B^*} - m_B &\approx 45 \text{ MeV} \,. \end{aligned} \tag{1.41}$$

Another symmetry emerges as eq. (1.37) is not depended on the heavy quark mass m_Q, such that it can be extended by

$$\mathcal{L}_\infty = i\sum_{i=1}^{N_f} \bar{Q}_v^i v \cdot D Q_v^i \,, \tag{1.42}$$

where N_f denotes the number of heavy quarks moving with velocity v. Combining the spin symmetry with the invariance under rotations in flavor space, the symmetry group of $\mathcal{L}_\infty$ can be promoted to SU(2 N_f). This is the so-called heavy quark spin-flavor symmetry, that in the limit of $m_Q \to \infty$ the interaction is independent of the heavy quark spin and flavor.

1.4. Hadronic Molecules

A hadronic molecule is a bound state composed of two (or more) hadrons. The concept is analogous to a nucleus that is composed of multiple baryons. As a result, certain characteristics of light nuclei may be generalized to hadronic molecules. For this reason, we begin this section with a very brief overview of few-nucleon systems. For additional material we refer to Refs. [25–27].

Important characteristics for nuclear systems are the binding energy E_b as well as the binding momentum γ. The lightest nucleus composed of a proton and a neutron is the deuteron with a binding energy of $E_b(\text{deuteron}) = 2.22$ MeV, defined as the difference between sum over the masses of the constituents m_i and the mass of the bound state M_X

$$E_b(X) = \sum_i m_i - M_X \,. \tag{1.43}$$

The binding momentum given by

$$\gamma = \sqrt{2\mu E_b}, \quad \mu = \frac{m_1 m_2}{m_1 + m_2} \tag{1.44}$$

is a measure for the typical momentum scale inside a molecule and only well defined for a two body system. Furthermore, it defines the size of a molecule, which large distance behaviour scales like $\exp(-\gamma r)$. The binding momentum ranges from values of a couple MeV for the seperation of the Λ in hypertriton ($\gamma \approx 13$ MeV up to several 100 MeV in He^4 ($\gamma \approx 200$ MeV), which also sets the scale for the binding momenta expected for meson systems. The internucleon interaction is in general strongest in a S-wave, due to the missing centrifugal barrier. Consequently, the deepest bound nuclei are in a S-wave, however, also higher partial waves are possible. The role of the one-pion exchange for nuclear and molecular bindings is still being discussed in the literature and is briefly addressed later in this section.

While there are certain parallels between nuclei and mesonic molecules, there are also differences, e.g. the latter do not survive the large N_c limit [28, 29].

1.4.1. Weinberg Criterion

The Weinberg Criterion developed by Steven Weinberg is a scheme to quantify the molecular and compact components of a bound state wave function [30, 31]. His original goal in 1965 was to demonstrate that the deuteron is not an elementary particle, however, it can also be generalized from bound states to resonances and virtual states close to threshold [32, 33].

One can define the wave function $|\Psi\rangle$ of a bound state as a composition of a compact component $|\psi_0\rangle$ and a two-hadron component $|\mathrm{h_1h_2}\rangle$

$$|\Psi\rangle = \begin{pmatrix} \lambda|\psi_0\rangle \\ \chi(k)|\mathrm{h_1h_2}\rangle \end{pmatrix} . \tag{1.45}$$

In this context compact describes an object whose size is controlled by the confinement radius $R_{\text{conf.}} < 1\text{fm}$, such that this component is much smaller than $\sim 1/\gamma$ for small binding energies. As given by the ansatz, λ quantifies the contribution of the compact component $|\psi_0\rangle$ to the bound state wave function, such that λ^2 denotes the probability to find the compact component in the physical state. $\chi(k)$ is the wave function of the two hadron component with relative momentum k.

As demonstrated by Weinberg in Ref. [34] a general interaction Hamiltonian can be expressed in following form

$$\mathcal{H}|\Psi\rangle = E|\Psi\rangle, \qquad \mathcal{H} = \begin{pmatrix} H_{\mathrm{c}} & V \\ V & H^0_{\mathrm{hh}} \end{pmatrix} , \tag{1.46}$$

using the fact that it is possible with a field redefinition to shift all hadron-hadron interactions into ψ_0, such that the two-hadron Hamiltonian is simply given by the kinetic term $H^0_{\mathrm{hh}} = k^2/(2\mu)$ with μ being the reduced mass of the two-hadron system, see also Ref. [35]. Defining a transition form factor

$$f(k) = \langle\psi_0|V|\mathrm{h_1h_2}\rangle \tag{1.47}$$

the two hadron wave function in momentum space is given by

$$\chi(k) = \lambda \frac{f(k)}{E - k^2/(2\mu)} . \tag{1.48}$$

From the normalization of the bound state wave function one finds:

$$\begin{aligned} 1 =& \langle\Psi|\Psi\rangle = \lambda^2\langle\psi_0|\psi_0\rangle + \int \frac{d^3k}{(2\pi)^3}|\chi(k)|^2\langle\mathrm{h_1h_2}|\mathrm{h_1h_2}\rangle \\ =& \lambda^2 \left(1 + \int \frac{d^3k}{(2\pi)^3}\frac{f^2(k)}{(E_{\mathrm{b}} + k^2/(2\mu))^2}\right) . \end{aligned} \tag{1.49}$$

Recollecting the definition of the wave function renormalization factor in a non-relativistic theory

$$G(E) = \frac{Z}{E - E_p} + \mathcal{O}((E - E_p)^2) \quad \text{with} \quad Z = \frac{1}{1 - \partial_E\Sigma'(E)|_{E=E_p}} \tag{1.50}$$

one finds

$$Z = \left(1 + \int \frac{d^3k}{(2\pi)^3} \frac{f^2(k)}{(E_\mathrm{b} + k^2/(2\mu))}\right)^{-1} \quad \text{from} \quad \Sigma(E) = \int \frac{\mathrm{d}^3k}{(2\pi)^3} \frac{f^2(k)}{E - k^2/(2\mu)} \,. \tag{1.51}$$

Comparing Eq. (1.51) to Eq. (1.51) gives

$$Z = \lambda^2 \,. \tag{1.52}$$

This allows one to write a relation between the probability of finding a compact component, λ^2, and the bare coupling g_0. The Integral of Eq. (1.49) is convergent even if $f(k) = \text{const}$, which in case of a S-wave coupling is satisfied by the LO expansion of $f(k)$ with $f(0) = g_0$ [36]. Solving for g_0 yields

$$g_0^2 = \frac{2\pi\gamma}{\mu^2} \left(\frac{1}{\lambda^2} - 1\right) + \mathcal{O}\left(\frac{\gamma}{\beta}\right) , \tag{1.53}$$

where β denotes the inverse range of forces. Note that higher order corrections are impossible to include in a model-independent way. The bare coupling g_0 appears in the physical propagator of the bound state, such that one can write the corresponding T-matrix for two continuum particles whose threshold lies in close proximity of the bound state pole

$$T_\mathrm{NR}(E) = \frac{g_0^2}{E + E_\mathrm{b} + g_0^2\mu/(2\pi)(ik + \gamma)} \tag{1.54}$$

where the subscript NR indicates non-relativistic normalization. Equation (1.54) corresponds to a one-channel version of the Flatté parameterization.

So one can conclude, that a measurement of near-threshold data in principle allows to determine the composition of the bound state wave function. Following Eq. (1.54), the different behavior of compact and molecular structures is also reflected in the effective range expansion

$$\begin{aligned} a &= -2\frac{1-\lambda^2}{2-\lambda^2} \left(\frac{1}{\gamma}\right) + \mathcal{O}\left(\frac{1}{\beta}\right) \\ r &= -\frac{\lambda^2}{1-\lambda^2} \left(\frac{1}{\gamma}\right) + \mathcal{O}\left(\frac{1}{\beta}\right) , \end{aligned} \tag{1.55}$$

where β denotes the inverse range of forces with $\beta \gg \gamma$. For a pure molecule, one finds that the scattering length a becomes maximal while r tends to be very small, although typically greater than zero. Compact states are characterized by a small scattering length of order $1/\beta$ while $r \to -\infty$

$$\begin{aligned} \lambda^2 = 0: &\qquad a = -\frac{1}{\gamma}, &&\qquad r = \mathcal{O}\left(\frac{1}{\beta}\right) \\ \lambda^2 = 1: &\qquad a = -\mathcal{O}\left(\frac{1}{\beta}\right), &&\qquad r \to -\infty \,. \end{aligned} \tag{1.56}$$

These differences can also have severe impact on the line shapes of such near-threshold states. Solving Eq. (1.55) for Z in the zero-range approximation, namely neglecting terms of $\mathcal{O}(1/\beta)$, results in

$$1 - Z = \sqrt{\frac{a}{a + 2r}} =: X \,. \tag{1.57}$$

As X is the probability of finding the two hadron composite component in the bound state wave function, it is also called *compositeness*.

Production reaction, on the other hand, are sensitive to the residue of the bound state pole, which is given by the effective coupling constant $g_{\text{eff.}}$. It is calculated by multiplying the bare coupling with the wave-function renormalization $\sqrt{Z}$

$$g^2_{\text{eff.}} = Z g_0^2 = 16\pi M^2 \left(\frac{1}{\gamma}\right)(1 - \lambda^2) + \mathcal{O}\left(\frac{E_{\text{b}}}{M}\right) \,. \tag{1.58}$$

Thus the effective coupling of such a system is bounded from above, becoming maximal for a pure molecular state. The consequences of this important observation are discussed later in this section.

In contrast the wave functions of resonances and virtual states are not normalizable and Eq. (1.49) can not be employed, which makes the extension to states other than bound states difficult. However, the formal definition of the field renormalization factor Z allows to derive similar relations between Z, a, r and $g^2_{\text{eff.}}$ for virtual states, e.g. for Eq. (1.55) one simply needs to replace γ with $-\gamma$ to get relations for a virtual state. Further using the fact that a probabilistic interpretation requires $|X| \in (0, 1)$, Ref. [33] introduced

$$\bar{X}_A = 1 - \bar{Z}_A = \sqrt{\frac{1}{1 + |2r/a|}} \,. \tag{1.59}$$

Note that this choice is not unique and alternative suggestions exist, eg. Ref. [37]. By construction Eq. (1.59) agrees with Weinberg's original formula (Eq. (1.57)) in its regime of applicability. Ref. [33] used the fact that by varying QCD parameters like quark masses, a bound state pole can transition into either a virtual state or a resonance and therefore allow for a connection between them.

Both Weinberg's original formula and its extensions are generally based on the fact that the scattering amplitude near threshold fulfills the effective range expansion, which is typically expected in systems where the momenta are smaller than the inverse range of forces. While true in most cases, Ref. [38] demonstrated that scattering amplitudes may have zeros close to threshold, which invalidate the effective range expansion.

1.4.2. Lineshapes

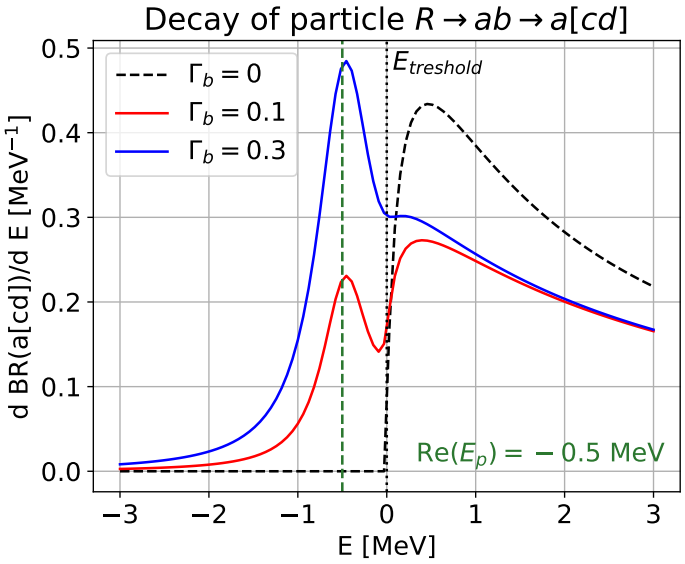

Figure 1.2.: Resulting count rate for a bound state decaying into its constituents $R \to a, b$, with one of the constituents further decaying into $b \to cd$, for different width of the constituents Γ_b.

For more deeply bound states like the $Y(4230)$ with $E_b \approx 60$ MeV uncertainties are of the same order as the compositeness itself. However, as derived in Eq. (1.58), the coupling of a hadronic molecule to the two hadron continuum becomes maximal. Consequently, the constituents threshold can significantly distort the lineshape of a molecular resonance [36, 39]. In case of the $Y(4230)$, one of its constituents, the $D_1(2420)$, is unstable itself and can decay into $D^*\pi$. To demonstrate the effects of this one can choose a generalization of Eq. (1.54). The resulting count rate in the elastic channel may be written as

$$\frac{\partial T}{\partial E} \propto \frac{1 + \frac{ig^2}{2}(\partial k_{\mathrm{eff}}/\partial E)}{(E + E_b + \frac{g^2}{2}(ik_{\mathrm{eff}} + \gamma) + i\Gamma_0/2)^2}\,, \tag{1.60}$$

where

$$k_{\mathrm{eff}}(E) = \sqrt{\mu}\sqrt{\sqrt{E^2 + \Gamma_b^2/4} + E} + i\sqrt{\mu}\sqrt{\sqrt{E^2 + \Gamma_b^2/4} - E}$$

is introduced to account for the constituents width Γ_b [39].
The emerging lineshapes for the example of the $X(3872)$ as a $D^*\bar{D}$ molecule are shown in Fig. 1.2, using

$$m_1 = 1865 \text{ MeV}, \quad m_2 = 2007 \text{ MeV}, \quad \Gamma_0 = 1.5 \text{ MeV}, \quad g_{ab} = 0.1 \text{ MeV}\,. \tag{1.61}$$

Starting with a true bound state, i.e. $\Gamma_b = 0$ MeV, denoted by the black dotted curve in figure 1.2, the lineshape is only non-zero above the threshold with a peak structure at slightly higher energies. However, if the constituent has a non-vanishing width, coupling strength can leak below the threshold and enhance the pole structure itself, where the relevant parameter is given by the binding energy over the width of the constituent E_b/Γ_b.

1.4.3. Powercounting

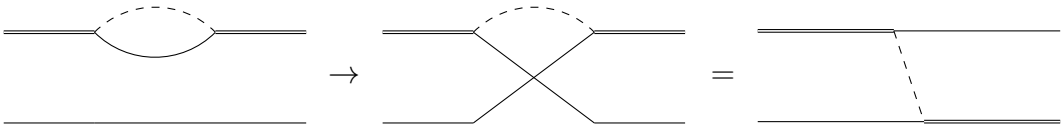

Figure 1.3.: The 1st diagram shows the contribution to the 2-body self energy for an unstable particle involved. Interchanging momenta of the final particles as shown in the second diagram reveals, that the One-pion exchange in the 3rd diagram is of the same order as the first one.

In order to estimate the uncertainties of an effective field theory a proper power counting scheme is necessary. However, no theoretical agreement is found for doubly heavy systems, with XEFT and Weinberg counting being the most prominent proposals in the present situation. XEFT, based conceptually on the KSW scheme introduced for NN scattering [40], was first introduced to investigate the pion dynamics for the $X(3872)$, under the assumption that it is a $D^*\bar{D}$ molecule [41].

The starting assumption in XEFT is that the typical pion momentum is small, so all momentum scales above $p_\pi \approx p_D \approx \mu$ are integrated out. As energies are treated non-relativistically, they are of order momentum squared. Consequently, the one pion exchange as well as the momentum-independent contact interactions are naively of order $\mathcal{O}(1)$. In that sense, the theory is perturbative and therefore cannot produce bound states. Since bound states are formed, the corresponding scattering length is large. Therefore, the momentum-independent contact terms must scale like $\mathcal{O}(p^{-1})$ and are treated non-perturbatively.

The classical Weinberg power counting [42] on the other hand requires to calculate a potential up to order $\mathcal{O}((p_\Phi/\Lambda_\chi)^n)$. The resulting potential is then used in a scattering equation, thus also including the one-pion exchange non-perturbatively. For 3-body systems, this yields some significant deviation between the two power countings [43].

We study systems where πD loops provide inelasticises for resonances. Those need to be resummed. To see that this naturally calls for a resummation also of the

one-pion exchange let us look at DD^* scattering - the system that generates the $T_{cc}(3875)$. The Lagrangian for $D^*D\pi$ introduced later in Section 1.5 gives rise to both a momentum-dependent self-energy of the D^* and a one-pion exchange in the D^*D system, shown as the first and last diagram of Fig. 1.3. As both diagrams can be converted into each other by simply changing the momenta of the final state particles, both are naturally of the same order. Therefore, it is essential for the 3-body dynamics to include both the momentum-dependent self-energy as well as the one-pion exchange simultaneously to not violate 3-body unitarity [44]. In their analysis of the T_{cc}, Ref. [45] investigated the effects of a perturbative and non-perturbative inclusion of the one-pion exchange. Considering no 3-body effects or only the momentum-dependent D^* self energy non-perturbatively, following XEFT, leads to significantly different pole parameters. Ref. [45] demonstrates that both dynamical ingredients, the D^* self-energy as well as the one-pion exchange, need to be considered non-perturbatively to achieve 3-body unitarity and allow for a meaningful pole extraction.

1.5. Heavy Meson Chiral Perturbation Theory

From the derivation of heavy quark effective theory we find that for hadrons that contain one or more heavy quark the chromomagnetic interaction is strongly suppressed, leading to the conservation of the heavy quark spins. When studying hadronic molecules, however, it is not appropriate to work on quark level, but hadrons need to be considered as degrees of freedom, following the ansatz from chiral perturbation theory. This further allows for a proper inclusion of the Goldstone bosons. To construct a Lagrangian that is invariant under both heavy-quark spin and chiral transformation it is useful to define superfields representing the different light-quark spin multiples of heavy mesons, that have the correct transformation properties [46]. The ground states of heavy mesons with light quark quantum numbers $j_\ell^P = \frac{1}{2}^-$, namely $\{D, D^*\}$, will be denoted by H_a. For angular momentum $L = 1$ two spin multiplets emerge, one with $j_\ell^P = \frac{3}{2}^+$ containing the spin pair $\{D_1, D_2\}$ and one with $j_\ell^P = \frac{1}{2}^+$ containing $\{D_0', D_1'\}$ denoted by T_a and S_a, respectively. We may thus write

$$\begin{aligned} H_a^{(Q)} &= \frac{1+\not{v}}{2}\left[D_a^{*\mu}\gamma_\mu - D_a\gamma_5\right] \ , \\ T_a^{(Q)\mu} &= \frac{1+\not{v}}{2}\left[D_{2a}^{\mu\nu}\gamma_\nu - \sqrt{\tfrac{3}{2}}D_{1a\nu}\gamma_5(g^{\mu\nu} - \tfrac{1}{3}\gamma^\nu(\gamma^\mu - v^\mu))\right] \\ S_a^{(Q)} &= \frac{1+\not{v}}{2}\left[D_1^{\prime\mu}\gamma_\mu\gamma_5 - D_{0a}'\right] \ , \end{aligned} \tag{1.62}$$

where a is the SU(3) flavor index. We have, e.g., for $j_\ell^P = \frac{1}{2}^-$

$$\begin{aligned} D_a &= (D^0, D^+, D_s^+) \\ D^*_{a\mu} &= (D^{*0}_\mu, D^{*+}_\mu, D^{*+}_{s\mu})\,. \end{aligned} \tag{1.63}$$

The heavy field operators contain a factor $\sqrt{M_{\rm H}}$ and therefore have dimension 3/2. Under $\mathrm{SU}(3)_L \otimes \mathrm{SU}(3)_R$ chiral symmetry the superfield transform like

$$H_a \to H_b U^\dagger_{ba}\,, \tag{1.64}$$

where U is a unitary matrix introduced in Section 1.3.1. Under heavy-quark spin symmetry it transforms like

$$H_a \to S H_a\,, \tag{1.65}$$

where $S \in \mathrm{SU}(2)$ as demonstrated in Eq. 1.38 and below. At last, under Lorentz transformations

$$H_a \to D(\Lambda) H_a D(\Lambda)^{-1}\,, \tag{1.66}$$

where $D(\Lambda) \in \mathrm{O}(1,3)$ is a representation of the Lorentz group. As pair creation is suppressed in HQET the field operators, eg. $D^{*\mu}_a$ and D_a for the ground state, only destroy the corresponding $D^{*\mu}_a, D_a$ mesons with 4-velocity v. The superfields creating heavy mesons are given by

$$\begin{aligned} \bar{H}^{(Q)}_a = \gamma_0 H^{(Q)\,\dagger}_a \gamma_0 &= \left[D^{*\mu\,\dagger}_a \gamma_\mu + D^\dagger_a \gamma_5\right] \frac{1+\not{v}}{2} \\ \bar{T}^{(Q)\mu}_a = \gamma_0 T^{(Q)\mu\,\dagger}_a \gamma_0 &= \left[D^{\mu\nu\,\dagger}_{2a} \gamma_\nu + \sqrt{\tfrac{3}{2}} D^\dagger_{1a\nu} (g^{\mu\nu} - \tfrac{1}{3}(\gamma^\mu - v^\mu)\gamma^\nu)\gamma_5\right] \frac{1+\not{v}}{2}\,. \\ \bar{S}^{(Q)}_a = \gamma_0 S^{(Q)\,\dagger}_a \gamma_0 &= \left[D'^{\mu\,\dagger}_{1a} \gamma_\mu \gamma_5 - D'^\dagger_{0a}\right] \frac{1+\not{v}}{2}\,. \end{aligned} \tag{1.67}$$

The corresponding superfields containing an anti-heavy quark $\bar{Q}$ can be constructed using the charge conjugation operator $\mathcal{C} = i\gamma^2\gamma^0$, where we are following the convention $\mathcal{C} D^{(Q)}_a \mathcal{C}^{-1} = D^{(\bar{Q})}_a$ and $\mathcal{C} D^{*(Q)}_a \mathcal{C}^{-1} = -D^{*(\bar{Q})}_a$

$$
\begin{aligned}
H_a^{(\bar{Q})} &= \left[D_{a\mu}^{*(\bar{Q})}\gamma^\mu - D_a^{(\bar{Q})}\gamma_5\right]\frac{1-\not{v}}{2} \\
\bar{H}_a^{(\bar{Q})} &= \gamma_0 H_a^{(\bar{Q})\dagger}\gamma_0 = \frac{1-\not{v}}{2}\left[D_a^{*(\bar{Q})\,\mu\,\dagger}\gamma_\mu + D_a^{(\bar{Q})\,\dagger}\gamma_5\right] \\
T_a^{(\bar{Q})\mu} &= \left[D_{2a}^{(\bar{Q})\mu\nu}\gamma_\nu - \sqrt{\tfrac{3}{2}}D_{1a\nu}^{(\bar{Q})}\gamma_5(g^{\mu\nu} - \tfrac{1}{3}(\gamma^\mu - v^\mu)\gamma^\nu)\right]\frac{1-\not{v}}{2} \\
\bar{T}_a^{(\bar{Q})\,\mu} &= \gamma_0 T_a^{(\bar{Q})\,\mu\,\dagger}\gamma_0 = \frac{1-\not{v}}{2}\left[D_{2a}^{(\bar{Q})\,\mu\nu\,\dagger}\gamma_\nu + \sqrt{\tfrac{3}{2}}D_{1a\nu}^{(\bar{Q})\ \dagger}(g^{\mu\nu} - \tfrac{1}{3}\gamma^\nu(\gamma^\mu - v^\mu)\gamma_5)\right] \\
S_a^{(\bar{Q})} &= \left[D_{1a}^{\prime\mu\dagger}\gamma_\mu\gamma_5 - D_{0a}^{\prime}\right]\frac{1-\not{v}}{2} \\
\bar{S}_a^{(\bar{Q})} &= \gamma_0 S_a^{(\bar{Q})\,\dagger}\gamma_0 = \frac{1-\not{v}}{2}\left[D_{1a}^{\prime\mu\dagger}\gamma_\mu\gamma_5 - D_{0a}^{\prime}\right]\,,
\end{aligned}
\tag{1.68}
$$

where $\langle ... \rangle$ denotes the tracing over the Dirac matrices, $\Lambda_\chi \approx 4\pi f_\pi$ the chiral symmetry braking scale and $D_\mu = \partial_\mu + \mathcal{V}_\mu$, $D'_\mu = \partial_\mu - \mathcal{V}_\mu$ the covariant derivatives.

Pseudoscalar mesons couple through the vector $\mathcal{V}_\mu$ and axialvector $\mathcal{A}_\mu$ current containing an even and odd number of boson fields, respectively,

$$
\begin{aligned}
\mathcal{V}_\mu &= \frac{1}{2}(u^\dagger\partial_\mu u + u\partial_\mu u^\dagger) \\
\mathcal{A}_\mu &= \frac{i}{2}(u^\dagger\partial_\mu u - u\partial_\mu u^\dagger)\,,
\end{aligned}
\tag{1.69}
$$

conserving chiral symmetry [47]. Chiral symmetry violation is introduced via constructions of the kind

$$
\chi_\pm = u^\dagger\chi u^\dagger \pm u\chi^\dagger u\ , \tag{1.70}
$$

with $\chi = 2BM$, where M is the quark mass matrix and B a scale parameter related to the chiral condensate. Here the exponential parameterization is employed for the light Goldstone boson fields, where $u = \sqrt{U}$ consistent with Eq. (1.18):

$$
\begin{aligned}
u &= \exp\left(i\frac{\Phi}{\sqrt{2}f_\pi}\right) \\
\Phi &= \begin{pmatrix} \frac{\pi^0}{\sqrt{2}} + \frac{\eta_8}{\sqrt{6}} & \pi^+ & K^+ \\ \pi^- & -\frac{\pi^0}{\sqrt{2}} + \frac{\eta_8}{\sqrt{6}} & K^0 \\ K^- & \bar{K}^0 & -\frac{2\eta_8}{\sqrt{6}} \end{pmatrix},
\end{aligned}
\tag{1.71}
$$

with $f_\pi = 92$ MeV denoting the pion decay constant in the chiral limit. The Lagrangian is constructed by imposing invariance under heavy-quark spin and chiral transformation [19, 48–50].

The mass and kinetic terms are

$$\begin{aligned}\mathcal{L}_{\text{kin}} =& i\langle \bar{H}_b v_\mu D^\mu_{ba} H_a\rangle + \frac{{f_\pi}^2}{4}\left(\langle \partial^\mu u \partial_\mu u^\dagger\rangle + \langle \chi_+\rangle\right) \\ &+\langle \bar{S}^\mu_b (iv_\nu D^\nu_{ba} - \delta_{ba}\Delta_S) S_{a\mu}\rangle + \langle \bar{T}^\mu_b (iv_\nu D^\nu_{ba} - \delta_{ba}\Delta_T) T_{a\mu}\rangle\,,\end{aligned} \tag{1.72}$$

where Δ_S and Δ_T denote the mass difference due to hyperfine splitting in the $\{D_0', D_1'\}$ and $\{D_1, D_2\}$ doublet, respectively. The relevant terms for the interaction are given by

$$\begin{aligned}\mathcal{L}_{\text{int}} =& g\langle H^{(Q)}_b \not{\mathcal{A}}_{ba}\gamma_5 \bar{H}^{(Q)}_a\rangle + g_{3/2}\langle T^{(Q)\mu}_b \not{\mathcal{A}}_{ba}\gamma_5 \bar{T}^{(Q)}_{a\,\mu}\rangle \\ &+ \frac{h_1}{\Lambda_\chi}\langle T^{(Q)\mu}_b (D_\mu \not{\mathcal{A}})_{ba}\gamma_5 \bar{H}^{(Q)}_a\rangle + \frac{h_2}{\Lambda_\chi}\langle T^{(Q)\mu}_b (\not{D}\mathcal{A}_\mu)_{ba}\gamma_5 \bar{H}^{(Q)}_a\rangle \\ &+ g\langle \bar{H}^{(\bar{Q})}_a \not{\mathcal{A}}_{ab}\gamma_5 H^{(\bar{Q})}_b\rangle + g_{3/2}\langle \bar{T}^{(\bar{Q})\mu}_a \not{\mathcal{A}}_{ab}\gamma_5 T^{(\bar{Q})}_{b\,\mu}\rangle \\ &+ \frac{h_1}{\Lambda_\chi}\langle \bar{T}^{(\bar{Q})\mu}_a (\not{\mathcal{A}}\overleftarrow{D}_\mu)_{ab}\gamma_5 H^{(\bar{Q})}_b\rangle + \frac{h_2}{\Lambda_\chi}\langle \bar{T}^{(\bar{Q})\mu}_a (\mathcal{A}_\mu \overleftarrow{\not{D}})_{ab}\gamma_5 H^{(\bar{Q})}_b\rangle + \text{h.c.}\,.\end{aligned} \tag{1.73}$$

1.5.1. Coupling constants

The relation between the decay width and the effective coupling of a resonance R with total angular momentum J_R decaying into the two-body final state a in the narrow width approximation is given by [51]

$$\Gamma_{R\to a} = \frac{1}{m_R}\rho_a(m_R^2)\left(\frac{1}{2J_R+1}\right)\sum_{\text{pol.}}|\mathcal{M}_{R\to a}|^2\,, \tag{1.74}$$

where m_R denotes the resonance mass, the phase space factor is

$$\rho_a(m_R^2) = \frac{2p_a(m_R)}{16\pi m_R} \tag{1.75}$$

and p_a denotes the relative momentum of the decay particles in the rest frame of the resonance,

$$p_a(m_R) = \frac{\sqrt{(m_R^2-(m_{a,1}+m_{a,2})^2)(m_R^2-(m_{a,1}-m_{a,2})^2)}}{(2m_R)}\,, \tag{1.76}$$

with $m_{a,i}$ for the masses of the particles in channel a. The summation runs over the polarizations of the final and initial state, respectively, if necessary. The pertinent matrix elements can be read off the Lagrangian given in Eq. (1.73) straightforwardly allowing one to determine the couplings from the experimentally measured decay widths.

1.5.2. Superfield $H \to H\Phi$ transition

The Lagrangian for the transition of a $j_\ell^P = \frac{1}{2}^-$ superfield into $\frac{1}{2}^-$ and a Goldstone boson is given by

$$\mathcal{L}_{HH\pi} = g\langle H_b \not{\mathcal{A}}_{ba}\gamma_5 \bar{H}_a\rangle \,. \tag{1.77}$$

Expanding the relevant terms for $D^* \to D\Phi$ results in

$$\begin{aligned}\mathcal{L}_{D^*\to D\Phi} =& \frac{g}{4\sqrt{2}f_\pi}\left[{D^*}_\alpha D^\dagger \partial_\mu \Phi\right]\langle(1+\not{v}_{D^*})\gamma^\alpha\gamma^\mu(1+\not{v}_D)\rangle \\ =& \frac{g}{4\sqrt{2}f_\pi}\left[{D^*}_\alpha D^\dagger \partial_\mu \Phi\right](4\,(v_{D^*}\cdot v_D + 1)\, g^{\alpha\mu}) \\ \overset{\text{L.O.}}{=}& \frac{\sqrt{2}g}{f_\pi}\left[{D^*}_\alpha D^\dagger \partial^\alpha \Phi\right] \,.\end{aligned} \tag{1.78}$$

At leading order in HQET the velocity of the heavy mesons do not change due to the mass degeneracy in the multiplets. As the pion 4-momentum is contracted with the D^* polarization vector, only the spacial components remain

$$V({D^*}_b \to D_a \Phi_{ba}) = \frac{\sqrt{2}g}{f_\pi}\tau_{ba}(p_\pi \cdot \epsilon_{D^*})\sqrt{m_{D^*}m_D} = g_1^\pi \tau_{ba}(p_\pi \cdot \epsilon_{D^*}) \,, \tag{1.79}$$

where τ_{ba} is the corresponding isospin coefficient.
The squared matrix-element for the transition of $D^{*a} \to D^b \phi_{ab}$, summed over the D^* polarization, is given by

$$\sum_{\text{pol.}} |\mathcal{M}_{D^*D\pi}|^2 = \frac{2g^2 c_{ab}^2 p_{\pi D}(m_{D^*})^2}{{f_\pi}^2} m_{D^*} m_D \,, \tag{1.80}$$

where the coefficient c_{ab} can be read off from the Goldstone boson matrix provided in Eq. (1.18): $c_{+0} = 1$ and $c_{++} = 1/\sqrt{2}$. Using eq. (1.74) we extract for $D^{*+} \to D^0\pi^+$

$$|g(D^{*+} \to D^0\pi^+)| = \sqrt{\frac{12{f_\pi}^2\pi\Gamma(D^{*+} \to D^0\pi^+)}{p_{\pi D}(m_{D^*})^3}\frac{m_{D^{*+}}}{m_{D^0}}} \approx 0.57 \,, \tag{1.81}$$

where the central values listed in the Review of Particle Physics by the Particle Data Group [51] were used

$$\Gamma(D^{*+} \to D^0\pi^+) = \text{BR}(D^{*+} \to D^0\pi^+)\cdot\Gamma_{\text{full}}^{D^{*+}} = 0.677 \cdot 83.4\,\text{keV} = 56.4\,\text{keV} \,. \tag{1.82}$$

Analogously from $D^{*+} \to D^+\pi^0$ we find

$$|g(D^{*+} \to D^+\pi^0)| = \sqrt{\frac{24{f_\pi}^2\pi\Gamma(D^{*+} \to D^+\pi^0)}{p_{\pi D}(m_{D^*})^3}\frac{m_{D^{*+}}}{m_{D^+}}} \approx 0.57 \,, \tag{1.83}$$

with $\Gamma(D^{*+} \to D^+\pi^0) = 25.6\,\text{keV}$. Therefore we use $g = 0.57$ in our calculations in line with the non-relativistic limit in Ref. [52] and lattice calculations [53]. The Lagrangian for $D^*D^*\pi$ is given by

$$\begin{aligned}\mathcal{L}_{D^*\to D^*\pi} =& \frac{g}{4\sqrt{2}f_\pi} D^*{}_\alpha D^{*\dagger}_\beta \Phi p_\mu \langle (1+\not{v}^{(1)})\gamma^\alpha\gamma^\mu\gamma_5\gamma^\beta(1+\not{v}^{(2)})\rangle \\ =& \frac{g}{4\sqrt{2}f_\pi} D^*{}_\alpha D^{*\dagger}_\beta \Phi p_\mu \left[4i\left(v^{(1)}_\nu \epsilon^{\alpha\beta\mu\nu} + v^{(2)}_\nu \epsilon^{\alpha\beta\mu\nu}\right)\right] \\ \overset{\text{L.O.}}{=}& \frac{\sqrt{2}ig}{f_\pi} D^{*i} D^{*\dagger j} \Phi p_k \epsilon^{ijk}\,,\end{aligned} \tag{1.84}$$

resulting in the vertex

$$V(D^*{}_b \to D^*{}_a \Phi_{ba}) = i\frac{\sqrt{2}g}{f_\pi}\epsilon^i_{D^*}\epsilon^{*j}_{D^*} p^k_\pi \tau_{ba}\epsilon^{ijk} m_{D^*} = i g_2^\pi \epsilon^i_{D^*}\epsilon^{*j}_{D^*} p^k \tau_{ba}\epsilon^{ijk}\,, \tag{1.85}$$

where $g_2^\pi = \frac{\sqrt{2}g}{f_\pi} m_{D^*}$.

1.5.3. Superfield $T \to H\Phi$ transition

The interaction of the $j_\ell^P = \frac{3}{2}^+$ dublet $\{D_2, D_1\}$ with $\{D^*, D\}$ and the Goldstone bosons Φ given in Eq. (1.73) can be re-expressed as

$$\begin{aligned}\mathcal{L}_{TH\pi} &= i\frac{h_1}{\Lambda_\chi}\langle T_b^{(Q)\mu}(D_\mu \not{\mathcal{A}})_{ba}\gamma_5 \bar{H}_a^{(Q)}\rangle + i\frac{h_2}{\Lambda_\chi}\langle T_b^{(Q)\mu}(\not{D}\mathcal{A}_\mu)_{ba}\gamma_5\bar{H}_a^{(Q)}\rangle + \text{h.c.} \\ &= -\frac{h'}{f_\pi}\langle T^{(Q)\mu}\gamma^\nu(\partial_\mu\partial_\nu\Phi)\gamma_5\bar{H}^{(Q)}\rangle + \text{h.c.}\,,\end{aligned} \tag{1.86}$$

where $h' = (h_1 + h_2)/\Lambda_\chi$.
The resulting Vertex for $D_1 \to D^*\pi$ is

$$\begin{aligned}\mathcal{L}_{D_1D^*\pi} =& \frac{h'}{4f_\pi}\sqrt{\frac{3}{2}}(D_1)_\alpha (D^*)_\beta \Phi p_\mu p_\nu \\ & \langle (1+\not{v}_{D_1})\gamma_5 (g^{\mu\alpha} - \frac{1}{3}\gamma^\alpha(\gamma^\mu - v^\mu_{D_1}))\gamma^\nu\gamma_5\gamma^\beta(1+\not{v}_{D^*})\rangle \\ \overset{\text{L.O.}}{=}& \sqrt{\frac{2}{3}}\frac{h'}{f_\pi}(D_1)_\alpha(D^*)_\beta\Phi \\ & (3p^\alpha p^\beta - (p^2 - (p\cdot v)^2)g^{\alpha\beta} - (p\cdot v)(p^\alpha v^\beta + p^\beta v^\alpha))\,.\end{aligned} \tag{1.87}$$

Due to the Proca-constraint the last term vanishes, as a heavy-field is contracted with the velocity v. The 0th component drops out, such that the D-wave scales with the 3-momentum squared.

$$\mathcal{L}_{D_1D^*\pi} = \sqrt{\frac{2}{3}}\frac{h'}{f_\pi}(D_1)_i(D^*)_j\Phi(3p^ip^j - p^2\delta^{ij})\,, \tag{1.88}$$

The decay of the narrow D_1 into $D^*\pi$ is predominately in a D-wave, since the S-wave is suppressed by heavy-quark spin symmetry, which calls for the conservation of the light quark total angular momentum in the decay. However, violations of this symmetry in the charm sector can be sizeable. To get an estimate for the S-wave strength in the D_1 decay, we can use the fact that the spin partner of the D_1, the D_2, can only decay into $D^*\pi$ and $D\pi$ in a pure D-wave due to the total angular momentum conservation [54]. From Eq. (1.86) it follows

$$\begin{aligned}\mathcal{L}_{D_2D^*\pi} =& \frac{h'}{4f_\pi}(D_2)_{\mu\alpha}(D^*)_\beta \Phi p^\mu p_\nu \langle (1+\not{v}_{D_2})\gamma^\alpha\gamma^\nu\gamma_5\gamma^\beta(1+\not{v}_{D^*})\rangle \\ \overset{\text{L.O.}}{=}& \frac{2ih'}{f_\pi}(D_2)_{\mu\alpha}(D^*)_\beta \Phi p^\mu p_\nu v_\gamma \epsilon^{\alpha\beta\nu\gamma}\,,\end{aligned} \tag{1.89}$$

resulting in

$$\mathcal{L}_{D_2D^*\pi} = \frac{2ih'}{f_\pi}(D_2)_{ik}(D^*)_j \Phi p_i p_l \epsilon^{kjl}\,. \tag{1.90}$$

Analogously the Lagrangian for $D_2 \to D\pi$ is given by

$$\begin{aligned}\mathcal{L}_{D_2D\pi} =& -\frac{h'}{4f_\pi}(D_2)_{\mu\alpha} D^\dagger(\partial^\mu\partial^\nu\Phi)\langle (1+\not{v}_{D_2})\gamma^\alpha\gamma_\nu(1+\not{v}_D)\rangle \\ \overset{\text{L.O.}}{=}& \frac{h'}{f_\pi}(D_2)_{\mu\alpha} D\Phi p^\mu p^\nu (v^2+1) g^{\alpha\nu}\,.\end{aligned} \tag{1.91}$$

The 0th component of field contraction goes to 0, yielding

$$\mathcal{L}_{D_2D\pi} = \frac{2h'}{f_\pi}(D_2)_{ij} p^i p^j D^\dagger \Phi\,. \tag{1.92}$$

Adding the partial widths, according to Eq. (1.74), the total width of the D_2 is given by

$$\begin{aligned}\Gamma_{D_2} =& \frac{1}{5}\frac{\rho_{\pi D^*}(m_{D_2}^2)}{m_{D_2}} \sum_{\text{pol.}} |\mathcal{M}_{D_2\to D^*\pi}|^2 \\ &+ \frac{1}{5}\frac{\rho_{\pi D}(m_{D_2}^2)}{m_{D_2}} \sum_{\text{pol.}} |\mathcal{M}_{D_2\to D\pi}|^2,\end{aligned} \tag{1.93}$$

with

$$\begin{aligned}\sum_{\text{pol.}} |\mathcal{M}_{D_2\to D^*\pi}|^2 &= \frac{3}{2}\frac{2h'^2}{{f_\pi}^2} p_{\pi D^*}(m_{D_2})^4 m_{D_2} m_{D^*} \\ \sum_{\text{pol.}} |\mathcal{M}_{D_2\to D\pi}|^2 &= \frac{3}{2}\frac{4h'^2}{3{f_\pi}^2} p_{\pi D}(m_{D_2})^4 m_{D_2} m_D\,,\end{aligned} \tag{1.94}$$

where the factor 3/2 in front of each term results from adding the partial widths of the $D^{(*)+}\pi^0$ and $D^{(*)0}\pi^+$ in line with what was done for the decay of the D^*. Using $\Gamma_{D_2} = 47.3$ MeV [51], one can extract $h' = 0.82$ GeV^{-1}. Our calculation is not sensitive to the sign of this coupling which we chose positive.
Allowing for a $D^*\pi$ S-wave, the expression for the total width of the D_1 reads

$$\begin{aligned}\Gamma_{D_1} = &\frac{1}{3}\frac{\rho_{\pi D^*}(m_{D_1}^2)}{m_{D_1}}\sum_{\text{pol.}}|\mathcal{M}^{s-\text{wave}}_{D_1\to D^*\pi}|^2 \\ &+\frac{1}{3}\frac{\rho_{\pi D^*}(m_{D_1}^2)}{m_{D_1}}\sum_{\text{pol.}}|\mathcal{M}^{d-\text{wave}}_{D_1\to D^*\pi}|^2,\end{aligned} \tag{1.95}$$

From Eq. (1.88) one finds

$$\sum_{\text{pol.}}|\mathcal{M}^{d-\text{wave}}_{D_1\to D^*\pi}|^2 = \frac{h'^2}{{f_\pi}^2}p_{D^*\pi}(m_{D_1})^4 m_{D_1} m_{D^*}\ , \tag{1.96}$$

where again a factor 3/2 was included to account for the two possible final states. With h' fixed above, one finds $\Gamma^{d\text{-wave}}_{D_1} = 15$ MeV, in agreement with Ref. [54]. Since the total width of the $D_1(2420)$ is 31 MeV [51], the S-wave decay must generate the remainder. Using

$$\mathcal{L}^{\text{s-wave}}_{D_1D^*\pi} = i\frac{h'_s}{\sqrt{6}f_\pi}\left(D_{1b}\cdot D^{*\dagger}_a\right)\partial_0\phi_{ba} \tag{1.97}$$

one gets

$$\sum_{\text{pol.}}|\mathcal{M}^{s-\text{wave}}_{D_1\to D^*\pi}|^2 = \frac{h'^2_s\omega_\pi^2}{6{f_\pi}^2}\frac{3}{2}m_{D_1}m_{D^*}\ , \tag{1.98}$$

where ω_π denotes the energy of the pion and again the factor 3/2 accounts for the two decay channels $D_1^+ \to D^{*0}\pi^+$ and $D^{*+}\pi^0$. This leads to $h'_s = 0.57$. Below we study a pion angular distribution, which is sensitive to the relative sign of h' and h'_s. We already account for the observation that the data call for equal signs of the two.

1.5.4. Superfield $T \to T\Phi$ transition

The vertex functions presented in this section are only relevant for the full analysis discussed in Sec. 3.

The transition of the $j_\ell^P = \frac{3}{2}^+$ doublet $\{D_2, D_1\}$ into $\{D_2, D_1\}$ and a Goldstone bosons Φ is given in Eq. (1.73) by

$$\mathcal{L}_{TT\Phi} = g_{3/2}\langle T_b^{(Q)\mu}\not{\mathcal{A}}_{ba}\gamma_5\bar{T}^{(Q)}_{a\,\mu}\rangle\,. \tag{1.99}$$

The resulting vertex for $D_2 \to D_1\pi$ reads

$$\begin{aligned}\mathcal{L}_{D_2D_1\Phi} =& -\frac{\sqrt{3}g_{3/2}}{f_\pi} D_2^{\mu\nu} D_1^{\beta\,\dagger} p^\alpha \left\langle (1+\not{v}_{D_2})\gamma_\nu\gamma_\alpha\gamma_5(g_{\mu\beta}-\frac{1}{3}(\gamma_\mu - v_{D_1\,\mu})\gamma_\beta)\gamma_5(1+\not{v}_{D_1})\right\rangle \\ \overset{\text{L.O.}}{=}& -i\frac{8g_{3/2}}{\sqrt{3}f_\pi} D_2^{\mu\nu} D_1^{\beta\,\dagger} p^\alpha \left(2g^{\alpha\nu}g^{\beta\mu} - g^{\alpha\mu}g^{\beta\nu} + g^{\alpha\beta}g^{\mu\nu}\right. \\ & \left. + g^{\alpha\beta}v^\mu v^\nu - g^{\alpha\nu}v^\beta v^\mu + g^{\beta\nu}v^\alpha v^\mu\right) .\end{aligned} \tag{1.100}$$

Due to the Proca constraint, the terms in the second line proportional to $v^\mu v^\nu$ vanish, such that the vertex is given by

$$\begin{aligned}\mathcal{L}_{D_2D_1\Phi} &= -i\frac{8g_{3/2}}{\sqrt{3}f_\pi}\left(2D_2^{\mu\nu}D_{1\,\mu}^\dagger p_\nu - D_2^{\mu\nu}D_{1\,\nu}^\dagger p_\mu + D_{2\,\mu}^{\mu}D_{1\,\nu}^\dagger p^\nu\right) \\ &= -i\frac{8g_{3/2}}{\sqrt{3}f_\pi} D_2^{ij} D_{1\,i}^\dagger p_j \,.\end{aligned} \tag{1.101}$$

Here we exploited that the polarization vector for a Spin-2 particle corresponds to a symmetric rank-2 tensor, i.e. it is symmetric under the exchange of its indices and its trace vanishes in $d = 4$ dimensions.

Analogous to $D^* \to D^*\Phi$ in Eq. (1.84), the $j_\ell^P = \frac{3}{2}^+$ doublet can also emit a pion in a $P-$wave for $D_1 \to D_1\Phi$ and a $P-$ or $E-$wave for $D_2 \to D_2\Phi$. The corresponding lagrangian for the former reads

$$\begin{aligned}\mathcal{L}_{D_1D_1\Phi} =& \frac{3g_{3/2}}{2f_\pi} D_1^\nu D_1^{\beta\,\dagger} p^\alpha \\ & \times \left\langle (1+\not{v}_{D_1})\gamma_5(g^{\mu\nu} - \frac{1}{3}\gamma^\nu(\gamma^\mu - v_{D_1}^\mu))\gamma_\alpha\gamma_5(g^{\mu\beta} - \frac{1}{3}(\gamma^\mu - v_{D_1^\dagger}^\mu))\gamma_5(1+\not{v}_{D_1^\dagger})\right\rangle \\ \overset{\text{L.O.}}{=}& i\frac{20g_{3/2}}{3f_\pi} D_1^\nu D_1^{\beta\,\dagger} p^\alpha v^\delta \epsilon^{\alpha\beta\nu\delta} \\ =& i\frac{20g_{3/2}}{3f_\pi} D_1^i p^j D_1^{k\,\dagger}\epsilon^{ijk} .\end{aligned} \tag{1.102}$$

The vertex for the pion emission of the D_2 in a $P-$wave is given by

$$\begin{aligned}\mathcal{L}_{D_2D_2\Phi} =& -\frac{g_{3/2}}{4\sqrt{2}f_\pi} D_2^{\mu\nu} D_{2\,\mu\beta}^\dagger p^\alpha \left\langle (1+\not{v}_{D_2})\gamma_\nu\gamma_\alpha\gamma_5\gamma_\beta(1+\not{v}_{D_2^\dagger})\right\rangle \\ \overset{\text{L.O.}}{=}& i\frac{2g_{3/2}}{f_\pi} D_2^{\mu\nu} D_{2\,\mu\beta}^\dagger p^\alpha \epsilon^{\alpha\beta\nu\delta} \\ =& i\frac{2g_{3/2}}{f_\pi} D_2^{ij} p^k D_2^{il\,\dagger}\epsilon^{jkl} ,\end{aligned} \tag{1.103}$$

where $g_{3/2}$ is a free parameter to be determined in a fit.

1.5.5. Superfield $H\bar{H} \to c\bar{c}$ transition

We now come to the description of the doubly heavy vector fields of relevance to this study. In the case of a meson with two heavy quarks $\bar{Q}Q$, degeneracy is still expected under the rotation of both heavy quark spins, allowing us to write $\bar{Q}Q$ superfields just from the spin structure [46, 55]

$$\begin{aligned} J^{\mu_1\cdots\mu_l} =& \frac{1+\not{v}}{2}\left[H_{l+1}^{\mu_1\cdots\mu_l\alpha}\gamma_\alpha + \frac{1}{\sqrt{l(l+1)}}\sum_i \epsilon^{\mu_i\alpha\beta\gamma} v_\alpha \gamma_\beta H_{l\gamma}^{\mu_1\cdots\mu_{i-1}\mu_{i+1}\cdots\mu_l} \right. \\ &+ \frac{1}{l}\sqrt{(2l-1)(2l+1)}\sum_{i=1}^{l}(\gamma^{\mu_i}-v^{\mu_i})H_{l-1}^{\mu_1\cdots\mu_{i-1}\mu_{i+1}\cdots\mu_l} \\ &- \frac{2}{l\sqrt{(2l-1)(2l+1)}}\sum_{i<j}\left(g^{\mu_i\mu_j}-v^{\mu_i}v^{\mu_j}\right)\gamma_\alpha H_{l-1}^{\alpha\mu_1\cdots\mu_{i-1}\mu_{i+1}\cdots\mu_{j-1}\mu_{j+1}\cdots\mu_l} \\ &\left. + K^{\mu_1\cdots\mu_l}\gamma_5 \right]\frac{1-\not{v}}{2}\,. \end{aligned} \tag{1.104}$$

The $\ell = 0$ superfield $R^{(Q\bar{Q})}$ contains the $\{J/\psi,\eta_c\}$ doublet and can be expressed as

$$R^{(Q\bar{Q})} = \frac{1+\not{v}}{2}\left[J/\psi^\mu\gamma_\mu - \eta_c\gamma_5\right]\frac{1-\not{v}}{2}\,, \tag{1.105}$$

where the interaction with D/D^* is given by the Lagrangian

$$\mathcal{L}_{HHR} = \frac{g_{HHR}}{2}\langle R^{(Q\bar{Q})}\bar{H}_{2a}\overset{\leftrightarrow}{\partial}\!\!\!\!/\,\bar{H}_{1a}\rangle\,, \tag{1.106}$$

with $A\overset{\leftrightarrow}{\partial_\mu}B = A(\partial_\mu B) - (\partial_\mu A)B$. The resulting vertex factors are

$$\begin{aligned} V_{J/\psi DD} =& g_{J/\psi D\bar{D}}(\epsilon_{J/\psi}\cdot q) \\ V_{J/\psi D^*D} =& g_{J/\psi D^*\bar{D}} i\epsilon_{ijk}\epsilon^i_{J/\psi}\epsilon^j_{D^*}q^k \\ V_{J/\psi D^*D^*} =& -g_{J/\psi D^*\bar{D}^*}\left[(\epsilon_{J/\psi}\cdot\epsilon_2)(\epsilon_1\cdot q)\right. \\ & \left. -(\epsilon_{J/\psi}\cdot q)(\epsilon_1\cdot\epsilon_2) + (\epsilon_{J/\psi}\cdot\epsilon_1)(\epsilon_2\cdot q)\right]\,, \end{aligned} \tag{1.107}$$

with $q = k_1^{(Q)} - k_2^{(\bar{Q})} =$ denoting the relative residual momentum between the D mesons. At leading order the masses of the multiples are degenerate $m_{D^*} = m_D = m_H$ and q simplifies to $q = p_1 - m_H v - p_2 + m_H v = p_1 - p_2$. The coupling is traditionally parameterized as

$$g_{J/\psi AB} = \frac{m_{J/\psi}\sqrt{m_A m_B}}{m_D f_{J/\psi}}\,, \tag{1.108}$$

which includes the leading spin-symmetry violating effects via the mass factors. The $\ell = 1$ superfield $P^{(Q\bar{Q})}$ contains the spin triplet $\chi_{c0}, \chi_{c1}, \chi_{c2}$ and the singlet h_c

$$\begin{aligned} P^{(Q\bar{Q})\mu} = \frac{1+\not{v}}{2} \Bigg(& \chi_2^{\mu\alpha}\gamma_\alpha + \frac{1}{\sqrt{s}}\epsilon^{\mu\alpha\beta\gamma} v_\alpha \gamma_\beta \chi_{1\gamma} \\ & + \frac{1}{\sqrt{3}}(\gamma^\mu - v^\mu)\chi_0 + h_1^\mu \gamma_5 \Bigg) \frac{1-\not{v}}{2} \,. \end{aligned} \tag{1.109}$$

Due to the Proca-constraint, $P^\mu v_\mu$, the leading order Lagrangian for the interaction of the $\ell = 1$ spin-multiplet with D and D^* contains only a single term:

$$\mathcal{L}_{HHP} = i\frac{g_{HHP}}{2} \left\langle P^{(Q\bar{Q})\mu} \bar{H}_{2a} \gamma_\mu \bar{H}_{1a} \right\rangle \,. \tag{1.110}$$

From this the vertex factors evaluate to

$$\begin{aligned} V_{h_c D^* D} &= -2g^{h_c}(\epsilon^*_{D^*} \cdot \epsilon_{h_c}) \sqrt{m_{h_c} m_{D^*} m_D} \\ V_{h_c D^* D^*} &= 2ig^{h_c} \epsilon_{\alpha\beta\tau\sigma} m_{h_c} v^\alpha \epsilon^\beta_{h_c} \epsilon_1^{*\tau} \epsilon_2^{*\sigma} \sqrt{\frac{m^2_{D^*}}{m_{h_c}}} \\ &= 2ig^{h_c} \epsilon^{ijk} \epsilon^i_{h_c} \epsilon_1^{*j} \epsilon_2^{*k} \sqrt{m^2_{D^*} m_{h_c}} \,, \end{aligned} \tag{1.111}$$

where we fixed $\alpha = 0$. The coupling is parameterized as

$$g^{h_c} = -\frac{m_{\chi_{c0}}}{3} \frac{1}{f_{\chi_{c0}}} \,, \tag{1.112}$$

where $f_{J/\psi} = 416$ MeV was determined using vector-meson dominance (VMD) [56] and $f_{\chi_{c0}} = (510 \pm 40)$ MeV obtained from results of QCD sum rules [57]. Those parameters carry a systematic uncertainty which is difficult to quantify. We allow $f_{J/\psi}$ to vary within 10% of its value in the fits, while we fix $f_{\chi_{c0}}$ to its central value, since the fits of our initial study are not sensitive to this quantity.

1.5.6. Additional vertices

Photons couple via the field-strength tensor $F^{\mu\nu} = \partial_\mu A_\nu - \partial_\nu A_\mu$, where A_μ denotes the photon field. In this way gauge invariance is preserved automatically. The production of a vector resonance from a photon is thus described by

$$\mathcal{L}_{V\gamma} = \frac{e}{2f_V} V_{\mu\nu} F^{\mu\nu} \approx \frac{em_V^2}{f_V} V_\mu A^\mu \,, \tag{1.113}$$

where $V_{\mu\nu} = \partial_\mu V_\nu - \partial_\nu V_\mu$ and V denotes either the field for the $Y(4230)$ or the $\psi(4160)$. The implications of heavy quark spin symmetry on charmonium production

from photons are discussed later in Sec. 2.2.1, but as the production of the $Y(4230)$ must go via the broad $D_1(2430)$, we may allow for a complex phase at the vertex. For the decay of $Y(4230) \to X(3872)\gamma$ we can describe the E1 transition of D_1 going to $D^*\gamma$ with the following Lagrangian

$$\mathcal{L}_{TH\gamma} = \frac{c_a}{2}\langle T_a^i \bar{H}_a \rangle E^i \,, \tag{1.114}$$

where E^i denotes the electric component of the photon field.

1.6. Analiticity and unitarity

1.6.1. S-matrix theory

Considering a short ranged interaction, the S-matrix S is a unitary operator connecting asymptotically free initial $|i, \text{in}\rangle$ and final $|i, \text{out}\rangle$ particle states undergoing a scattering process, describing the time evolution from $t = -\infty$ to $t = \infty$

$$|i, \text{out}\rangle = S|i, \text{in}\rangle. \tag{1.115}$$

Generally for a two channel system it can be written as

$$S = \begin{pmatrix} \eta e^{2i\delta_1} & i\sqrt{1-\eta^2}e^{i(\delta_1+\delta_2)} \\ i\sqrt{1-\eta^2}e^{i(\delta_1+\delta_2)} & \eta e^{2i\delta_2} \end{pmatrix}, \tag{1.116}$$

where η denotes the elasticity of the process and δ_i the respective channels physical phase shift. The T-matrix T is defined as the non-trivial part of the S-matrix, containing all information of the interaction.

$$S_{ij} = \mathbb{1} + 2i\sqrt{\rho_i}T_{ij}\sqrt{\rho_j} \,, \tag{1.117}$$

with ρ being the two particle phase space defined in Eq. (1.75). The elasticity of the contemplated process can be expressed with the T-matrix by

$$\eta = \mod (1 + 2i\rho_1 T_{11}) \,. \tag{1.118}$$

S and T are analytical over the whole complex plane of the physical sheet up to branch cuts on the real axis required by unitarity and possible poles below threshold due to bound states. Every opening of a new threshold comes with a branch cut located at threshold energy s_{th} along the real axis, as shown in figure 1.4(a). The discontinuity of this so called right-hand cut is in terms of the T-matrix defined by

$$\text{disc}T(s) = \lim_{\epsilon \to 0^+} (T(s + i\epsilon) - T(s - i\epsilon)). \tag{1.119}$$

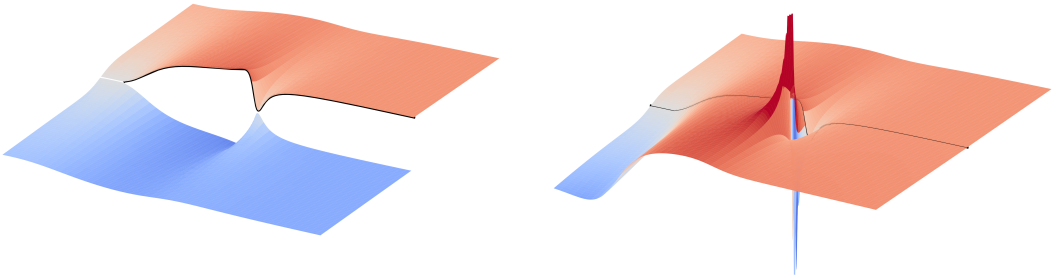

Figure 1.4.: The left plot shows a schematic depiction of the imaginary part of the first Riemann sheet of a T-matrix, the black line denotes the real axis ($+i\epsilon$). The right plot shows the imaginary part of the first Riemann sheet and the adjacent second Riemann sheet containing a resonance pole.

Using the Schwartz reflection principle for complex analytical functions

$$T(s^*) = T(s)^* \tag{1.120}$$

a relation between discontinuity and imaginary part is given by

$$\mathrm{disc}T(s) = T(s+i\epsilon) - T(s-i\epsilon) = T(s+i\epsilon) - T^*(s+i\epsilon) = 2i\mathrm{Im}\left(T(s)\right). \tag{1.121}$$

For the opening of a threshold involving unstable particles the corresponding branch cut moves into the complex plane. The branch point itself shifts according to the particles width, as demonstrated in the right plot of figure 1.5. To be precise, the branch point is split in two in accordance with the Schwartz reflection principle. However, the second branch point has negligible influence on the real axis for a remote threshold. The imprint of the relevant cusp on the real axis appears smoother the greater the width of the particle is, as demonstrated in figure 1.6. In general such T-matrix can also contain a left-hand cut due to crossing symmetry, opening at some energy s_{left} going to negative ∞.

Resonances manifest themselves as poles on the adjacent second Riemann sheet, also called unphysical sheet as shown in figure 1.4(b). The position s_{p} of these poles contain information about mass m and decay width Γ of the corresponding resonance

$$\sqrt{s_{\mathrm{p}}} = m - i\frac{\Gamma}{2}. \tag{1.122}$$

The unitarity of the S-matrix is directly linked to the conservation of probability P, which for a transition from $|\mathrm{in}\rangle$ to $|\mathrm{out}\rangle$ states is given by

$$P = |\langle \mathrm{in}|\mathrm{out}\rangle|^2 = |\langle \mathrm{in}|S|\mathrm{in}\rangle|^2. \tag{1.123}$$

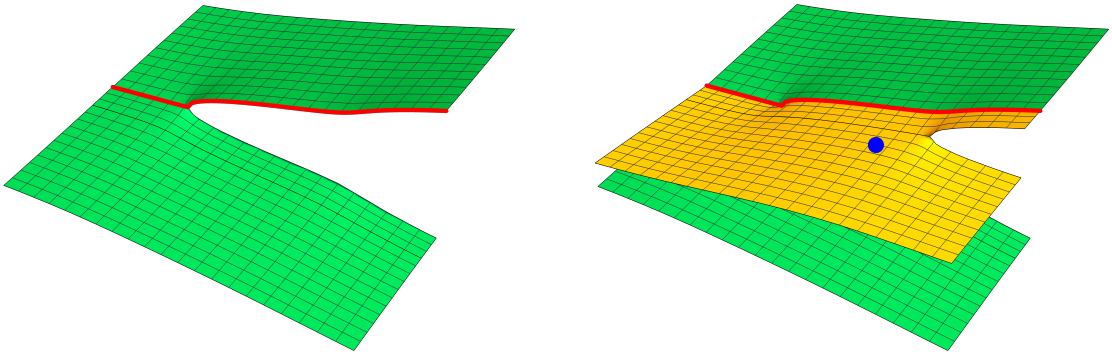

Figure 1.5.: Schematic depiction of the imaginary part of a 2 channel T-matrix. The left plot shows the physical sheet with respect to the lower threshold in green, which generates a branch cut on the real axis. The right plot additionally shows the physical sheet with respect to the second threshold involving unstable particles in yellow. The width of the constituents shift the branch point in the complex plane. The blue dot corresponds to a bound state pole of the second threshold.

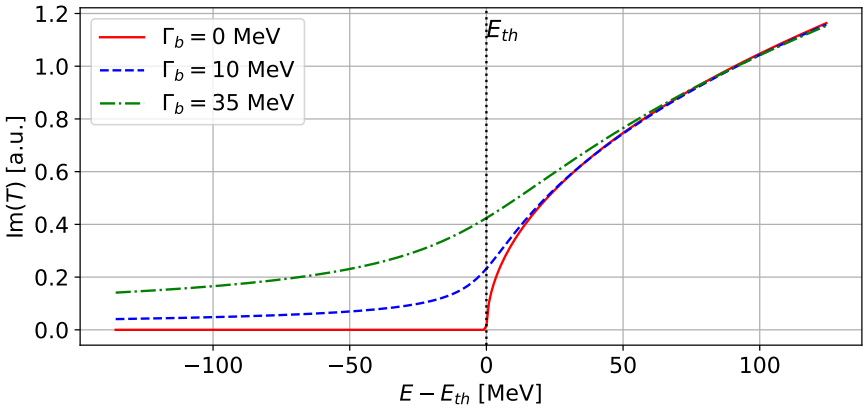

Figure 1.6.: Imaginary part of the T-matrix evaluated on the real axis at the threshold of some particles a, b for varying width Γ_b of particle b.

From the elastic unitarity of the S-matrix a condition constraining the T-matrix can be found

$$S^\dagger S = \mathbb{1} \rightarrow \mathrm{Im}\,(T^{-1}) = -\rho, \tag{1.124}$$

which is analogous to the optical theorem in a single channel case

$$\mathrm{Im}\,(T) = T^\dagger \rho T. \tag{1.125}$$

1.6.2. Dispersion theory

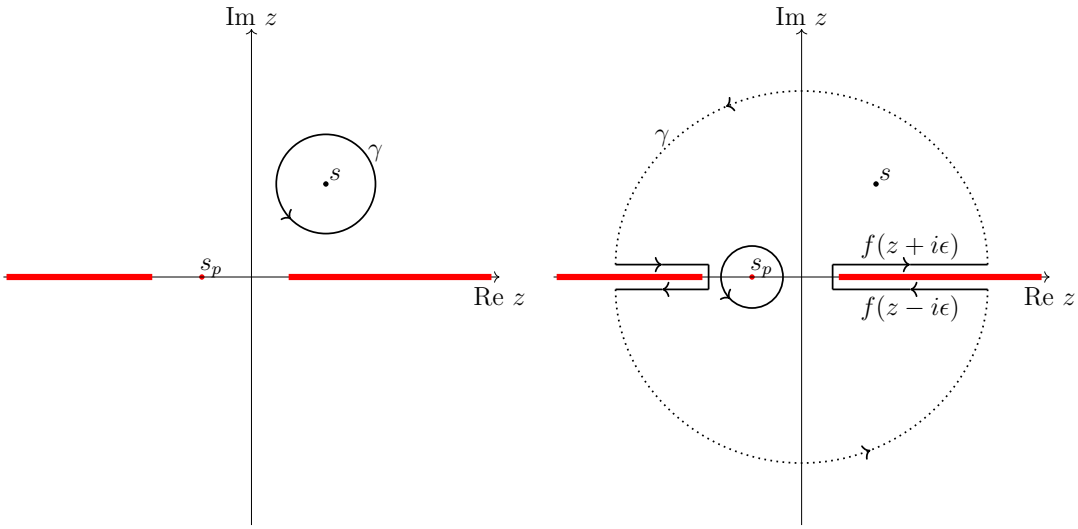

Figure 1.7.: Contour γ for f(z) in the presence of a discontinuity on the positive and negative real axis marked by red, as well as a pole at $z = s_p$. The left plot shows the initial contour that is deformed according to the right plot.

Dispersion theory is a powerful non-perturbative tool enabling one to calculate a unitary and casual function $f(s)$ from just its imaginary part and residues of eventually present bound states [58]. To obey unitarity and causality the function has to be analytic in the whole complex plane with exception of the branch cut on the real axis and potential bound state poles. The discontinuity of the function can be related to the imaginary part using the Schwartz reflection principle. The residues of bound states will be omitted below as they do not occur in $\pi\pi$ scattering relevant to this work. Expressing $f(s)$ in terms of a Cauchy integral gives

$$f(s) = \frac{1}{2\pi i} \oint_\gamma \mathrm{d}z \frac{f(z)}{z-s}, \tag{1.126}$$

where γ is a closed path. Here the function f must be holomorphic in the area enclosed by γ.
As $f(s)$ is analytic except for the branch cuts and poles on the real axis, the integration path can be deformed as shown in figure 1.7. We omit residues of potential bound state in the calculation below, as they do not occur in $\pi\pi$ scattering. Under the assumption that for $|z| \to \infty : f(z) \to 0$, the arc contribution will vanish and the function can be expressed by

$$\begin{aligned} f(s) &= \frac{1}{2\pi i}\oint_\gamma \mathrm{d}z \frac{f(z)}{z-s} = \frac{1}{2\pi i}\left(\oint_{s_{\mathrm{th}}}^{\infty} \mathrm{d}z \frac{f(z+i\epsilon)}{z-s} + \oint_{\infty}^{s_{\mathrm{th}}} \mathrm{d}z \frac{f(z-i\epsilon)}{z-s}\right) \\ &= \frac{1}{2\pi i}\oint_{s_{\mathrm{th}}}^{\infty} \mathrm{d}z \frac{f(z+i\epsilon) - f^*(z+i\epsilon)}{z-s} = \frac{1}{2\pi i}\oint_{s_{\mathrm{th}}}^{\infty} \mathrm{d}z \frac{\mathrm{disc} f(z)}{z-s}. \end{aligned} \tag{1.127}$$

Expressing the discontinuity via the imaginary part gives the relation

$$f(s) = \frac{1}{\pi}\oint_\gamma \mathrm{d}z \frac{\mathrm{Im}\, f(z)}{z-s}. \tag{1.128}$$

If the convergence of $f(s)$ is not sufficiently fast resulting in $f(z) \to$ const. for $|z| \to \infty$ one can subtract the dispersion integral

$$\tilde{f}(s) = \frac{f(s) - f(s_0)}{s - s_0}, \tag{1.129}$$

with the subtraction point $s_0 < s_{\mathrm{th}}$, such that $\mathrm{disc} f(s_0) = 0$. If the convergence is now fast enough, one can write a relation for $\tilde{f}(s)$

$$\tilde{f}(s) = \frac{1}{\pi}\int_{s_{\mathrm{th}}}^{\infty} \frac{\mathrm{Im}\, \tilde{f}(z)}{z-s}\mathrm{d}z = \frac{1}{\pi}\int_{s_{\mathrm{th}}}^{\infty} \frac{\mathrm{Im}\, f(z)}{(z-s)(z-s_0)}\mathrm{d}z. \tag{1.130}$$

Rearranging equation (1.129), one obtains the once-subtracted dispersion integral for $f(s)$

$$f(s) = f(s_0) + \frac{s-s_0}{\pi}\int_{s_{\mathrm{th}}}^{\infty} \frac{\mathrm{Im}\, f(s)}{(z-s)(z-s_0)}\mathrm{d}z, \tag{1.131}$$

where $f(s_0)$ is the subtraction constant. If the function still does not converge properly, one can iterate this procedure at the cost of additional parameters in the form of a subtraction polynomial.

1.6.3. Homogeneous Omnés problem

In general such function can contain left-hand cuts from crossing-symmetry, however, for now we only consider the right-hand cuts, the so-called Homogeneous Omnés problem. We consider $f(s)$ to be a two-particle amplitude with definite isospin and angular momentum. By unitarity, the discontinuity at the right-hand cut of such a function in the elastic regime must be given by

$$\mathrm{disc} f = 2iT^*\rho f, \tag{1.132}$$

where T denotes the elastic on-shell scattering matrix with phase shift δ. Since the discontinuity is purely imaginary and the phase space ρ is real above threshold, it follows that $T^* f \in \mathbb{R}$. Therefore, T and f must share the same argument and one can express $f(s)$ in the elastic regime in terms of the corresponding scattering phase shift $\delta(s)$

$$f(s) = |f(s)|e^{i\delta(s)}, \tag{1.133}$$

which is known as Watson's theorem [59]. Finding a solution for this function is called the Omnès problem [60]. Assuming $\Omega(s)$ to be such a solution, $P(s) \cdot \Omega(s)$ with a polynomial $P(s) \in \mathbb{R}$ also fulfills the relation. Further, if $\Omega(s)$ is free of zeros one may study the logarithm with discontinuity

$$\mathrm{disc}(\log(\Omega(s))) = 2i\delta(s). \tag{1.134}$$

Using the dispersion relation (1.131) and choosing the subtraction point to be $s_0 = 0$, one obtains

$$\Omega(s) = \exp\left(\frac{s}{\pi}\int_{s_{\mathrm{th}}}^{\infty} \frac{\delta(z)}{z(z-s)}\mathrm{d}z\right), \tag{1.135}$$

where $\Omega(s)$ is the so called Omnès function, which by convention is normalized to $\Omega(s_0) = 1$. Using a phase shift which converges to a finite value $\lim\limits_{s\to\infty} \delta(s) = c$ fixes the high-energy behaviour of the Omnès function to be $\lim\limits_{s\to\infty} \Omega(s) \to s^{-c/\pi}$.

1.6.4. Inhomogeneous Omnés problem

For the inhomogeneous Omnés problem the left-hand cuts from crossed channels are considered in addition to the right-hand cuts. It is convenient to isolate the left-hand cut of the scattering amplitude f by writing

$$f(s,z) = M(s,z) + I(s,z)\,, \tag{1.136}$$

where $M(s,z)$ only contains right-hand cuts and all left-hand cuts are contained in $I(s,z)$, the so-called *inhomogeneity*. The same separation is still valid for the partial-wave projected amplitudes f_L

$$f(s,z) = \sum_l (2l+1) f_l(s) P_l(z), \quad \text{with } f_l(s) = M_l(s) + I_l(s)\,. \tag{1.137}$$

From unitarity the discontinuity along the right-hand cut is given by

$$\mathrm{disc}_R\, \Omega_{L\,ij}(s) = \sum_k 2i T^*_{L\,ik}(s)\sigma_k(s)\Omega_{L\,kj}\,, \tag{1.138}$$

where $\sigma_k = \sqrt{1-(4m_k^2/s)}\Theta(s-4m_k^2)$ and $i,j,...$ denote the indices of the coupled channels. One may now define the quantity

$$\mathcal{I}_l(s) = \Omega_l^{-1}(s) M_l(s) = \Omega^{-1}(s)\left(f_l(s) - I_l(s)\right) , \tag{1.139}$$

which does not contain any left-hand cuts. Following the ansatz that $\mathrm{disc}_R\, I_l = 0$, the discontinuity of $\mathcal{I}$ can be expressed by

$$\begin{aligned} \mathrm{disc}_R\, \mathcal{I}_L &= \Omega_l^{-1} M_L - \Omega^{-1\,*} M_L^* + \Omega^{-1\,*} M_L^- \Omega^{-1\,*} M_L^* \\ &= -\Omega^{-1\,*} \mathrm{disc}_R\, \Omega^{-1} M_l + \Omega^{-1\,*} \mathrm{disc}_R\, (f_l - I_l) \\ &= 2i\Omega^{-1\,*} T_L \rho I_l - \Omega^{-1\,*} \mathrm{disc}_R\, I_l \\ &= 2i\Omega^{-1\,*} T_L \rho I_l \,, \end{aligned} \tag{1.140}$$

where the coupled channel indices are dropped to simplify notation. Solving both Ω_l and T_l using their respective discontinuity equation

$$\begin{aligned} \Omega^{-1\,*} &= (1 - 2iT_l^*\rho) \\ T_l^* &= (1-2iT_l^*\rho)^{-1} T_l \,, \end{aligned} \tag{1.141}$$

the discontinuity of $\mathcal{I}_l$ may be written as

$$\mathrm{disc}_R\, \mathcal{I}_l = 2i\Omega_l^{-1} T_l \rho I_l \,. \tag{1.142}$$

In general the inhomogeneity I_l can introduce additional branch cuts. However, assuming that the branch points lie on unphysical sheets, $\mathcal{I}_l$ can be reconstructed dispersively

$$\left(\mathcal{I}_l(s)\right)_j = \left(\mathcal{P}_{n-1}(s)\right)_j + \sum_{km} \frac{s^n}{\pi} \int \frac{\mathrm{d}z}{z^n} \frac{\Omega_{jk}^{-1}(z) T_{km}(z) \sigma_m(z) \mathcal{M}_m^0(z)}{z-s} \,, \tag{1.143}$$

resulting in

$$M_l(s) = \sum_k \Omega_{jk} \left[\left(\mathcal{P}_{n-1}\right)_k + \sum_{lm} \frac{s^n}{\pi} \int \frac{\mathrm{d}z}{z^n} \frac{\Omega_{kl}^{-1}(z) T_{lm}(z) \sigma_m(s) \mathcal{M}_m^0(z)}{z-s} \right] , \tag{1.144}$$

where $\mathcal{P}_{n-1}$ is the subtraction polynomial of order $n-1$.

2. The $Y(4230)$ as a $D_1\bar{D}$ molecule

This chapter is largely built on our publication [61].

2.1. Introduction

Following the discovery of the first exotic state in the $\bar{c}c$-sector in 2003, the $\chi_{c1}(3872)$, also referred to as $X(3872)$, many more states in the charmonium and bottomonium mass range have been discovered showing properties that defy predictions from the original quark model. For recent reviews see, e.g., Refs. [25, 26, 62–65]. Data in the $J^{PC} = 1^{--}$ channel is particularly rich, as states containing $\bar{c}c$ can be created directly in e^+e^--collisions, allowing for a straightforward study in experiments such as BaBar, Belle, and BESIII. This chapter focuses on the vector states in the mass range from 4.2 to 4.35 GeV, which hosts most prominently the $\psi(4230)$ also known as $Y(4230)$. BESIII claims an additional state located at 4.32 GeV to account for the highly asymmetric line shape in the reaction $e^+e^- \to J/\psi\pi^+\pi^-$ [66, 67]. In particular, their most recent analysis [67] revealed for the Breit-Wigner mass and width of the $Y(4230)$ in this channel

$$\begin{aligned} M_{Y(4230)} &= 4221.4 \pm 1.5 \pm 2.0 \text{ MeV} \\ \Gamma_{Y(4230)} &= 41.8 \pm 2.9 \pm 2.7 \text{ MeV} , \end{aligned} \tag{2.1}$$

and for the $Y(4320)$

$$\begin{aligned} M_{Y(4320)} &= 4298 \pm 12 \pm 26 \text{ MeV} \\ \Gamma_{Y(4320)} &= 127 \pm 17 \pm 10 \text{ MeV} , \end{aligned} \tag{2.2}$$

where the first and second uncertainty is statistical and systematic, respectively. The $Y(4320)$ is also necessary in their analysis of the $J/\psi\pi^0\pi^0$ channel [68], where the parameters shown above are consistent with the data in this channel. However, the $Y(4230)$ is in total seen in eight additional channels shown in Fig. 2.1, with admittedly largely inconsistent resonance parameters. However, the state $Y(4320)$ shows up in none of them, at least within the mass range consistent with Eq. (2.2), not even in $e^+e^- \to J/\psi K\bar{K}$ which is directly related to $e^+e^- \to J/\psi\pi\pi$ by the approximate SU(3) flavor symmetry of QCD.
The BaBar and Belle experiments reported an additional potential state with a mass of about 4345 MeV, named $Y(4360)$, in the $\psi(2S)\pi^+\pi^-$ [77, 78] final state.

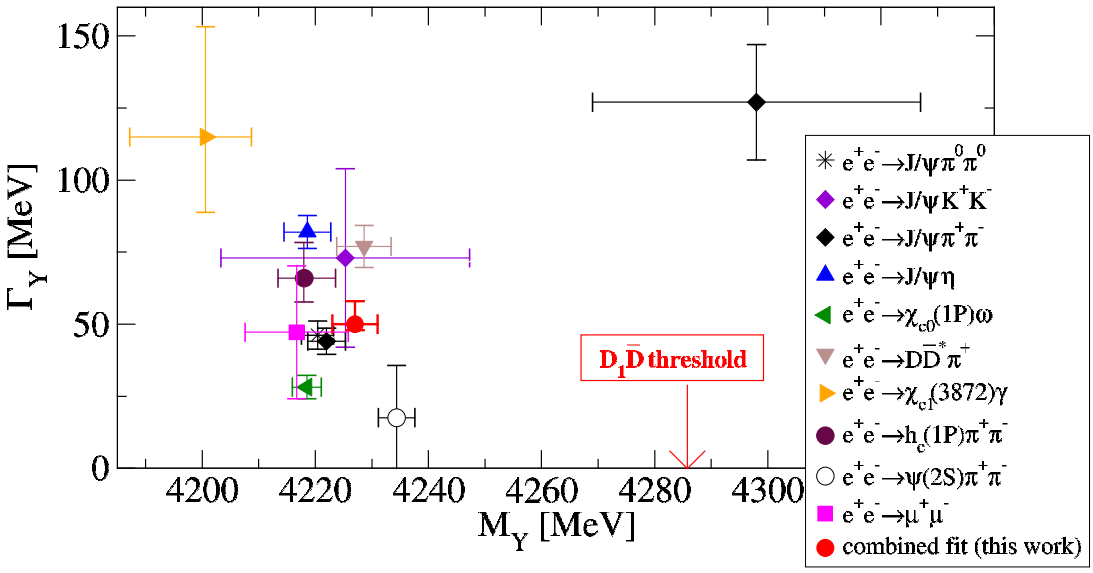

Figure 2.1.: Mass and width of the two Y-states discussed in the introduction as extracted from the experimental analyses of the individual channels shown by the labels. All data below a mass value below 4240 MeV is interpreted a $Y(4230)$ and the one data point above refers to the $Y(4320)$. The experimental values are taken from [67–76]. The red dot denotes the pole location for the $Y(4230)$ as extracted in this thesis.

In experiments by BaBar and Belle a state named $Y(4360)$, with a mass of about 4345 MeV, was discovered in the $\psi(2S)\pi^+\pi^-$ [77, 78] final state. However, the recent BESIII measurement of the same channel revealed that the $Y(4360)$ emerges due to a subtle interference of the $Y(4230)$ and a state at 4390 MeV with a width of 140 MeV [75], which is thus in a mass range close to the $\psi(4415)$, although, twice as wide. A signal at 4390 MeV with consistent parameters was also observed by BESIII in the $h_c\pi\pi$ [73] and $J/\Psi\eta$ [69] final states. As this state is outside of the energy range studied in this chapter, we do not discuss it here any further.

In the mass range from 4.2 to 4.35 MeV these results raise the following questions:

1. Why do the resonance parameters for the $Y(4230)$ scatter so much in the different final states? Even for the two data sets with the highest statistic, the observed width of the $Y(4230)$ deduced from the $D\bar{D}^*\pi$ channel is almost twice as large as the width determined from the $J/\psi\pi\pi$ channel [71]?

2. What can we learn from the cross section differences for $Y(4230)$ in its various decay channels? Note that the cross section in the $D\bar{D}^*\pi$ channel is about one order of magnitude larger than those of hidden charm decays.

3. With regard to the previous point, why is the observed count rate for $Y(4230)$ in final states with both $\bar{c}c$ spin 1 (i.e. $J/\psi\pi\pi$ and $\psi'\pi\pi$ channels) and $\bar{c}c$ spin 0 (i.e. $h_c\pi\pi$ channel) of similar order, despite the production via a photon only allowing for $\bar{c}c$ in spin 1? Can we understand this seemingly large violation of heavy quark spin symmetry?

4. Why is the $Y(4320)$ seen only in a single final state?

5. Can the apparent asymmetry of the $J/\psi\pi^+\pi^-$ line shape be generated by the opening of the $D_1(2420)\bar{D}$ channel just below the nominal mass of the $Y(4320)$? Here the $D_1(2420)$ is the narrow axial vector with a width of about 30 MeV, which decays into πD^* predominantly in D-wave. The nearby $D_1(2430)$ has a width of about 300 MeV and decays to the πD^* channel predominantly in S-wave. Thus, the broad D_1 is not capable of producing structures as narrow as those discussed here, although its mixing with the narrow D_1, emerging from spin symmetry violation, is relevant for the production of the $Y(4320)$.

In this chapter we address the mentioned issues starting from the assumption that the $Y(4230)$ is a $D_1(2420)\bar{D}$ hadronic molecule, proposed originally in Ref. [79], and refined in Ref. [80] by taking the $D_1\bar{D}$ cut properly into account and the triangle singularity mechanism, which is crucial for the production of the $Z_c(3900)$.

2.1.1. Different structure assumptions

Before we lay out the observable consequences of a molecular nature in detail, we present other possible structure assumptions put forward in the literature, namely the hybrid, the hadrocharmonium and the compact tetraquark interpretation, as well as studies that do not require a pole of the $Y(4230)$ at all. The details will be discussed in the following paragraphs, where we demonstrate the specific and significant implications of a molecular structure of the $Y(4230)$. For a general introduction to the different binding mechanisms see the recent review Ref. [26].

Hadrocharmonium

In the hadrocharmonium picture exotic hidden charm states are viewed as a compact $\bar{c}c$ state surrounded by a typically excited light quark cloud [81].
The main differences to the molecular picture in the context of the $Y(4230)$ are already discussed in Ref. [82]. The $Y(4230)$ as a hadrocharmonium state naturally

explains its decay into final states that contain charmonium with additional light quarks and the decoupling to $D^{(*)}\bar{D}^{(*)}$ channel, which would be expected for a standard charmonium quark-model state. However, it appears at odds with the previously mentioned fact that the $Y(4230)$ is also observed in $\bar{c}c$ spin 0 final states like $h_c\pi\pi$, as HQSS calls for a conservation of the heavy quark spin. To overcome this contradiction Ref. [83] proposed the $Y(4230)$ emerges from the mixing of two states, one with a spin 0 and one with a spin 1 $\bar{c}c$ core. This scenario calls for an additional nearby vector state, with the aforementioned $Y(4320)$ being a good candidate. Furthermore, this mixing scenario implies the existence of four spin symmetry partners [84]. For example, there should be two exotic η_c states, one in between the two vector states, one significantly lighter than the $Y(4230)$. In this picture, it is difficult to understand why the cross section $Y(4230) \to D\bar{D}^*\pi$ is large.

Hybrid

The first theoretical works after its discovery proposed the $Y(4230)$ to be a hybrid state based either on phenomenological calculations [85–87] or heavy quark effective field theory [88]. For a hybrid state in addition to quarks also gluons contribute to the valence degrees of freedom. Ref. [89] investigated the dacays of heavy quarkonium hybrids into conventional heavy quarkonia, disfavoring a pure hybrid interpretation of the $Y(4230)$ [89]. Similar to the hadrocharmonium picture the hybrid scenario requires the mixing of two close-by vectors states with different spin of the $\bar{c}c$ component. This again calls for the existence of both the $Y(4230)$ and $Y(4320)$ to explain the transitions to heavy quarkonia with spin 1 and spin 0. Additionally, by exploiting the SU(3) flavor symmetry between $J/\psi\pi\pi$ and $J/\psi K\bar{K}$, the rate of the latter in a hybrid decay is larger than what was found in experiment.

Compact tetraquark

In the compact tetraquark picture the states are typically made of heavy-light diquarks and anti-diquarks. This approach calls for four non-strange vector states with masses in the range 4220 MeV and 4660 MeV [90, 91], since the diquarks can have either spin one or spin zero allowing for the following spin couplings with positive C parity, $[0,0]_0$, $[1,0]_1 + [0,1]_1$, $[1,1]_0$, $[1,1]_2$, with the spins of diquark and antidiquark in the brackets and their total spin as subindex outside — note that a state that contains two spin 1 substructures coupled to total spin 1 has negative C parity. To get the negative parity needed for a vector state, an angular momentum of 1 needs to be introduced between the diquark and antidiquark that in addition flips the C parity to the needed -1. For example, the currently preferred fit of Ref. [90] includes both $Y(4230)$ as well as $Y(4320)$. An alternative approach to compact tetraquarks, similar in spirit, but different in the realization, is outlined in Ref. [92].

Thus, we see that three of the non-molecular scenarios prefer the presence of both $Y(4230)$ and $Y(4320)$.

No pole scenario

For the scenarios requiring no pole the structure of the $Y(4230)$ is generated either by an interference effects of the well established vectorcharmonia or their strong coupling to a nearby multi-hadron threshold. In Refs. [93, 94] the structure near $\sqrt{s} = 4230$ MeV is generated from a strong coupling of the $Y(4230)$ to the $D_s^* \bar{D}_s^*$ channel, which threshold lies roughly at 4225 MeV. This indeed provides a reasonable description of the $J/\psi\pi^+\pi^-$ data, however, no other channels are investigated and it is unlikely that such a scenario allows a simultaneous description the other final states, especially the $D\bar{D}^*\pi$ channel. The same statements apply to Ref. [94], where the $Y(4230)$ is generated from an interference of the neighbouring charmonium states. We therefore do not consider these mechanisms any further.

2.1.2. General considerations

As we only consider the $D_1\bar{D}$ channel for now and include the contributions of the $D_1\bar{D}^*$ and $D_2\bar{D}^*$ channels in a subsequent study (see Sec. 3), we first limit the analysis to the energy range from 4.2 GeV to 4.35 GeV. The goal of this study is to demonstrate that the available data in this mass range are consistent with the presence of a single exotic state predominantly of molecular nature, which is reflected in a large coupling to the $D_1\bar{D}$ channel as shown in section 1.4. For this we perform a combined analysis of eight different final states produced in e^+e^- annihilation, namely $D^0D^{*-}\pi$, $J/\psi\pi^+\pi^-$, $J/\psi K^+K^-$, $h_c\pi^+\pi^-$, $\mu^+\mu^-$, $\chi_{c0}(1P)\omega$, $J/\psi\eta$ and $X(3872)\gamma$, under the assumption that the $Y(4230)$ is a $D_1\bar{D}$ molecule.
The molecular scenario for the $Y(4230)$ was already advocated in Refs. [95, 96] based on an analysis of older data in the $J/\psi\pi\pi$ and $h_c\pi\pi$ channels. It is crucial to emphasize that, while certain properties of the data emerge naturally in the current analysis, there are cases where fine-tuned parameters are necessary. Moreover, to obtain a coherent picture, it is unavoidable to include the interference with an additional vector state whose properties we fix to those of the well-known charmonium state $\psi(4160)$, discussed in section 2.2.3.
Since this work is considered exploratory, a few disclaimers must be given. These will be overcome in our subsequent project, which is presented in section 3.

- We treat the effect of the interference of the $\psi(4160)$ with the $Y(4230)$ perturbatively. While this simplifies the fitting, it violates unitarity since only terms linear in the vector propagators are included in the evaluation of the hadronic cross sections.

- To accelerate the fitting, we approximate the imaginary parts in the denominators of the resonance propagators for $\psi(4160)$, $Y(4230)$, and $Z_c(3900)$. Specifically, we keep dynamically the most significant imaginary parts that exhibit strong energy dependence within the considered mass range. Contributions from more distant channels that show minimal changes are replaced by constants. Details are given in the Sec. 2.2.1-2.2.3.

- This is a phenomenological study. In particular, we cannot estimate uncertainties from a truncation error in some systematic expansion. The triangle singularity present in the production of the Z_c is embedded in a 3-body phase space, discussed in section 2.2.2. There are certain kinematic regions close to the $D^*\bar{D}$ threshold where the triangle diagrams have significant contributions, however, over a large portion of the phase space these contributions are subleading. Further, the $D_1(2430)$ has a non-negligible width, whose proper inclusion in a power counting scheme has to be discussed. The current aim is to demonstrate what is possible with a single molecular particle in the mass range of interest.

- We focus on the effect of the $D_1\bar{D}$ intermediate state in the decays of the $Y(4230)$, ignoring that heavy quark spin symmetry also calls for the coupled channels $D_1\bar{D}^*$ and the $D_2\bar{D}^*$. This is the main limiting factor of our initial study when considering the energy range.

- The channels with two pions or two kaons in the final states necessitate the proper inclusion of $\pi\pi/K\bar{K}$ final-state interactions, as discussed in previous works [97–101]. In this study, we simplify the treatment of these effects presented in section 2.4.

- The data for $e^+e^- \to \psi(2S)\pi\pi$ [75], exhibit a very unusual energy dependence in the $\psi(2S)\pi$ invariant mass distributions at $\sqrt{s} = 4230$ and 4260 MeV [102], which seem to require a more refined treatment. Further, the signal of the $Y(4230)$ in the $\psi(2S)\pi\pi$ cross section appears way less prominent than the peak structure around 4380 MeV. Consequently, data from $e^+e^- \to \psi(2S)\pi\pi$ are not included in the current fits.

- The data currently available do not show apparent peak structures of $Y(4230)$ in $D^{(*)}\bar{D}^{(*)}$ channels, which must appear in odd partial waves to reach $J^{PC} = 1^{--}$. This suggests that the couplings of $Y(4230)$ to the two-body open charm channels are much smaller than those of the vector charmonium states. In Ref. [103] it was demonstrated that the dips seen in the data of $e^+e^- \to D^*\bar{D}^*$ and $D_s^*\bar{D}_s^*$ are consistent with interference from the $D_1\bar{D}$ molecular nature of the $Y(4230)$. We thus do not include these channels these channels here, which would call for the inclusion of additional $\bar{c}c$ resonances.

Note that with respect to the implications of the heavy quark spin symmetry there are more advanced studies than the one presented in this chapter already published [104, 105]. However, both those works focus solely on the pole locations that emerge from solving the scattering equations for the members of the spin multiplet $\{D_1, D_2\}$ scattering off those of $\{\bar{D}, \bar{D}^*\}$, where the pole locations were obtained from Breit-Wigner fits performed by the experimental groups. No attempt is made to investigate the resulting line shapes in the various decay channels. Contrary to those works, we here study the energy dependence of the cross sections in the various decay channels. This allows us to demonstrate that the inclusion of the $\psi(4160)$ together with the strong coupling of the $Y(4230)$ to the $D_1\bar{D}$ channel that is a consequence of its assumed molecular nature, is sufficient to describe all data sets studied here without the need for an additional exotic state in the mass range of interest. This conclusion is in line with the preliminary results of this study announced in Ref. [106].

Ref. [107] includes the same degrees of freedom as our initial study presented here. The central finding of this section is that in the energy range relevant to our work three poles are needed. While one of them might well represent the $\psi(4160)$, only with somewhat shifted parameters, and another one the $Y(4230)$, there is still a resonance needed close to 4320 MeV, absent in our analysis. A more detailed comparison will only be possible, once more details are published.

An alternative analysis, which includes both the $\psi(4160)$ and the $Y(4230)$ in the energy range of interest, but does not require a state at 4320 MeV, is presented in Ref. [108]. In this work, the asymmetric shape observed in the total cross sections of $J/\psi\pi^+\pi^-$ and D^0D^{*-} can be reproduced as an interference effect between $\psi(4160)$ and the higher energy state $\psi(4415)$, where the latter state is beyond the energy range considered here. It is combined with a non-resonant background. The inclusion of the $Y(4230)$ is necessary for fine-tuning the agreement with data near 4.2 GeV. Another notable difference between this work and the previous one, as well as ours, is the omission of any threshold effects. As we demonstrate below, the significance of the $D_1\bar{D}$ threshold on the Y line shapes is a direct hint towards its molecular nature. Accordingly, Ref. [108] argues that their analysis is consistent with a $\bar{c}c$ structure of the $Y(4230)$. Thus studying observable differences between the results of that work and ours is important to pin down the nature of the $Y(4230)$. We come back to this when discussing the results in Sec. 2.6. It should also be mentioned that the relatively large cross section seen in $e^+e^- \to h_c\pi\pi$, where the final state contains a $\bar{c}c$ pair in spin zero, contrary to the production of a $\bar{c}c$ pair with spin one — suggests a considerable amount of heavy quark spin symmetry (HQSS) violation. This phenomenon is naturally explained in a molecular scenario for the Y, whereas it seems highly unnatural for a conventional $\bar{c}c$ structure.

2.2. Relevant resonances

2.2.1. $Y(4230)$

We can write the $D_1 D$ wavefunction as a negative $\mathcal{C}$-eigenstate

$$|D_1\bar{D}(\mathcal{C}=-1)\rangle = \frac{1}{\sqrt{2}}\left(|D_1\bar{D}\rangle - |D\bar{D}_1\rangle\right) . \tag{2.3}$$

As the $Y(4230)$ is produced by a $c\bar{c}$ pair from the initial photon vertex it must be an iso-singlet. Following the convention

$$\begin{array}{ll} |\frac{1}{2},+\frac{1}{2}\rangle = \bar{D}^0 = \bar{c}u & |\frac{1}{2},+\frac{1}{2}\rangle = -D^+ = -c\bar{d} \\ |\frac{1}{2},-\frac{1}{2}\rangle = D^- = \bar{c}d & |\frac{1}{2},-\frac{1}{2}\rangle = D^0 = c\bar{u} \end{array} \tag{2.4}$$

the iso-singlet wavefunction is given by $|I=0\rangle = 1/\sqrt{2}\,(|\uparrow\downarrow\rangle - |\downarrow\uparrow\rangle)$, resulting in

$$|D_1\bar{D}(\mathcal{C}=-1, I=0)\rangle = \frac{1}{2}\left(|D_1^+D^-\rangle + |D_1^0\bar{D}^0\rangle + |D^+D_1^-\rangle + |D^0\bar{D}_1^0\rangle\right) . \tag{2.5}$$

In the single channel analysis the effective Lagrangian for the coupling of $D_1\bar{D}$ to $Y(4230)$ and $D_1\bar{D}$ self-interactions reads [96]

$$\mathcal{L}_Y = \frac{g_{Y0}}{\sqrt{2}}(\bar{D}^\dagger Y^i D_1^{i\dagger} - \bar{D}_1^{i\dagger} Y^i D^\dagger) + g_1\left[(D_1^i\bar{D})^\dagger(D_1^i\bar{D}) + (D\bar{D}_1^i)^\dagger(D\bar{D}_1^i)\right] , \tag{2.6}$$

where the couplings g_{Y0} and g_1 include the heavy quark mass normalization of the fields. Usually, a proper field redefinition allows one to absorb the effect of non-perturbative hadron-hadron scattering into a pole term. This is not possible only if there is more than one pole in the mass range of interest [109]. As this is not the case here we can safely set the parameter g_1 to zero. We checked that the inclusion of this parameter does not allow us to significantly improve the fit, however, it leads to large correlations between g_{Y0} and g_1 slowing the fitting. In our subsequent study, the effective coupling of the $Y(4230)$ to $D_1\bar{D}$ and its spin partners will emerge from solving the full coupled channel Lippman-Schwinger equation.
For now the $D_1\bar{D}$ scattering potential is fixed by

$$V(E) = -\frac{g_{Y0}^2}{2} G_0(E) \tag{2.7}$$

where the bare Y propagator reads

$$G_0(E) = \frac{1}{2\omega_Y(E-m_0)} , \tag{2.8}$$

with ω_Y denoting the on-shell energy of the $Y(4230)$ from the field normalization. Here we dropped the spin indices although G_0 and various other propagators below refer to the propagation of a vector particle. The reason is that in our non-relativistic treatment, the spin structure is simply given by δ^{ij}, so the spin is unchanged.
The relation of the bare propagator $G_0(E)$ to the full propagator $G_Y(E)$ is given by the Dyson equation

$$G_Y = G_0 + G_0 g_{Y0}(2\omega_Y \Sigma_{D_1 D}) g_{Y0} G_Y \,. \tag{2.9}$$

From this we find for the $D_1\bar{D}$ scattering amplitude

$$\mathcal{M}_{D_1\bar{D}\to D_1\bar{D}} = -\frac{g_{Y0}^2}{2} G_Y(E) \,, \tag{2.10}$$

with

$$G_Y(E) \;=\; \frac{1}{2\omega_Y} \frac{1}{E - m_0 - g_{Y0}^2 \Sigma_{D_1 D}(E) + i\Gamma_{\text{in}}/2}. \tag{2.11}$$

Note that the last term in the denominator was added to account for the contribution to the width of the $Y(4230)$ from the various inelastic channels. A justification for this treatment is given in the following section about the $Z_c(3900)$.

The self-energy Σ for a resonance R can be derived from the standard, scalar one-loop diagram, which can be dispersively reconstructed from its discontinuity $\text{disc}\Sigma_a = 2i\sigma_a$ for a two-body state a. In dimensional regularization it reads

$$\begin{aligned}
2\omega_R \tilde{\Sigma}_a^L(s) =& a - \frac{s - s_0}{\pi} \int_{s_{\text{th}}}^{\infty} \mathrm{d}s' \frac{\nu(s')^L \rho(s')}{(s' - s)(s' - s_0)^{L+1}} \\
2\omega_R \tilde{\Sigma}_a^0(s) =& \frac{1}{(4\pi)^2} \left[\tilde{a}(\mu) + \log\left(\frac{m_{a2}^2}{\mu^2}\right) + \frac{m_{a2}^2 - m_{a1}^2 + s}{2s} \log\left(\frac{m_{a1}^2}{m_{a2}^2}\right) \right. \\
& \left. + \frac{\lambda^{1/2}(s, m_{a2}^2, m_{a1}^2)}{2s} \log\left(\frac{m_{a2}^2 + m_{a1}^2 - s + \lambda^{1/2}(s, m_{a2}^2, m_{a1}^2)}{m_{a2}^2 + m_{a2}^2 - s - \lambda^{1/2}(s, m_{a2}^2, m_{a1}^2)} \right) \right] ,
\end{aligned} \tag{2.12}$$

where $\tilde{a}$ denotes the subtraction constant and μ the renormalization scale. The effect of the terms $\tilde{a} + \log(m_{a2}^2/\mu^2) \in \mathbb{R}$ will be absorbed in the renormalization of the pole. The masses in the expression refer to the masses of the two particles propagating in channel a. Analogously, the scalar one-loop diagram can also be derived from time-ordered perturbations theory, resulting in

$$\begin{aligned}
2\omega_R \tilde{\Sigma}_a^{\text{TOPT}}(E, p) &= \int \frac{\mathrm{d}^3 l}{(2\pi^2)} \frac{1}{4\omega_{a1}(p, l, z)\omega_2(l)} \frac{1}{E - \omega_{a1}(p, l, z) - \omega_{a2}(l)} \\
&= \frac{1}{(2\pi)^2} \int \mathrm{d}l \; \frac{l}{4\omega_{a2}(l)} \log\left[\frac{E - \omega_{a1}(p, l, z) - \omega_2(l)|_{z=1}}{E - \omega_{a1}(p, l, z) - \omega_{a2}(l)|_{z=-1}} \right]
\end{aligned} \tag{2.13}$$

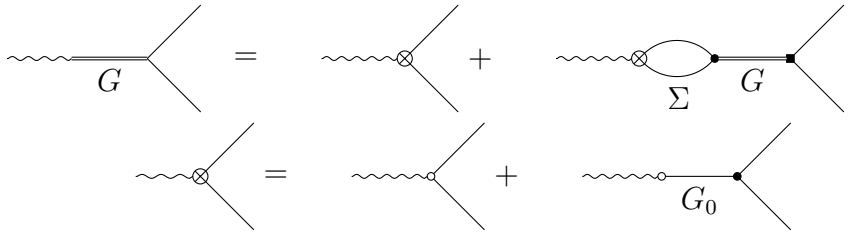

Figure 2.2.: The $Y(4230)$ induced production of the $D_1\bar{D}$ pairs from a pointlike source. The solid lines denote D_1 and D mesons as well as the bare propagator G_0, double line stands for the dressed propagator of the Y(4230), and the wiggly line corresponds to the initial photon.

for an external momentum p, where the radial integration has to be performed numerically. The derivation is analogous to the one presented in appendix B for the triangle loop. Equation (2.12) and (2.13) are identical in the limit $p \to 0$. However, even though the expression derived from time-order perturbation theory contains an explicit integral, its numerical evaluation is actually faster when performed properly due to the multiple log and square root functions in Eq. (2.12).
The actual expression of the self-energies that enter the propagators is

$$\Sigma_a(s) = \tilde{\Sigma}_a(s) - \mathrm{R}e(\tilde{\Sigma}_a(m_0^2)) \ . \tag{2.14}$$

With this subtraction, the real part of the inverse Y propagator vanishes at $E = m_0$ and it significantly reduces the correlations between couplings and bare masses [110]. Using the $D_1\bar{D}$ scattering amplitude and the $Y(4230)$ propagator G_Y, we can derive the operator for the production from a point-like source $\mathcal{M}_Y$, shown in Fig. 2.2, via $Y(4230)$ to $D_1\bar{D}$

$$\mathcal{M}_Y = (c - \alpha G_0 g_{Y0})(1 + 2\omega_Y \Sigma_{D_1 D} G_Y g_{Y0}^2) \ , \tag{2.15}$$

where c is the direct coupling of the photon to $D_1\bar{D}$ in the quantum numbers $J^{PC} = 1^{--}$, which vanishes in the HQSS limit, and α is the source term coupling of the photon to the bare Y state. Eq. (2.15) gives the impression as if it had a pole at the bare mass m_0, however, from Eq. (2.9) one gets that

$$(1 + 2\omega_Y \Sigma(E^2) G_Y(E) g_{Y0}^2) = G_0(E)^{-1} G_Y(E) \, , \tag{2.16}$$

which allows us to rewrite Eq. (2.15) as

$$\mathcal{M}_Y = (a + Eb) G_Y(E) g_{Y0} \ . \tag{2.17}$$

Here, in the purely one channel $D_1\bar{D}$ problem, unitarity requires the parameters to be real. Neglecting HQSS breaking effects, it is not possible to produce $D_1(2420)\bar{D}$

from a S-wave $\bar{c}c$ source, as the light degrees of freedom $j_\ell = \frac{3}{2} \otimes \frac{1}{2}$ can not couple to 0. At leading order, the production must go via the broad $D_1(2430)$, which has $j_\ell^P = \frac{1}{2}^+$. In the quark model, the physical $D_1(2420)$ and $D_1(2430)$ are generated by the admixture of a ${}^S L_J = {}^1P_1$ and a ${}^3P_1$ quark model state [111]. Ref. [96] argues that a small amount of HQSS breaking, allowing the mixture of $D_1(2420)$ and $D_1(2430)$, suffices for the production to be in the expected order of magnitude. In principle, we could allow for complex couplings in either the production or contact terms to absorb this effect, however, it was not necessary to achieve a proper fit.

The polarization of the $Y(4230)$ is determined by the Lepton-Photo production. The index structure of the Lepton-Tensor $L^{\mu\nu}$ must reproduce the transverse polarization of the photon produced in e^+e^- collision

$$L^{\mu\nu} = 4\left[k_1^\mu k_2^\nu + k_1^\nu k_2^\mu - g^{\mu\nu}((k_1 \cdot k_2) + m_e^2)\right] , \tag{2.18}$$

where k_1, k_2 denote the momentum of the electron and positron. At the energies studied in this work, the term proportional to the electron mass m_e is neglectable. We define the beam axis as the third component

$$\vec{k_1} = k_{\mathrm{CM}}(0,0,1)^{\mathrm{T}}, \quad \vec{k_2} = k_{\mathrm{CM}}(0,0,-1)^{\mathrm{T}} , \tag{2.19}$$

where $k_{\mathrm{CM}} = k$ is the center of mass momentum of the electron positron pair. The scalar product then evaluates in ultra-relativistic approximation as $k_1 \cdot k_2 = \omega_e^2 + k^2 \approx 2k^2$. The 4-momenta will be contracted by the polarization vectors of the heavy fields, leaving only the spacial components, such that:

$$L^{ij} = 8k^2\left[\delta^{ij} - \delta^{i3}\delta^{j3}\right] \tag{2.20}$$

where we used $k_1^i = k\delta^{i3}, k_2^i = -k\delta^{i3}$.

2.2.2. $Z_c(3900)$

BESIII first discovered the charged $Z_c^\pm(3900)$ states in the $J/\psi\pi^\pm$ invariant mass distribution of $e^+e^- \to J/\psi\pi^+\pi^-$, which was confirmed by Belle shortly after [112–114]. Later, its neutral partner was also discovered [115], confirming the $Z_c(3900)$ to be in iso triplet. As the decay $Z_c^\pm(3900) \to J/\psi\pi^\pm$ is observed, its minimal quark content must be $\bar{c}c$ to produce a J/ψ in the final state. Furthermore, as it also appears in charged modes, additional light valence degrees of freedom must be present and it was classified as an exotic state. In the literature the $Z_c(3900)$ is predominantly regarded to be a $D^*\bar{D}$ hadronic molecule [25, 80, 116]. Its quantum numbers were determined to be $I^G J^{PC} = 1^+1^{+-}$.

Analogous to the $Y(4230)$, we can express the wavefunction of the neutral $Z_c^0(3900)$ as a negative $C-$ eigenstate of $D^*\bar{D}$ under the assumption, that it is a $D^*\bar{D}$ molecule

$$|D^*\bar{D}(C=-1)\rangle = \frac{1}{\sqrt{2}}\left(|D^*\bar{D}\rangle + |D\bar{D}^*\rangle\right) . \tag{2.21}$$

As the charged $Z_c^{\pm}(3900)$ are not eigenstates of C, we can follow the construction of Ref. [117] in the bottemonium sector to write the wave function as

$$\begin{aligned}
|D^*D(I=1)\rangle_{I_3=1} &= \frac{1}{\sqrt{2}}\left(|D^+\bar{D}^{*\,0}\rangle - |D^{*+}\bar{D}^0\rangle\right) \\
|D^*D(I=1,C=-1)\rangle_{I_3=0} &= \frac{1}{2}\left(|D^{*0}\bar{D}^0\rangle - D^{*+}\bar{D}^-\rangle + |D^0\bar{D}^{*\,0}\rangle - |D^+D^{*+}\rangle\right) \\
|D^*D(I=1)\rangle_{I_3=-1} &= \frac{1}{\sqrt{2}}\left(|D^{*0}D^-\rangle - |D^{*-}\bar{D}^0\rangle\right) .
\end{aligned} \tag{2.22}$$

The relevant lagrangian for the coupling of Z_c to $D^*\bar{D}$ and the $D^*\bar{D}$ self-interaction is

$$\mathcal{L}_Z = g_{Z0}(\bar{D}^{*\dagger i}Z^iD^\dagger - \bar{D}^\dagger Z^iD^{*\dagger i}) + g_2\left[(D^{*i}\bar{D})^\dagger(D^{*i}\bar{D}) + (D\bar{D}^{*i})^\dagger(D\bar{D}^{*i})\right] + \text{hc.} . \tag{2.23}$$

The same reasoning for $g_1 = 0$ discussed in section 2.2.1 applies for g_2, i.e. $g_2 = 0$.

In analogy to the Y propagator provided in Eq. (2.11) we find for the propagator of the $Z_c(3900)$ from solving the related Dyson equation

$$G_Z = \frac{1}{2\omega_Z}\frac{1}{E - m_0 - \sum_i g_i\Sigma_i g_i} , \tag{2.24}$$

where the sum in the denominator runs over all relevant channels, which for the $Z_c(3900)$ are $D^*\bar{D}$ and $J/\psi\pi$ [51, 114], denoted as channels 1 and 2 respectively. Here g_i stands for the couplings of the $Z_c(3900)$ with the channel i, and Σ_i refers to the self-energy in the corresponding channel. As before the trivial spin structure of the propagator is not shown. As the energy range studied in this work is far above the $J/\psi\pi$ threshold, we only consider the leading effect to self-energy, $D^*\bar{D}$. Experiments confirmed that the coupling of the $Z_c(3900)$ to $D^*\bar{D}$ is significantly larger than to $J/\psi\pi$, leading to a ratio of partial widths of $\Gamma(D\bar{D}^*)/\Gamma(J/\psi\pi) = 6.2 \pm 1.1 \pm 2.7$ [114], altough $D^*\bar{D}$ has a tiny phase space.

Therefore the contribution of $J/\psi\pi$ to the self-energy is well approximated by a constant, which real part can be absorbed into the bare mass m_0, resulting in

$$G_Z = \frac{1}{2\omega_Z}\frac{1}{E - m_0 - g_{z0}^2\Sigma_{D^*D} - i\Gamma_Z/2} . \tag{2.25}$$

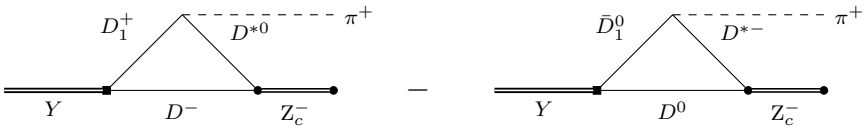

Figure 2.3.: Diagramatic contributions to $Y(4230) \to Z_c(3900)^-\pi^+$ relevant for the process $e^+e^- \to D^0D^{*-}\pi^+$.

We subtract the real part of the self-energy in accordance with Eq. (2.14). The parameter Γ_Z captures not only the effects of $J/\psi\pi$ but also the effects of all other inelastic thresholds. Although this approximation violates unitarity, it is well justified in certain situations as demonstrated later in this section.

The Z_c is at leading order produced via the triangle $Y \to Z_c\pi$. Considering the $D^0D^{*-}\pi^+$ final state, only two out of the four components of the $Y(4230)$ wavefunction, namely $|D_1^+D^-\rangle$ and $|D^0\bar{D}_1^0\rangle$, will contribute. The pertinent diagrams are shown in Fig. 2.3. A so-called triangle singularity further enhances this production [80, 118], as certain kinematics can lead to logarithmic singularities from the loop integration. Ref.[119] extensively discusses this phenomenon in the context of $\Lambda_b \to J/\psi K\pi$ decays. For the process relevant to this work we can write the on-shell momentum of the D for the first $D_1\bar{D}$ and second $D^*\bar{D}(\pi)$ cut by

$$\begin{aligned} p_{D,\text{cut1}} &= \frac{1}{2m_Y}\lambda^{1/2}(m_Y^2, m_{D_1}^2, m_D^2) \\ p_{D,\text{cut2}} &= \gamma(\beta E_D^* - p_D^*)\,, \end{aligned} \tag{2.26}$$

where E_D^* and p_D^* denote the D^* energy and momentum in the center of mass frame of $D\bar{D}^*$. The boost factors are given by $\beta = p_{DD^*}/E_{DD^*}$ and $\gamma = 1/\sqrt{1-\beta^2}$. As both these momenta must be equal, it follows for $p_D > 0$ that $p_{D^*} = \gamma(\beta E_{D^*}^* + p_D^*) > 0$ and therefore, both the D and D^* move in the same direction. In the rest frame of the $Y(4230)$ the velocities of the D and D^* are given by

$$v_D = \beta\frac{E_2^* - p_2^*/\beta}{E_2^* - \beta p_2^*} < \beta, \qquad v_{D^*} = \beta\frac{E_{D^*} * p_D^*/\beta}{E_{D^*}^* + \beta p_D^*} > \beta\,, \tag{2.27}$$

from which follows $v_{D^*} > v_D$. In a classical sense, the D_1 decays into $D^*\pi$, and subsequently the D^* can catch up with the beforehand produced D, making the second cut operative. The generalized idea was already formulated in 1965 in Ref.[120], from which the two necessary conditions for a triangle singularity follow:

2. The $Y(4230)$ as a $D_1\bar{D}$ molecule

1. All three intermediate particles can go on-shell simultaneously.

2. Particle 3 (D^*) produced in the decay of particle 1 (D_1) can catch up with particle 2 (D).

Although the contributions shown in Fig. 2.3 have a relative minus sign, the individual contributions generate an additional minus sign. From the lagrangian of Eq. (1.73) it follows that $T \to H\Phi$ and $H \to H\Phi$ vertices change sign under exchange of $Q \leftrightarrow \bar{Q}$. The two considered diagrams have the heavy quarks and anti-quarks interchanged. We do not need to consider the light degrees of freedom, as the vertices for π^+ or π^- share the same sign. Consequently, all three vertices change sign under the exchange $Q \leftrightarrow \bar{Q}$, such that the contributions of both diagrams add up.

In the following, we will discuss the effect of the constant width approximation on bound states and resonances. For the $Y(4230)$, we only consider the leading effect, namely $D_1\bar{D}$, to the self-energy. The resulting bound state pole lies on the physical sheet with respect to $D_1\bar{D}$. However, as the D_1 is unstable and decays into $D^*\pi$, there is an additional branch cut for the $D\bar{D}^*\pi$ intermediate state, such that the pole is located on the unphysical sheet with respect to $DD^*\pi$ as depicted in Fig. 1.5. For the present analysis, we only consider a limited energy range, such that the width of the D_1 can be treated as constant, as the D_1 pole is sufficiently high above the $D^*\pi$ threshold [36]. The propagator of the $Y(4230)$ therefore only produces a $D_1\bar{D}$ branch cut and the bound state pole is shifted deeper into the complex plane according to the constant width.

However, for proper resonances above a threshold, the effect of an additional constant contribution to the width appears more drastic, as demonstrated in Fig. 2.4. While the $Z_c(3900)$ is considered to be $D^*\bar{D}$ hadronic molecule, our fits suggest the pole to be slightly above the $D^*\bar{D}$ threshold. The implications of this observation are discussed later in section 2.6, for now, we focus only on the analytic structure of the resonance propagator. Considering the contributions of $D^*\bar{D}$ and $J/\psi\pi$ to the self-energy, the poles of the $Z_c(3900)$ appear as the blue dots in Fig. 2.4, consistent with unitarity. The lower and upper thresholds correspond to $J/\psi\pi$ and $D^*\bar{D}$, respectively. The physical sheet with respect to $J/\psi\pi$ is colored green, while the yellow sheet corresponds to the unphysical sheet to with respect to $D^*\bar{D}$ above its threshold, where the resonance poles are located. Approximating the contribution of $J/\psi\pi$ as a constant, the propagator only generates the higher $D^*\bar{D}$ branch cut, and the poles move according to Fig. 2.4. While this violates unitarity and Schwartz reflection principle, it also appears that the pole located on the positive imaginary half-plane on the unphysical sheet can move into the negative imaginary half-plane onto the physical sheet, denoted by the gray color in Fig. 2.4. For the 1-channel

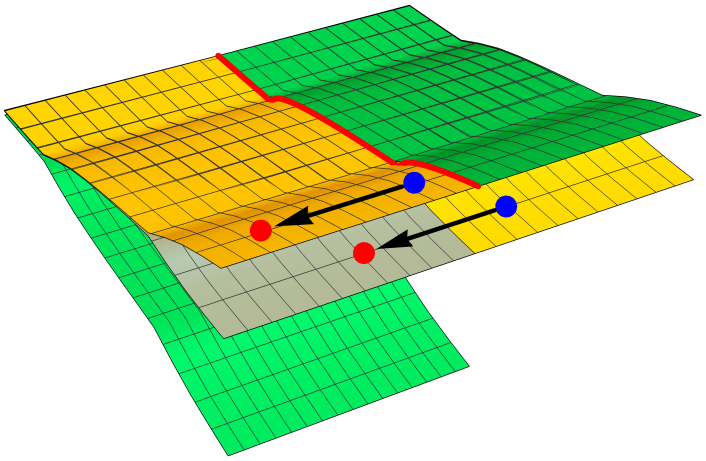

Figure 2.4.: Depiction of a 2 channel T-matrix showing the implication of the constant width approximation for a resonance. The blue dots denote the resonance poles on the unphysical sheet only considering the leading effects to the self-energy dynamically. The red dots denote the resonance pole after adding a constant width, showing the trajectory of the pole for increasing Γ_{add}.

system, it seems that analyticity is violated, however, with respect to the full two-channel problem, the pole moves on the unphysical $-+$ sheet. As the thresholds in this example are more than 600 MeV apart, the second pole on the $-+$ sheet has negligible influence on the real axis. Consequently, one only needs to consider the pole on the $+-$ sheet to be physical, which as expected moves further into the complex plane the higher the additional constant width is.

2.2.3. $\psi(4160)$

Very close to the nominal mass of the $Y(4230)$ a conventional charmonium resonance is located, the $\psi(4160)$. With a mass of $m_\psi = (4191 \pm 5)$ MeV and a width of $\Gamma_\psi = (70 \pm 10)$ MeV, at least some interplay between the two resonances is expected. While most of the hadronic final states do not show direct evidence for multiple resonances in the studied energy range, the $e^+e^- \to \mu^+\mu^-$ cross section data clearly shows two separate structures, which are impossible to describe with a single resonance. This is illustrated in Fig. 2.5, where we show the fit results with and without the $\psi(4160)$ for the $D^0D^{*-}\pi^+$, $J/\psi\pi^+\pi^-$ and $\mu^+\mu^-$ cross section. The narrow structure seen in the $J/\psi\pi\pi$ channel is by itself incompatible with the broad structure seen in $D\bar{D}^*\pi$, as well as some other channels discussed below. This is also reflected in

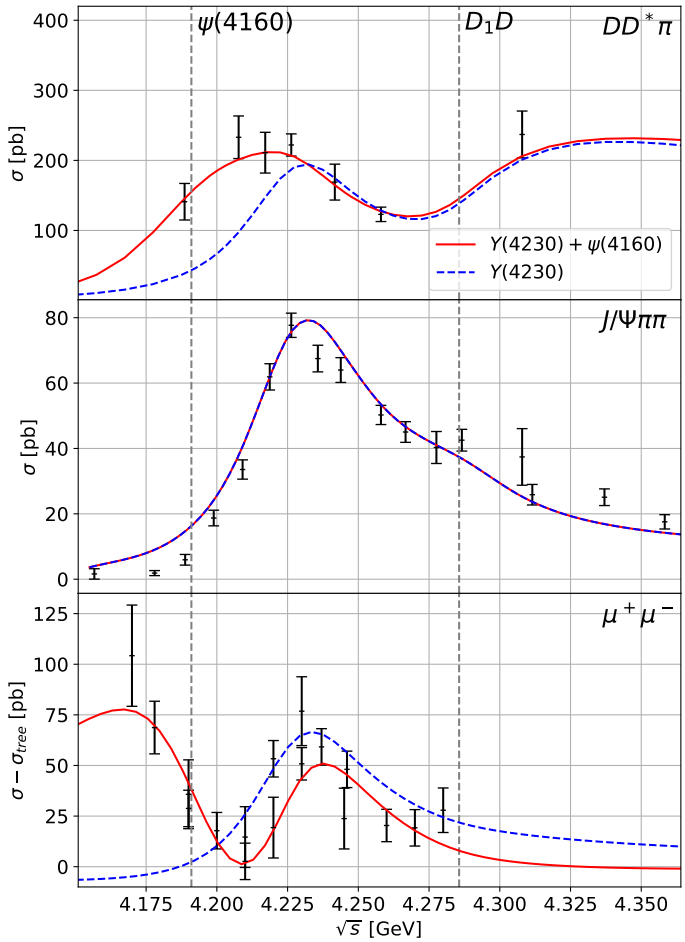

Figure 2.5.: Fit result for $D^0D^{*-}\pi^+$ and $J/\psi\pi^+\pi^-$ channels, including the $\psi(4160)$ (solid red line) and omitting it (dashed blue line). The data for the $D^0D^{*-}\pi^+$ channel are from Ref. [121] and those for the $J/\psi\pi^+\pi^-$ channel from Ref. [67]. The vertical red dotted lines indicate the positions of the nominal mass of the $\psi(4160)$ and $D_1\bar{D}$ threshold, respectively. The black dotted line at 4.33 GeV denotes the upper limit of the $D^0D^{*-}\pi^+$ fit range.

the resonance parameters extracted by BESIII. The width extracted from $D^0D^{*-}\pi^+$ is with $\Gamma_Y^{\text{exp}} = 77 \pm 6.8 \pm 6.3$ MeV [71] almost twice as large as in $J/\psi\pi^+\pi^-$ with $\Gamma_Y^{\text{exp}} 41.8 \pm 2.9 \pm 2.7$ MeV [67], differing by more than 3 standard deviations. Furthermore, $\mu^+\mu^-$ is the only channel where BESIII considered the inclusion of the $\psi(4160)$, while neglecting it in all of the hadronic final states. Ref. [122] puts forward the hypothesis that $\psi(4160)$ and $Y(4230)$ could actually be the same state. However,

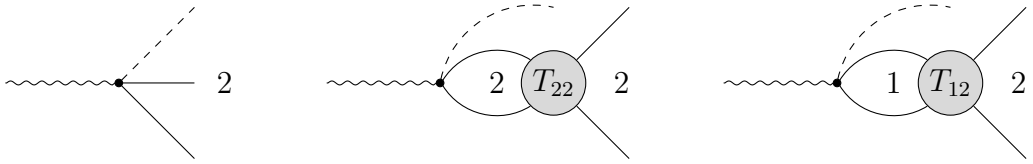

Figure 2.6.: Feynman diagram for production of channel 2. The scattering amplitudes T_{ij} in the channels ij $(i, j = 1, 2)$ are related to the Z_c propagator as $T_{ij} = g_i G_Z g_j$.

the data shown in Fig. 2.5 indicate that this conjecture is incompatible with the data.

For the exploratory study, we only consider the leading effects of the $\psi(4160)$ perturbatively via contact interactions to the final state, described in the following section. The resonance propagator is parameterized by a constant width Breit-Wigner, where we fix mass and decay width of the $\psi(4160)$ to its central values given in the Review of Particle Physics by the PDG [4]. As the coupling of the $\psi(4160)$ to the hadronic final states studied in this work is small, a Breit-Wigner is justified for an exploratory fit. In our subsequent study, the $\psi(4160)$ will be properly unitarized via some K-matrix formalism.

2.3. Production with coupled channel FSI

Unitarity links scattering and production processes in hadronic final state interactions. The derivation of the 3-point function of the $Y(4230)$ given above is already an example of this. In Eq. (2.15) both a contact term to the final state as well as a resonance collecting the interactions of the final state are present. A consequence of the conservation of unitarity is, that the tree-level production term gets canceled and the final amplitude given in Eq. (2.17) is proportional to the dressed resonance propagator.

Thus, we cannot consider tree-level or contact terms of a decay without including the non-perturbative final state interactions in the relevant subsystem, which are parameterized by the pertinent resonance propagators.
The production amplitude F_2 for channel 2, shown in Fig. 2.6, can be expressed as

$$\begin{aligned} F_2 &= M_2(1 + \Sigma_2 g_2 G_Z g_2) + M_1 \Sigma_1 g_1 G_Z g_2 \\ &= G_Z \left(M_2(E - m_0 - g_1^2 \Sigma_1) + M_1 \Sigma_1 g_1 g_2 \right) , \end{aligned} \tag{2.28}$$

where M_i denotes the production operator for channel i. The expression for F_1 is analogous and obtained by simply interchanging index 1 and 2 in Eq. (2.28). By defining $M_1 = g_1 \hat{M}_1$ and $M_2 = g_2 \hat{M}_2$ we can express the form factor $\vec{F}$ by

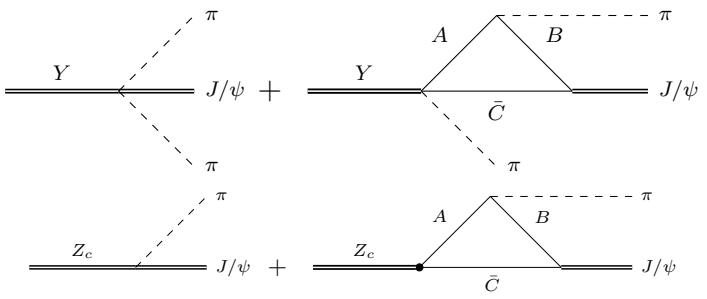

$$(\text{A,B,C}) = \{(D^*, D^*, D), (D^*, D, D), (D, D^*, D^*)\}$$

Figure 2.7.: Upper line: Feynman diagrams for production operator for $Y(4230) \to J/\psi\pi\pi$. In the full amplitude, the J/ψ and one of the pions undergo final state interactions driven by the Z_c. Lower line: The corresponding transition $Z_c \to J/\psi\pi$.

$$\vec{F}{=}G_Z\begin{pmatrix} g_1\left[(E-m_0)\hat{M}_1{+}g_2^2\Sigma_2(\hat{M}_1{-}\hat{M}_2)\right] \\ g_2\left[(E-m_0)\hat{M}_2{+}g_1^2\Sigma_1(\hat{M}_2{-}\hat{M}_1)\right] \end{pmatrix} . \tag{2.29}$$

which results in some vertex structure of the source term times the contribution of the Z_c propagator times the corresponding coupling of the channel, which is reflected in our choice of Feynman diagrams given in Sec. 2.5.2. The effective coupling g_2 of the Z_c to the $J/\psi\pi$ channel, shown in the lower line of Fig. 2.7, contains a triangle diagram and a counter term. M_2, shown in the upper line of Fig. 2.7, shows the same structure. Here the triangles appearing in g_2 and M_2 are almost identical, apart from the couplings of the Y and Z_c to D-mesons. The principal value part of these triangles depends on a regulator that requires to be renormalized by a contact term consistently for both cases because both include the $D^{(*)}\bar{D}^{(*)}J/\psi$ P-wave vertex. In the molecular scenario, the decay of the $Y(4230)$ is predominantly governed by an intermediate $D_1\bar{D}$ state rather than the ones depicted in Fig. 2.7, so it is reasonable to assume that the coefficient $\hat{M}_2$ to be real-valued.

Although the term proportional to $(\hat{M}_2 - \hat{M}_1)$ is formally included in the transition amplitude, it is not necessary for the description of the experimental data and the fit found it to be consistent with zero. Thus, we omit these terms and employ for the production amplitude

$$\vec{F} = G_Z \begin{pmatrix} g_1\alpha_1^{(1)}(\alpha_2^{(1)} + E) \\ g_2\alpha_1^{(2)}(\alpha_2^{(2)} + E) \end{pmatrix} , \tag{2.30}$$

where $\alpha_i^{(j)}$ are free parameters to be determined in the fit. These form factors are used in both the decays of $Y(4230)$ and the $\psi(4160)$. The strength parameters of the $\psi(4160)$ are denoted as $\beta_i^{(j)}$ in the following sections.

2.4. $\pi\pi - \bar{K}K$ final state Interaction

An amplitude $\mathcal{M}$ with certain isospin I (we omit the isospin index in what follows) can be projected to a partial wave $\mathcal{M}^l$ with definite angular momentum l

$$\mathcal{M}^l(s) = \frac{1}{2\sqrt{2}^\alpha} \int_{-1}^{1} \mathrm{d}z \; \mathcal{M}(s,z) P^l(z)\,, \tag{2.31}$$

where P^l denotes the Legendre polynomial of degree l, z the scattering angle and $\alpha = 0, 1, 2$ is a symmetry factor for identical particles in initial and final states (e.g. $\alpha = 2$ for $AA \to BB$, $\alpha = 1$ for $AA \to C\bar{C}$ and $\alpha = 0$ for $AB \to AB$). The full amplitude can be reconstructed using the orthogonality relation of the Legendre polynomials

$$\mathcal{M}(s,z) = \sqrt{2}^\alpha \sum_l (2l+1) \mathcal{M}^l(s) P^l(z)\,. \tag{2.32}$$

The rate of convergence for this series may vary depending on the process in question. We can compare the partial wave expansion for an exemplary box and triangle topology for $Y(4230) \to J/\psi\pi^+\pi^-$, later presented in section 2.5.2. As the Goldstone boson pair must have positive parity, only even partial waves will contribute. Both the box and triangle have an intermediate $D\bar{D}^*\pi$ cut, that can go on-shell in the $J/\psi\pi$ invariant mass distribution. For the triangle, however, also the $Z_c(3900)$ resonance is present and can go on-shell. This leads to a very slow convergence of the partial wave expansion. To show this we my write the Z_c amplitude as a resonance propagator

$$\frac{f(q)}{q^2 - m^2} = \frac{f(p,p')}{(p_0 - p_0')^2 - \vec{p}^2 - \vec{p}' - m^2 + 2pp'z}\,, \tag{2.33}$$

with p, p' denoting the incoming and outgoing momenta, respectively, and $f(p,p')$ denoting some non-resonant contributions. The accommodating scale introduced by the partial wave expansion for a given partial wave are the momenta $(pp')^L$, the centrifugal barrier factors. The only independent scale appearing in the denominator of Eq.(2.33) is given by $m_{\text{eff}} = (p_0 - p_0')^2 - m^2$, such that the corresponding expansion parameter is

$$\left(\frac{pp'}{m_{\text{eff}}^2}\right)^L\,. \tag{2.34}$$

Once the resonance can go on-shell the scale $m_{\text{eff}} = 0$ vanishes and the expansion breaks down. Consequently, infinitely many partial waves need to be considered, as

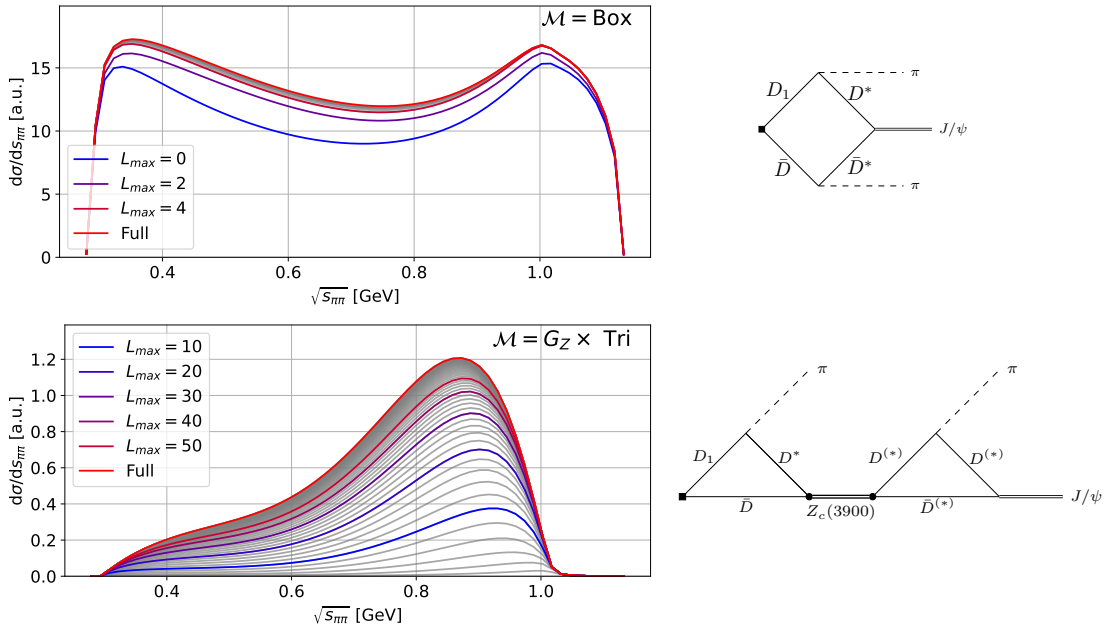

Figure 2.8.: Comparison of the convergence of the partial wave expansion for a box topology (upper panel) and a triangle including the $Z_c(3900)$ (lower panel) in the process $Y(4230) \to J/\psi\pi^+\pi^-$. The gray unlabeled lines denote partial waves summed up to $L_{\max} = 0, 2, 4, ..., 100$ given by Eq.(2.35).

all contributions will be of similar size. The resulting partial wave expansion for the box and triangle are shown in Fig. 2.8.
Here we compare the expansion of Eq.(2.32) truncated at different $L_{\max}$

$$\mathcal{M}^{L_{\max}}(s,z) = \sqrt{2}^{\alpha} \sum_{l}^{L_{\max}} (2l+1)\mathcal{M}^l(s)P^l(z)\,. \tag{2.35}$$

The majority of the box diagram is given by the S-wave contribution, with small corrections from the D- and F-wave. For $L_{\max} = 4$ the maximum deviation to the full amplitude is minor with roughly 4%. In contrast, the convergence for the triangle including the Z_c is considerably worse, where even at $L_{\max} = 50$ significant deviations to the full solution exist. As a result, the inclusion of the $\pi\pi - \bar{K}K$ S-wave final state interaction will have a significant influence on the lineshape of the box diagrams in the $\pi\pi$ and $J/\psi\pi$ invariant mass distributions, with only minor changes for the triangle diagrams.

The discontinuity of the production amplitude $\mathcal{M}^l$ is from the unitarity of the S-matrix given by

$$\text{disc}\mathcal{M}^l_j(s) = 2i \sum_k T^*_{jk}(s)\sigma_k(s)\mathcal{M}^l_k(s)\,, \tag{2.36}$$

where $\sigma_k = \sqrt{1-(4m_k^2/s)}\Theta(s-4m_k^2)$ and the subscript indices $j,k,...$ refer to the coupled channels $\pi\pi$ and $K\bar{K}$ in our case. Here T_{jk} denotes the meson-meson coupled-channel amplitude. The solution derived in section 1.6.2 is given by the Muskhelishvili Omnés function in Eq. (1.144). As a result, the full amplitude encoding the $\pi\pi/K\bar{K}$ final state interaction can be found by adding the amplitudes $\mathcal{M}_j$ and Γ, which only include the left- and right-hand (unitarity) cuts, respectively, and reads

$$\begin{aligned}\mathcal{M}_j^{\text{full}}(s) &= \mathcal{M}_j + \Gamma_j \\ &= \mathcal{M}_j + \sum_k \Omega_{jk}\left[(\mathcal{P}_{n-1})_k + \sum_{lm}\frac{s^n}{\pi}\int\frac{\mathrm{d}z}{z^n}\frac{\Omega_{kl}^{-1}(z)T_{lm}(z)\sigma_m(z)\mathcal{M}_m^0(z)}{z-s}\right] \\ &= \left[\mathcal{M}_j^{l>0}+\mathcal{M}_j^0\right] + \sum_k\left[\Omega_{jk}\left((\mathcal{P}_{n-1})_k + \frac{s^n}{\pi}\,\text{P.V.}\int[...]\right) + iT_{jk}\sigma_k\mathcal{M}_k^0\right],\end{aligned} \tag{2.37}$$

where $\mathcal{P}_{n-1}$ is a polynomial of the order $n-1$, which is discussed below, and Ω is the S-wave Omnés matrix.

The amplitudes $\mathcal{M}_j$ that have a left-hand cut correspond to the diagrams discussed in Secs. 2.5.2 and 2.5.3, while the right-hand cut in Γ is generated from the $\pi\pi/K\bar{K}$ S-wave FSI encoded inΩ.

The required inputs for the amplitude Omnés and T matrix are taken from Refs. [123, 124]. We now have a closer look at the principal value integral. Using the abbreviation $\sum_{kl}\Omega_{jk}^{-1}T_{kl}\sigma_l\mathcal{M}_l = f_j(z)$ we get

$$\begin{aligned}\text{P.V.}\int\frac{dz}{z^n}\frac{f_k(z)}{z-s} &= \text{P.V.}\int\mathrm{d}z\left[\frac{f_k(z)}{z^{n-1}}-\frac{f_k(s)}{s^{n-1}}+\frac{f_k(s)}{s^{n-1}}\right]\frac{1}{z(z-s)} \\ &= \int\mathrm{d}z\left[\frac{f_k(z)}{z^{n-1}}-\frac{f_k(s)}{s^{n-1}}\right]+\frac{f_k(s)}{s^{n-1}}\;\text{P.V.}\int\mathrm{d}z\frac{1}{z(z-s)}\;.\end{aligned} \tag{2.38}$$

Now we can analytically evaluate the integral of the second summand in the last line

$$\text{P.V.}\int_{s_{\text{th}}}^{\infty}\mathrm{d}z\frac{1}{z(z-s)} = \frac{1}{s}\log\left(\frac{1}{s/s_{\text{th}}-1}\right)\;. \tag{2.39}$$

However, in the exploratory study we aim at here, we neglect this part which we anticipate to play the role of a correction. The achieved quality of the fits might be taken as justification for this treatment a posteriori, even though changes in the relative weight of the individual contributions in a complete analysis cannot be ruled out.

2. The $Y(4230)$ as a $D_1\bar{D}$ molecule

Finally, the modified $\pi\pi$ and $\bar{K}K$ s-wave amplitude reads

$$(\mathcal{M}_j^0)_{\text{mod}} = \mathcal{M}_j^0 + \sum_k \Omega_{jk}\,(\mathcal{P}_{n-1})_k + \left(iT_{jk}\sigma_k + \frac{1}{\pi}\log\left(\frac{1}{s/s_{\text{th}}-1}\right)T_{jk}\sigma_k\right)\mathcal{M}_k^0\,, \tag{2.40}$$

such that we approximate the full amplitude (2.37) as

$$\mathcal{M}_{j\ \text{mod}} = \mathcal{M}_j^{l>0} + (\mathcal{M}_j^0)_{\text{mod}}\,. \tag{2.41}$$

Furthermore, this enables us to project the FSI onto the $K\bar{K}$-channel, allowing us to also determine the contribution of $Y(4230) \to J/\psi\pi\pi \to J/\psi\bar{K}K$.

The subtraction polynomial $(\mathcal{P}_{n-1})_j$ in Eqs. (2.37) and (2.40) is matched to the $Y(4230) \to J/\psi\Phi\Phi$ chiral contact term. In Ref. [125] it was found that both the light quarks SU(3) singlet and octet components both contribute for the $Y(4230)$, which can be decomposed as

$$|Y(4230)\rangle = \left(c_1|V_1^{\text{light}}\rangle + c_8|V_8^{\text{light}}\rangle\right)\otimes|V^{\text{heavy}}\rangle, \tag{2.42}$$

where

$$\begin{aligned} V_1^{\text{light}} &= \tfrac{1}{\sqrt{3}}(u\bar{u}+d\bar{d}+s\bar{s}) \\ V_8^{\text{light}} &= \tfrac{1}{\sqrt{6}}(u\bar{u}+d\bar{d}-2s\bar{s})\ . \end{aligned} \tag{2.43}$$

At leading order in chiral expansion the Lagrangian $\mathcal{L}_{Y\psi\Phi\Phi}$ is given by [126]

$$\begin{aligned} \mathcal{L}_{Y\psi\Phi\Phi} = & g_1\langle V_1^\alpha J_\alpha^\dagger\rangle\langle u_\mu u^\mu\rangle + h_1\langle V_1^\alpha J_\alpha^\dagger\rangle\langle u_\mu u_\nu\rangle v^\mu v^\nu \\ & + g_8\langle J_\alpha^\dagger\rangle\langle V_8^\alpha u_\mu u^\mu\rangle + h_8\langle J_\alpha^\dagger\rangle\langle V_8^\alpha u_\mu u_\nu\rangle v^\mu v^\nu \\ & + \text{h.c.}\,, \end{aligned} \tag{2.44}$$

with $J = (\psi/\sqrt{3})\mathbb{1}$. For the $J/\psi\pi\pi$ and $J/\psi K\bar{K}$ final states, the resulting s-wave projected chiral contact terms are given by

$$\begin{aligned} M_{\pi\pi}^0 &= -\frac{2}{f^2}\sqrt{m_Y m_{J/\psi}}\left(g_1 + \frac{g_8}{\sqrt{2}}\right)(s-2m_\pi^2) + \frac{h_1 + \frac{h_8}{\sqrt{2}}}{2}\left[s + q^2\left(1-\frac{\sigma_\pi}{3}\right)\right] \\ M_{KK}^0 &= -\frac{2}{f^2}\sqrt{m_Y m_{J/\psi}}\left(g_1 - \frac{g_8}{2\sqrt{2}}\right)(s-2m_K^2) + \frac{h_1 - \frac{h_8}{2\sqrt{2}}}{2}\left[s + q^2\left(1-\frac{\sigma_K}{3}\right)\right]\,, \end{aligned} \tag{2.45}$$

with $q^2 = \lambda^{1/2}(m_Y^2, m_{J/\psi}^2, s)/(2m_Y)$, resulting in

$$
\begin{aligned}
[\Omega\mathcal{P}_{n-1}]_{\pi\pi} &= \Omega_{11} M^0_{\pi\pi} + \frac{2}{\sqrt{3}}\Omega_{12} M^0_{KK} \\
[\Omega\mathcal{P}_{n-1}]_{KK} &= \Omega_{21} M^0_{\pi\pi} + \frac{2}{\sqrt{3}}\Omega_{22} M^0_{KK} \,.
\end{aligned}
\tag{2.46}
$$

In summary, the amplitudes used in our calculations, which incorporate the $\pi\pi/K\bar{K}$ FSI, are given by Eqs. (2.40), (2.41) and (2.46).

2.5. Final states

In this section we discuss the relevant final states studied in this work and present the derivation of the required scattering amplitudes.

2.5.1. $D^0 D^{*-}\pi^+$

As outlined in Sec. 1.4, the coupling of a molecular state to its constituents becomes maximal. Consequently, the most direct access is given by its near-threshold imprint on the cross section of the channel that forms the molecular state. The unnaturally large nucleon-nucleon scattering lengths originate from the same logic [25, 31, 33]. The phenomenon arises due to a close by molecule in the spin-1 channel, with the deuteron being a true bound state, and the spin-0 channel, with a nearby located virtual state.

The unstable $D_1(2420)$ with a width of approximately 30 MeV decays predominantly into $D^*\pi$ in D-wave. Thus, the closest connection to a possible molecular nature of the $Y(4230)$ is the $D\bar{D}^*\pi$ final state. The contributing diagrams are shown in Fig. 2.9. Both diagram (a) and diagram (c) have the intermediate $D_1\bar{D}$ state and scale with the large $Y \to D_1\bar{D}$ coupling. Moreover, both are enhanced by the near on-shell propagation of the D_1, as we are in the vicinity of a narrow state pole. The $Z_c(3900)$, appearing in the rescattering of the $D^*\bar{D}$ pair, is also treated as a hadronic molecule, in line with Ref. [80]. Accordingly, we expect the coupling of the Z_c to the $D^*\bar{D}$ channel to be large. The triangle loop part of diagram (c) is further enhanced by a very nearby triangle singularity [127], as discussed in Sec. 2.2.2. Thus diagrams (a) and (c) are expected to contribute significantly to the observables.

The binding energy of the $Y(4230)$ with about 60 MeV is roughly twice the width of the $D_1(2420)$, which still allows for a resonance signal at $\sqrt{s} = 4230$ MeV [36, 39]. However, it is strongly suppressed by the kinematics of the decay $D_1 \to D^*\pi$ in a D-wave, which develops its effect mostly as an enhancement above the $D_1\bar{D}$ threshold. In addition, although violating HQSS, the narrow $D_1(2420)$ is expected to mix with the much broader $j^P_\ell = \frac{1}{2}^+$ state, the $D_1(2430)$. This allows the narrow

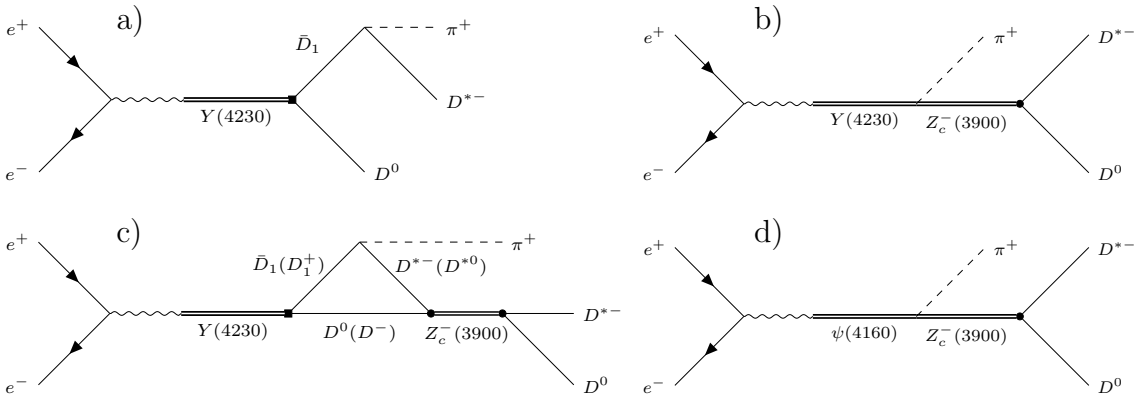

Figure 2.9.: Feynman diagrams contributing to $e^+e^- \to \bar{D}D^*\pi$. a) tree level, b) $Y(4230)$ contact term, c) Triangle, d) $\psi(4160)$ contact term, where the last two include the final state interactions in the doubly heavy subsystem.

$D_1(2420)$ to also decay in a S-wave [54], which does not suffer as strongly as the D-wave from the above-mentioned kinematic suppression. Therefore it can contribute significantly to the $Y(4230)$ peak in the $\pi D^*\bar{D}$ channel. The decays of $D_1(2420)$ to $D^*\pi$ in both S- and D-waves are included in all diagrams that contain this vertex, i.e. diagrams a) and c) in Fig. 2.9, as derived in Sec. 1.5. In this thesis, whenever we refer to D_1 without mass number, we consider the narrow $D_1(2420)$, to simplify notation.

Due to the large width of the $D_1(2430)$, it effectively acts like a short-range contribution. Thus, we do not explicitly calculate the corresponding loop contributions, but parameterize its effect by a S-wave point coupling of the $Y(4230)$ to $\pi D^*\bar{D}$ in all subsystems. Further, as the $D^*\bar{D}$ system undergoes final state interaction, this point coupling cannot occur isolated but needs to get dressed by the propagator of the $Z_c(3900)$, which parametrizes the $D^*\bar{D}$ S-wave interaction. The details are given in Sec. 1.5 and Sec. 2.3, which is represented by the diagram 2.9(b). The resulting amplitude is by construction consistent with the Watson final state theorem [128].

Finally, the structure around 4230 MeV in the experimental data of the $D^*\bar{D}\pi$ channel is notably broader than that observed, e.g., in the $J/\psi\pi\pi$ channel — see Fig. 2.5. As a result, the resonance parameters extracted by the BESIII collaboration are largely inconsistent for the different final states, as shown in Fig. 2.1. The possible mechanism considered in this work that allows for a simultaneous fit of the various channels is the inclusion of the $\psi(4160)$, which is parameterized by a small S-wave coupling to $D^*\bar{D}\pi$. The experimental signal observed below the $D_1\bar{D}$ threshold can therefore emerge due to the interference from the two resonances. Here we assume the coupling for the $\psi(4160)$ to be in a S-wave with respect to all subsystems. As before, the transition $\psi(4160) \to D^*\bar{D}\pi$ gets dressed by the

$Z_c(3900)$ propagator, which parameterizes the $D^*\bar{D}$ final state interaction. The corresponding diagram is given in Fig. 2.9(d). We are aware of the fact that, if the $\psi(4160)$ were (predominantly) a D-wave charmonium, there should be angular momentum present in the final state due to HQSS. However, for the present fit, the data do not require an additional coupling and thus we omit it from our study.

With $D^0D^{*-}\pi^+$ being the channel with the most direct access to the molecular nature of the $Y(4230)$, we expect the tree-level decay to provide the most significant contribution. As argued above the $D_1(2420)$ can decay into $D^*\pi$ in both S- and D-wave, such that the spin structure of the $Y \to D^0D^{*-}\pi^+$ amplitude can be written as

$$\begin{aligned}\mathcal{M}^i_{Y\to DD^*\pi} = G_\mathrm{Y}\Bigg\{ \left(\mathcal{M}^{DD^*\pi}_{Y\ \mathrm{CT}}\right)^{ij} - \frac{g_{Y0}}{\sqrt{2}}\left(h^\pi_{1d}\left(3p^i_\pi p^j_\pi - p^2_\pi\delta^{ij}\right) - h^\pi_{1s}\omega_\pi\delta^{ij}\right) \\ \times\left[G_{D_1}(E_{D^*\pi}) - 2g^2_{Z0}\mathcal{T}_{D_1DD^*}G_Z(E_{DD^*})\right]\Bigg\}\epsilon^{*\ j}_{D^*}\,,\end{aligned} \tag{2.47}$$

where we introduced the abbreviations

$$\begin{aligned}h^\pi_{1s} &= \frac{h'_s}{\sqrt{3}f_\pi}\sqrt{m_{D_1}m_{D^*}} \\ h^\pi_{1d} &= \sqrt{\frac{2}{3}}\frac{h'}{f_\pi}\sqrt{m_{D_1}m_{D^*}}\,.\end{aligned} \tag{2.48}$$

The $D_1{\to}D^*\pi$ couplings h'_s and h' in S- and D-wave are fixed from the experimentally measured D_1 decay as explained in Sec. 1.5. The S-wave vertex and other amplitudes below scale with the on-shell pion energy $\omega_\pi = \sqrt{m^2_\pi + p^2_\pi}$ to respect the Goldstone theorem, stating that the pion amplitude has to vanish in the chiral limit for $p_\pi \to 0$. For the spin indices i, j the summation over j is assumed implicitly. The tree-level diagram is given in Fig. 2.9a. Furthermore, the $D\bar{D}^*$ pair can re-scatter into the $Z_c(3900)$ via a triangle loop shown in diagram 2.9c. As explained above we further allow for a direct point-like transition of the $Y(4230){\to}D^0D^{*-}\pi^+$ in an S-wave, corresponding to the diagram in Fig. 2.9b. The phase of this diagram is fixed by the re-scattering of the $D\bar{D}^*$ pair into the $Z_c(3900)$, which is based on the formalism described in section 2.3

$$\left(\mathcal{M}^{DD^*\pi}_{Y\ \mathrm{CT}}\right)^{kj} = \ G_Z(E_{DD^*})g_{Z0}\omega_\pi\left[\alpha^{(1)}_1(\alpha^{(1)}_2{+}E_{DD^*})\delta^{kj}\right]\,.$$

This expression agrees to Eq. (2.30), where we replaced the general name g_1 to now adapt to a notation consistent with Sec.1.5.

The relative factor 2 between the Z_c contributions and the tree-level arises from the isospin coefficient of the $Y(4230)$ wave function shown in Eq. (2.5), which is discussed in Sec. 2.2.2. The coefficients of the iso-triplet production of the $Z_c(3900)$ from the wavefunction in Eq. (2.22) are absorbed into the coupling g_{Z0} of $Z_c(3900) \to D\bar{D}^*$.

Formally, one should treat the $Y(4230)$ arising from the $D\bar{D}^*\pi$ three-body system, where time-ordered perturbation theory (TOPT) [129] is the most convenient method for handling the 3-body cuts. With the more complete treatment in mind, which is presented in Sec. 3, we evaluate all loop integrals of this work using the same formalism. Thus, the scalar triangle with emitting a pion may be written as

$$\mathcal{T}_{D_1 DD^*} = \int \frac{\mathrm{d}^3 l}{(2\pi)^3} \frac{1}{8\omega_{D_1}\omega_D\omega_{D^*}} \frac{1}{E-\omega_{D_1}-\omega_D} \frac{1}{E-\omega_\pi-\omega_{D^*}-\omega_D} ,$$

where the D_1 energy is given by $\omega_{D_1} = \sqrt{(m_{D_1} - i\Gamma_{D_1}/2)^2 + l^2}$, with the constant width Γ_{D_1}. The energies of the other particles are defined analogously. See Sec. 2.2.1 for a discussion regarding the width of the D_1. In addition, we checked that the energy dependencies of the various loop diagrams included in this study agree with a covariant evaluation. As demonstrated above, simultaneous treatment of $Y \to J/\psi\pi\pi$ and $Y \to D\bar{D}^*\pi$ is only possible if we allow the interference with the $\psi(4160)$. The contribution of $\psi(4160) \to D^0 D^{*-}\pi^+$ is parameterized in line with Eq. (2.30), yielding

$$\mathcal{M}^i_{\psi\to DD^*\pi} = G_\psi g_{Z0} G_Z \omega_\pi \left[\beta_1^{(1)}(\beta_2^{(1)} + E_{DD^*})\delta^{ij}\right] \epsilon^{*\,j}_{D^*} . \tag{2.49}$$

Here, a comment is in order. As we examine the interference effect between $\psi(4160)$ and $Y(4230)$ on the line shapes in various channels—specifically, for $e^+e^- \to D^0 D^{*-}\pi$, $J/\psi\pi^+\pi^-$, $J/\psi K^+K^-$, $h_c\pi^+\pi^-$, $\chi_{c0}(1P)\omega$, $J/\psi\eta$, and $X(3872)\gamma$ we consider the same complex couplings $g_{\gamma R} = \exp(i\delta_{R\gamma}) e m_R^2/f_R$ for the production of resonance R from a photon as defined in Eq. (1.113), with R denoting both the $\psi(4160)$ and $Y(4230)$. For all channels listed above, it is obvious that only the relative phase of the two resonances plays a role, which in principle is not needed to achieve a proper description of the hadronic final states. However, this is not the case for the $e^+e^- \to \mu^+\mu^-$ cross section, where the phases of the two resonances enter individually. For the discussion regarding the necessity of these phase factors see Sec. 2.5.7 for details.

2.5.2. $J/\psi(\pi\pi/\bar{K}K)$

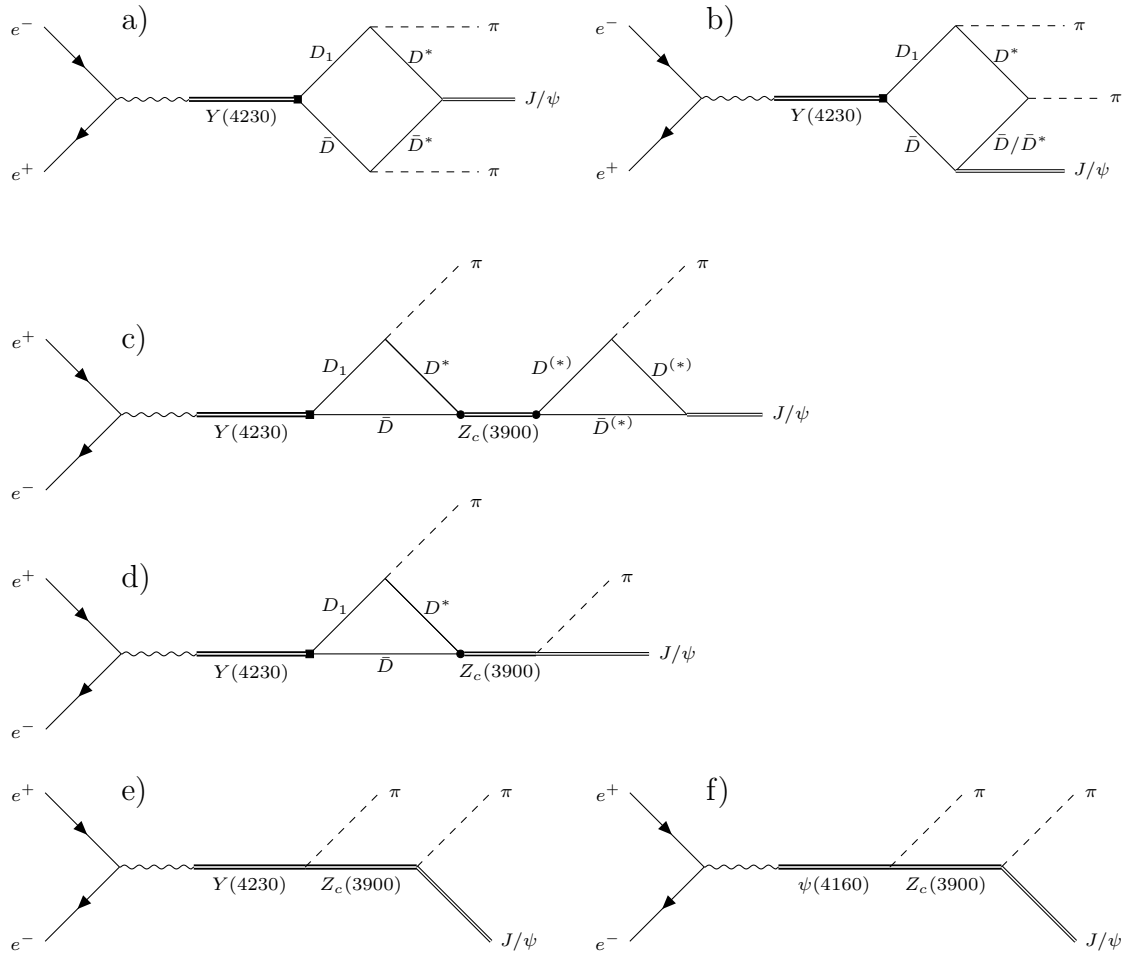

Figure 2.10.: Diagrams contributing to $e^+e^- \to J/\psi\pi\pi$. The thin lines in the box and triangle denote D^* or D mesons. a) and b) boxes, c) triangle, d) triangle counter term, e) $Y(4230)$ contact term, f) $\psi(4160)$ contact term, where for the last two the final state interactions in the doubly heavy subsystem are included.

Next we turn to the discovery channel of the $Y(4230)$, $e^+e^- \to J/\psi\pi\pi$, where the highly asymmetric lineshape lead to the claim for the existence of an additional state called $Y(4320)$ [66, 67]. Again, driven by the assumed molecular nature of the $Y(4230)$, contributions that run through the $D_1(2420)\bar{D}$ intermediate state are sizable and need to be considered. Then, to reach the $J/\psi\pi\pi$ final state, possible topologies are either box diagrams (see Fig. 2.10, (a) and (b) as well as Fig. 2.11

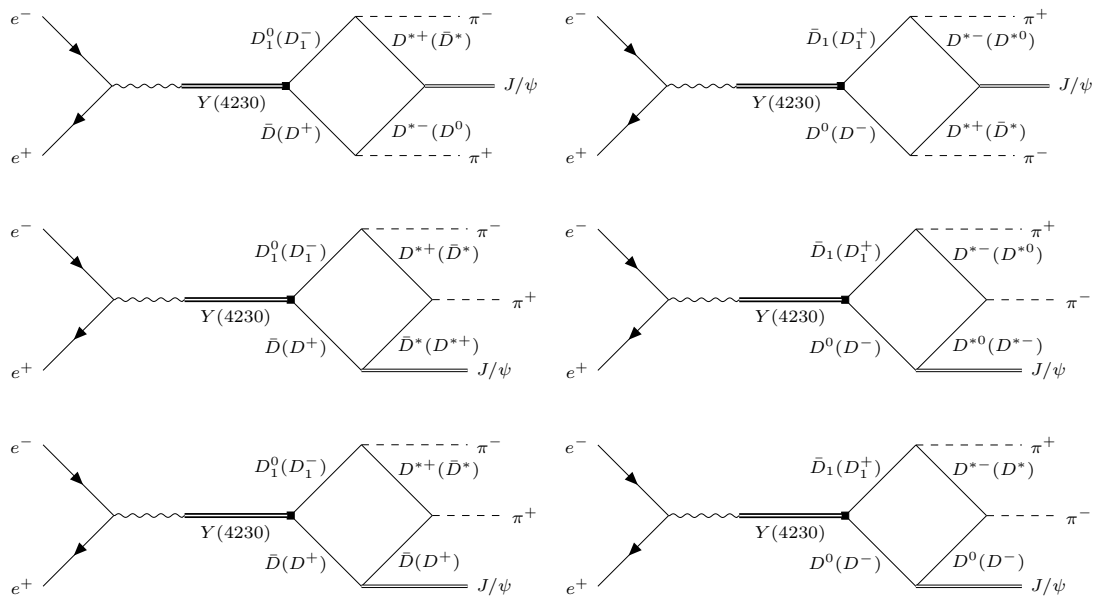

Figure 2.11.: Decomposition for the box topology of $e^+e^- \to J/\psi\pi^+\pi^-$

for a complete set of box diagrams) or a triangle followed by a $Z_c(3900)$ propagator (Fig. 2.10(c) and (d)). As before we need to allow for additional processes and also here include a diagram for the contact transition of the $Y(4230)$ to the $J/\psi\pi\pi$ final state (Fig. 2.10(e)), as before dressed by the final state interaction that leads to the occurrence of the $Z_c(3900)$ — see Sec. 2.3 for a detailed discussion. Furthermore, we also allow for a contribution of the $\psi(4160)$ in this channel, shown in Fig. 2.10(f).

The signal of the $Z_c(3900)$ appears twice in the $J/\psi\pi$ invariant mass distribution, as demonstrated in Fig. 2.12. As the Z_c can form in both the $J/\psi\pi^+$ and $J/\psi\pi^-$ subsystem, a so-called reflection can be seen. The imprint of the reflection does not generate a sharp pole-like structure but leaves a small contribution at low invariant masses, where the Z_c can go on-shell in the other subsystem.

To come to the full amplitudes, the $\pi\pi$ final state interaction needs to be taken into account as well. Since the initial photon generates a $\bar{c}c$-pair, which is isoscalar, and the final $\bar{c}c$ pair is isoscalar as well, the pion pair must be isoscalar with even angular momentum (the latter also follows from parity conservation). In the vicinity of the $Y(4230)$ pole, the $\pi\pi$ system is probed in the energy range from its threshold up to about 1.1 GeV. Since the scalar-isoscalar $\pi\pi$ interaction has a strong coupling to the $\bar{K}K$ system, the final state interaction is included by employing a formalism that explicitly treats the coupled channels. Since the full treatment of the system is technically very demanding [101] (see Refs. [97–99] for related studies) because of the intricate singularity structure of the pertinent integrals, in this exploratory study

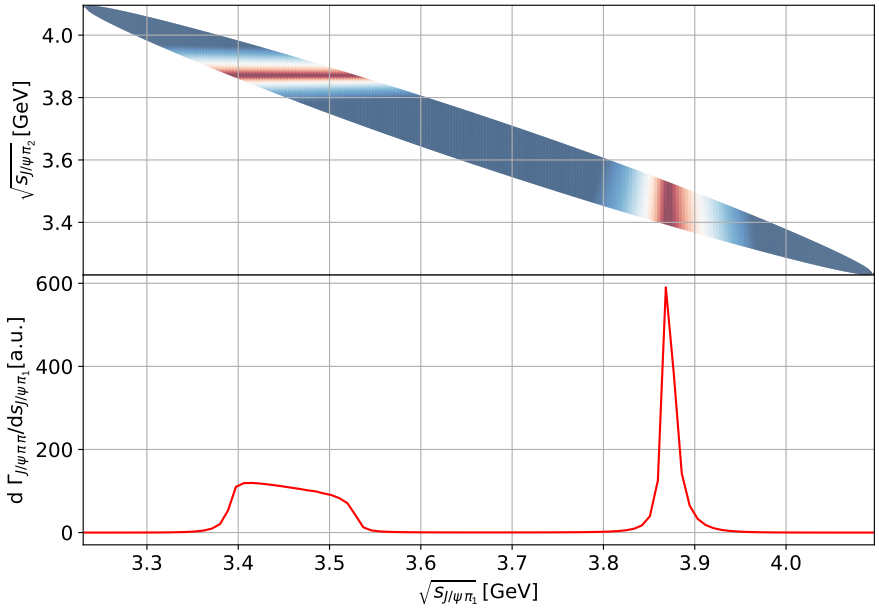

Figure 2.12.: Reflection of the $Z_c(3900)$ in the $J/\psi\pi$ invariant mass distribution of the decay $Y(4230) \to J/\psi\pi\pi$. The upper plot shows the modulus of the $Z_c(3900)$ propagator in a Dalitz plot for the $J/\psi\pi_1$ - $J/\psi\pi_2$ system. The lower panel shows the resulting invariant mass distribution for one of the $J/\psi\pi$ subsystems.

we employ an approximate treatment that still allows for a sensible description also of the $\pi\pi$ spectra — details are given in the following and in Sec. 2.4.

The coupled channel treatment of the $\pi\pi/\bar{K}K$ final state interaction provides us at the same time access to $J/\psi\bar{K}K$ final state. To make the latter calculation complete, we also need to take into account strangeness in the source, as shown in Fig. 2.13. This does not introduce any additional parameters, since we demand that the vertices are consistent with the $SU(3)$-flavor symmetry. Naturally, the strangeness sources are also included in the calculation of the $J/\psi\pi\pi$ final state.

The dominant contributions corresponding to the molecular nature of the $Y(4230)$ are the box, below denoted as $\mathcal{M}^{\square}$, and triangle, $\mathcal{M}^{\triangle}$, topologies, since those contain the $D_1\bar{D}$ intermediate state. As the second triangle in figure 2.10 c) is divergent, due to the internal P-wave vertex that is connected to a J/ψ coupling to a pair of $D^{(*)}$ mesons, a counter term $\mathcal{M}^{\triangle}_{\mathrm{CT}}$ is also introduced

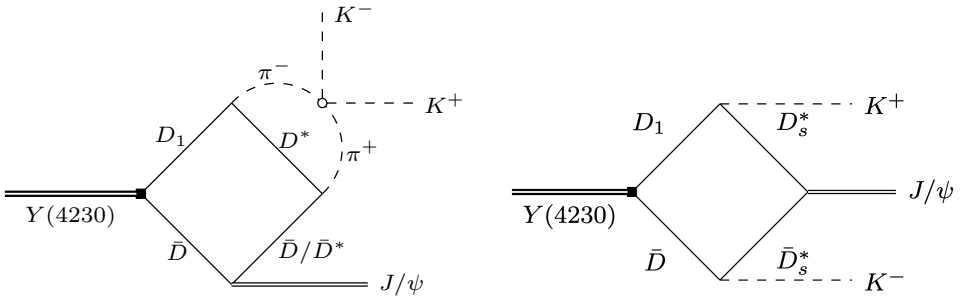

Figure 2.13.: Final state interaction $Y(4230) \to J/\psi\pi^+\pi^- \to J/\psi K^+K^-$ and strange source for $Y(4230) \to J/\psi K^+K^-$

$$\begin{aligned}
\mathcal{M}^i_{Y\to J/\psi\pi\pi} =& G_Y \left[\left(\mathcal{M}_{Y\ \mathrm{CT}}^{J/\psi\pi\pi} \right)^{il} - \frac{g_{Y0}}{\sqrt{2}} \left(h^\pi_{1d}(3p^i_{\pi 1}p^j_{\pi 1} - \delta^{ij}p^2_{\pi 1}) - h^\pi_{1s}\omega_{\pi 1}\delta^{ij} \right) \right. \\
& \left. \times\, 2 \left((\mathcal{M}^{\square})^{jl} + (\mathcal{M}^{\triangle})^{jl} + (\mathcal{M}^{\triangle}_{\mathrm{CT}})^{jl} \right) \right] \epsilon^{*\ l}_{J/\psi} \\
& + (p_{\pi_1} \leftrightarrow p_{\pi_2}) \\
\mathcal{M}^i_{\psi\to J/\psi\pi\pi} =& G_\psi \left[\beta_1^{(2)} (\beta_2^{(2)} + E_{J/\psi\pi_1}) \right] g^{Z\ il}_{J/\psi\pi} \omega_{\pi_1} G_Z(E_{J/\psi\pi_1}) \epsilon^{*\ l}_{J/\psi} + (p_{\pi_1} \leftrightarrow p_{\pi_2}) \ ,
\end{aligned} \tag{2.50}$$

where $g^{Z_c}_{J/\psi\pi}$ is the coupling of $Z_c \to J/\psi\pi$, given by the triangle transition shown in figure 2.7

$$g^{Z_c\ ik}_{J/\psi\pi} = g_{Z0}(\mathcal{M}_2^{\triangle})^{ik} + \omega_{\pi_2} c^{\triangle}_{\mathrm{CT}} \delta^{ik} \, . \tag{2.51}$$

To reduce the run-time of the numerical evaluation of the loop integrals only two out of four contributions of the $Y(4230)$ wave function shown in Eq. (2.5) with $p_{\pi_1} \leftrightarrow p_{\pi_2}$ are considered, as the differences due to isospin breaking are negligible small. Fig. 2.14 shows the individual contributions of the $Y(4230)$ wave function to one of the possible box topologies. The two diagrams in each row have the heavy quarks and anti-quarks interchanged. The $H \to H\Phi, T \to H\Phi$ vertices as well as the $Y \to D_1\bar{D}$ and $H\bar{H} \to J/\psi$ vertices change sign under the exchange of $Q \leftrightarrow \bar{Q}$, such that all contributions add up. As the isospin breaking effects in the loops are negligible, the diagrams in the same column are approximately equal. For example, for the box topologies shown in figure 2.11 only the particle content spelled out first at each line in the boxes is evaluated explicitly, while those in brackets are included via multiplication with a factor 2.

The $Y(4230)$ contact term $\mathcal{M}_{Y\ \mathrm{CT}}^{J/\psi\pi\pi}$ has two contributions, one in the $\pi\pi$ invariant mass from the subtraction polynomial of the $\pi\pi$ final state interaction and the other in $J/\psi\pi$ from the chiral contact term and intermediate $Z_c(3900)$

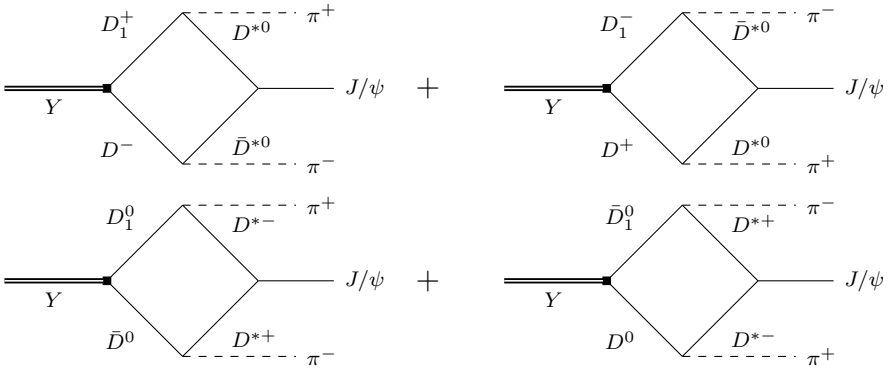

Figure 2.14.: Contributions of the $Y(4230)$ wavefunction to the decay $J/\psi\pi^+\pi^-$ for one possible box topology.

$$\left(\mathcal{M}_{Y\ \mathrm{CT}}^{J/\psi\pi\pi}\right)^{ik} = G_Z g_{J/\psi\pi}^{Z\,ik}\omega_{\pi_1}\left[\alpha_1^{(2)}(\alpha_2^{(2)} + E_{J/\psi\pi})\right] + \Omega_{11}M_0^{\pi\pi} + \frac{2}{\sqrt{3}}\Omega_{12}M_0^{KK}\,, \tag{2.52}$$

with $c_{\mathrm{CT}}^{\triangle}$ denoting the free parameter of the triangle counterterm. The amplitudes of the loop diagrams are given below, where the notation and numerical implementation are discussed in the appendix B

$$\begin{aligned}
(\mathcal{M}^{\square})^{jl} &= \mathcal{B}^{\mathrm{I}}(g_1^{\pi} g_{J/\psi D^* D^*}, q_{\mathrm{I}}^l p_{\pi_2}^j - p_{\pi_2}^l q_{\mathrm{I}}^j - \delta^{lj}(p_{\pi_2}\cdot q_{\mathrm{I}})) \\
&\quad + \mathcal{B}^{\mathrm{II}}(g_2^{\pi} g_{J/\psi DD^*}, p_{\pi_2}^l q_{\mathrm{II}}^j - \delta^{jl}(p_{\pi_2}\cdot q_{\mathrm{II}})) \\
&\quad + \mathcal{B}^{\mathrm{III}}(g_1^{\pi} g_{J/\psi DD}, p_{\pi_2}^j q_{\mathrm{III}}^l) \\
(\mathcal{M}^{\triangle})^{jl} &= \mathcal{T}_{D_1 DD^*} g_{Z0}^2 G_Z(E_{J/\psi\pi})(\mathcal{M}_2^{\triangle})^{jl} \\
(\mathcal{M}_2^{\triangle})^{jl} &= \mathcal{T}_2^1(g_2^{\pi} g_{J/\psi DD^*}, p_{\pi_2}^l q_{\mathrm{I}}'^{\,j} - \delta^{lj}(p_{\pi_2}\cdot q_{\mathrm{I}}')) + \mathcal{T}_2^2(g_1^{\pi} g_{J/\psi DD}, p_{\pi_2}^j q_{\mathrm{II}}'^{\,l}) \\
&\quad + \mathcal{T}_2^3(g_2^{\pi} g_{J/\psi D^* D^*}, q_{\mathrm{III}}'^{\,l} p_{\pi_2}^j - p_{\pi_2}^l q_{\mathrm{III}}'^{\,j} - \delta^{lj}(q_{\mathrm{III}}'\cdot p_{\pi_2})) \\
(\mathcal{M}_{\mathrm{CT}}^{\triangle})^{jl} &= \mathcal{T}_{D_1 DD^*} g_{Z0} G_Z(s_{J/\psi\pi}) c_{\mathrm{CT}}^{\triangle}\delta^{jl}\omega_{\pi_2}\,,
\end{aligned} \tag{2.53}$$

where the $q_{\mathrm{I}}, q_{\mathrm{II}}, q_{\mathrm{III}}, q_{\mathrm{I}}', q_{\mathrm{II}}', q_{\mathrm{III}}'$ denote the relative momenta at the $J/\psi D^{(*)} D^{(*)}$ vertex for the different box and triangle topologies. Additional free parameters come from the production polynomials of the $Y(4230)$ and $\Psi(4160)$ contact terms, namely $\alpha_1^{(2)}, \alpha_2^{(2)}$ and $\beta_1^{(2)}, \beta_2^{(2)}$ respectively, as well as the triangle counterterm $c_{\mathrm{CT}}^{\triangle}$. The inclusion of the $\pi\pi - \bar{K}K$ final state interaction is discussed in section 2.4.

With $J/\psi\pi\pi$ included in the study, we can also easily access $J/\psi K\bar{K}$, as the main contribution is expected to go via the $\pi\pi \to K\bar{K}$ final state interaction in the S-wave, where no new parameters need to be introduced. As mentioned above, the effect of the triangle topologies are negligible, as the partial wave projection on the $\pi\pi$ system contains a tiny S-wave piece due to the presence of the near on-shell $Z_c(3900)$ in the $J/\psi\pi$ subsystem. The amplitude is given by

$$\begin{aligned}\mathcal{M}^i_{Y\to J/\psi KK} =& G_Y \left(\left(\mathcal{M}^{J/\psi KK}_{Y\ \mathrm{CT}}\right)^{il} - \left(h^\pi_{1d}(3p_1^i p_1^j - \delta^{ij}p_1^2) + h^\pi_{1s}\omega_{\pi_1}\delta^{ij}\right) \right. \\ & \left. \times \left[\mathcal{M}^{jl}_{Y\to J/\psi KK} + \left[\left(\mathcal{M}^{\mathrm{loop}}_{J/\psi\pi\pi}\right)^{jl} \right]^{\mathrm{FSI}}_{\pi\pi\to KK} \right] \right) \epsilon^l_{J/\psi}\,,\end{aligned} \tag{2.54}$$

where we collected the loop diagrams in the amplitude

$$\left(\mathcal{M}^{\mathrm{loop}}_{J/\psi\pi\pi}\right)^{jl} = (\mathcal{M}^{\square})^{jl} + (\mathcal{M}^{\triangle})^{jl} \tag{2.55}$$

and

$$\left(\mathcal{M}^{J/\psi KK}_{Y\ \mathrm{CT}}\right)^{kl} = \left(\Omega_{21}M_0^{\pi\pi} + \frac{2}{\sqrt{3}}\Omega_{22}M_0^{KK}\right)\delta^{kl}\,. \tag{2.56}$$

Furthermore, $\mathcal{M}^{jl}_{Y\to J/\psi KK}$ is a strange source shown in Fig. 2.13. We postpone the inclusion of strange triangles, including the $Z_{cs}(4000)$, to a later, more complete analysis. In this sense, we regard this channel in this analysis as a consistency check. On the other hand, the $Z_{cs}(4000)$ can only appear in conjunction with an additional kaon within the triangular mechanism. Consequently, this state is expected to contribute significantly only in the energy range around 4470 MeV, well exceeding the energy range of interest in this study, even when accounting for the Z_{cs} width.

2.5.3. $h_c\pi^+\pi^-$

The diagrams contributing here are in principle analogous to those for the $J/\psi\pi\pi$ channel, shown in Fig. 2.10. However, in contrast to that channel, we exclude diagrams containing a $Z_c(3900)$. This is based on the observation that $Z_c(3900)$ does not show a significant contribution to the $h_c\pi$ invariant mass distribution. Additionally, we point out that the $Z_c(4020)$ is not included in this section, since this would require a complete treatment of the $\{D_1\bar{D}^{(*)}, D_2\bar{D}^{(*)}\}$ coupled channels, and of the $\{D\bar{D}^*, D^*\bar{D}^*\}$ sub-systems, which is postponed to future work presented in Sec. 3. Moreover, the contact terms that drive the contributions shown in diagrams (e) and (f) of Fig. 2.10 in the $J/\psi\pi\pi$ channel are omitted here since they violate spin symmetry. This symmetry violation is overcome by the loop diagrams as a result of

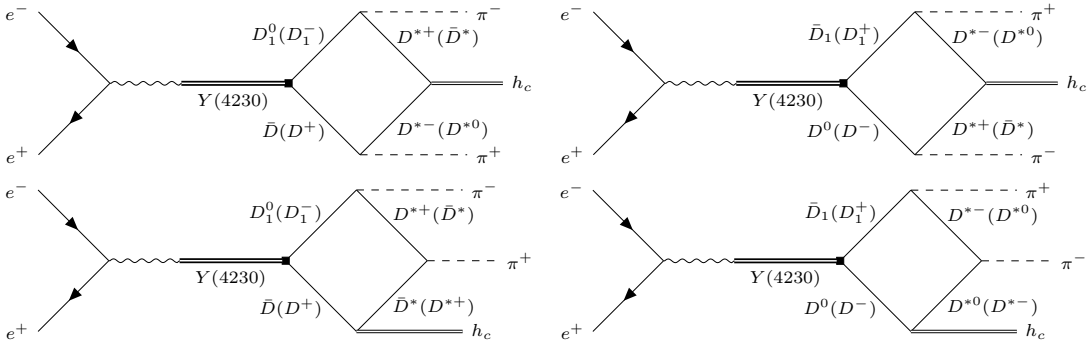

Figure 2.15.: Diagrams contributing to $e^+e^- \to h_c\pi^+\pi^-$.

the spin symmetry violation that enters through the mass differences of D and D^* as well as D_1 and D_2 — the former one being included explicitly in the calculation, the latter one by choosing an energy range where the D_2 contribution should be negligible. For a detailed discussion on how the spin symmetry gets restored in the heavy quark limit even in the presence of hadronic molecules, see Ref. [130]. In summary, for the $h_c\pi\pi$ channel we only include the box topologies shown in Fig. 2.15, expecting some deviations from experiment as a result of the omission of the $Z_c(4020)$. On the other hand, it is not expected that the $Z_c(4020)$ will generate significant structures in the total cross section of $h_c\pi\pi$, which is the focus of the current work, since in this case, the narrow peak from $Z_c(4020)$ in the πh_c subsystem is smeared. The same effect is demonstrated explicitly in this work, where the narrow structures of the $Z_c(3900)$ seen in the $J/\psi\pi$ subsystem do not modify visibly the energy dependence of the total cross section for $J/\psi\pi\pi$.
The amplitude therefore reads

$$\mathcal{M}^i_{Y\to h_c\pi\pi} = \frac{G_Y g_{y0}}{\sqrt{2}} \left[h^\pi_{1s}\omega_{\pi_1}\delta^{ij} - h^\pi_{1d}(3p^i_{\pi 1}p^j_{\pi 1} - \delta^{ij}p^2_{\pi 1})\right] \mathcal{M}^{h_c\pi\pi}_{\Box} m_{h_c}\epsilon_{ljm}p^m_{\pi_2}\epsilon^j_{h_c}\,, \qquad (2.57)$$

with $\mathcal{M}^{h_c\pi\pi}_{\Box}$ given by

$$\mathcal{M}^{h_c\pi\pi}_{\Box} = \frac{4gm^{3/2}_{D^*}\sqrt{m_D m_{h_c} m_{\chi_{c0}}}}{\sqrt{3}f_\pi f_{\chi_{c0}}} \left(\mathcal{B}^{h_c\pi\pi}_{\mathrm{I}} + \mathcal{B}^{h_c\pi\pi}_{\mathrm{II}}\right)\,. \qquad (2.58)$$

2.5.4. $\chi_{c0}\omega$

The Feynman diagrams are shown in figure 2.16. The main contribution is expected from the triangle, which scales like the scalar triangle as both the $D_1 \to D\omega$ and $DD \to \chi_{c0}$ are S-wave at leading order. Additionally, there are two S-wave contact

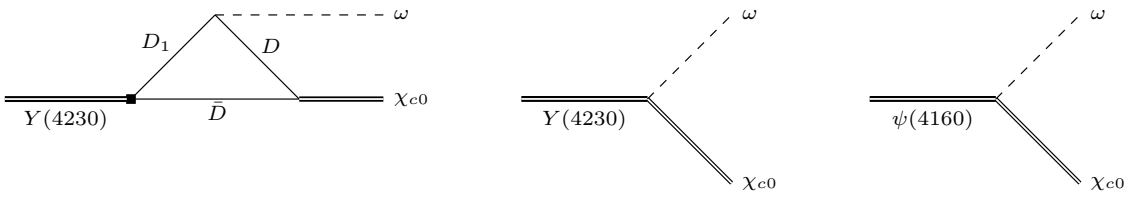

Figure 2.16.: Diagrams contributing to $\chi_{c0}\omega$.

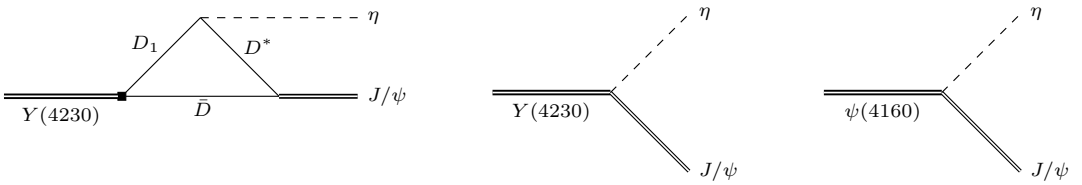

Figure 2.17.: Diagrams contributing to $J/\psi\eta$.

terms for the $Y(4230)$ and $\psi(4160)$ respectively

$$\begin{aligned}\mathcal{M}^i_{Y\to\chi_{c0}\omega}&=G_Y\left(c^{\triangle}_{\chi_{c0}\omega}m_{J/\psi}m_D\mathcal{T}_{\chi_{c0}\omega}+c^{Y}_{\chi_{c0}\omega}\right)\epsilon^i_\omega\\ \mathcal{M}^i_{\psi\to\chi_{c0}\omega}&=G_\psi c^{\psi}_{\chi_{c0}\omega}\epsilon^i_\omega\,,\end{aligned} \tag{2.59}$$

where $c^{\triangle}_{\chi_{c0}\omega}, c^{Y}_{\chi_{c0}\omega}$ and $c^{\psi}_{\chi_{c0}\omega}$ are free parameters. The width of the ω is included by convolving the cross section for a fixed ω mass with the ω spectral function — see, e.g., Ref. [131].

2.5.5. $J/\psi\eta$

For $J/\psi\eta$, the couplings of the triangle shown in figure 2.17 are fixed. The vector-vector-axial vector vertex of the contact terms must couple via $\epsilon^{\mu\nu\rho\sigma}$ which reduces to a three dimensional ϵ^{mjl} in the rest frame of the incoming particles:

$$\begin{aligned}\mathcal{M}^i_{Y\to J/\psi\eta}=&G_Y\left(-\frac{1}{\sqrt{6}}\left[h^\pi_{1d}(3p^i_\eta p^j_\eta-\delta^{ij}p^2_\eta)-h^\pi_{1s}\omega_\eta\delta^{ij}\right]\mathcal{T}_{J/\psi\eta}\left(g^{DD^*}_{J/\psi},q_l\right)\right.\\ &\left.+c^{Y}_{J/\psi\eta}p^l_\eta\right)\epsilon^{mjl}\epsilon^m_{J/\psi}\\ \mathcal{M}^i_{\psi\to J/\psi\eta}=&G_\psi c^{\psi}_{J/\psi\eta}\epsilon^{ijl}p^j_\eta\epsilon^l_{J/\psi}\,,\end{aligned} \tag{2.60}$$

where q denotes the relative momentum at the J/ψ vertex and $c^{Y}_{J/\psi\eta}$ and $c^{\psi}_{J/\psi\eta}$ are free parameters. We do not consider the mixing of the singlet η_1 and octet η_8 to the physical η and η' states, but just match $\eta_8=\eta$, as the mixing effects are small.

2.5.6. $X(3872)\gamma$

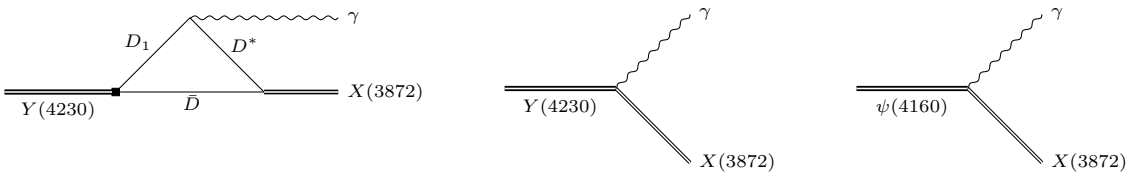

Figure 2.18.: Diagrams contributing to $X(3872)\gamma$.

If $Y(4230)$ is a $D_1\bar{D}$ hadronic molecule and both $Z_c(3900)$ and $X(3872)$ are $D^*\bar{D}$ hadronic molecules with $I(J^{PC}) = 1(1^{+-})$ and $I(J^{PC}) = 0(1^{++})$, respectively, the production mechanism of the latter pair in $Y(4230)$ decays must be analogous [132]. Only that the particle radiated off in the course of the $Y(4230)$ decay must have positive C parity for the transition to the Z_c and negative C parity for the transition to the $X(3872)$. Thus, all that needs to be done to get from the diagram that generates the Z_c in $Y(4230) \to \pi Z_c$ to the one that generates the $X(3872)$, is to replace the pion in the final state by a photon. The resulting diagrams are shown in Fig. 2.18 and are analogous to $Y(4230) \to Z_c\pi$ as well as $J/\psi\eta$. However, the quality of data for $X(3872)\gamma$ does not allow one to distinguish between the triangle and contact transition of $Y(4230) \to X(3872)\gamma$, such that we omit the latter from the start[1]. The vector-vector-axial-vector coupling of $D_1 \to D^*\gamma$ scales with ϵ^{kjl}, such that the amplitude is given by

$$\begin{aligned} \mathcal{M}^i_{Y\to X\gamma} &= G_Y c^Y_{X\gamma} \mathcal{T}_{X\gamma} \epsilon^{ijl} \epsilon^j_\gamma \epsilon^l_X \\ \mathcal{M}^i_{\psi\to X\gamma} &= G_\psi c^\psi_{X\gamma} \epsilon^{ijl} \epsilon^j_\gamma \epsilon^l_X \,, \end{aligned} \tag{2.61}$$

with $c^Y_{X\gamma}$ and $c^\psi_{X\gamma}$ being free parameters to be determined in a fit.

2.5.7. $\mu^+\mu^-$

For each reaction discussed so far the electromagnetic production mechanism and the strong decay were entangled in a special way. What makes the $e^+e^- \to \mu^+\mu^-$ especially interesting is, that here we may isolate production from decay since the total cross section is by far dominated by the real-valued tree-level diagram (first diagram in Fig. 2.19) and the hadronic cross sections only contribute significantly through their interference with the mentioned dominating one.Moreover, the decays

[1]We can get equally good fits to the data by replacing the triangle by the contact term, since the quality of the data does not allow one to see the different energy dependences of the two amplitudes.

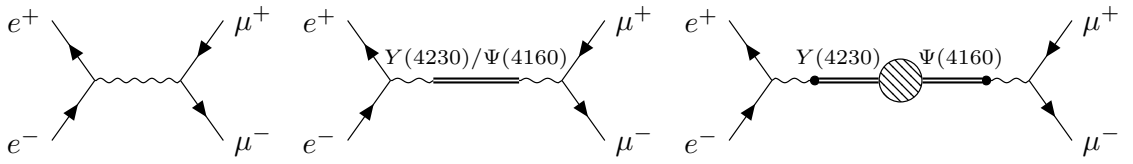

Figure 2.19.: Diagrams contributing to $e^+e^- \to \mu^+\mu^-$. The hatched circle in the rightmost diagram indicates the mixing of the two vector states driven by their common decays to the channels $DD^*\pi, J/\psi\pi\pi, \chi_{c0}\omega, J/\psi\eta$ and $X(3872)\gamma$ considered in this analysis — for details see text.

of $Y(4230)$ and $\psi(4160)$ into the same hadronic channels induce some mixing of these in the $\gamma^* \to \gamma^*$ transition amplitudes. The diagrams contributing to the process are shown in Fig. 2.19. The mentioned mixing of the two vector resonances is depicted here as the hatched blob. The imaginary part of this mixing amplitude is given by the respective interference terms that contribute also to the various exclusive hadronic channels discussed above. It is dominated by the transitions $Y(4230) \to D\bar{D}^*\pi \to \psi(4160)$, since the $D\bar{D}^*\pi$ cross section is by far the largest hadronic cross section. Therefore, the simultaneous study of the hadronic channels and the $e^+e^- \to \mu^+\mu^-$ channel provides a sanity check for the size of the induced mixing of the vector states, which turns out to be significant.
As discussed we consider three main contributions for $e^+e^- \to \mu^+\mu^-$, namely

$$\sigma_{e^+e^-\to\mu^+\mu^-} \;=\; \sigma^{\text{tree}}_{e^+e^-\to\mu^+\mu^-}\,|1+\mathcal{A}_R+\mathcal{A}_{\text{mix}}|^2$$

with

$$\sigma^{\text{tree}}_{e^+e^-\to\mu^+\mu^-} = \frac{4\pi\alpha^2}{3s} \tag{2.62}$$

for the tree level amplitude and we introduced

$$\mathcal{A}_R = \sum_{R=Y,\psi} g_{\gamma R} G_R g_{\gamma R} \tag{2.63}$$

and

$$\mathcal{A}_{\text{mix}} = \sum_{R\neq R'} g_{\gamma R} G_R \mathcal{M}^{RR'}_{\text{mix}} G_{R'} g_{\gamma R'}\ , \tag{2.64}$$

where $g_{\gamma R} = \exp(i\delta_{R\gamma}) e m_R^2/f_R$ defined in Eq. (1.113) with $\delta_{R\gamma}$ denoting a phase factor discussed in Sec. 2.6. The individual terms in Eq. (2.62) represent the different diagrams shown in Fig. 2.19. The imaginary part of $\mathcal{M}^{RR'}_{\text{mix}}$ is fixed by unitarity and can be reconstructed from the optical theorem

$$\text{Im}\,\mathcal{M}^{RR'}_{\text{mix}} = \frac{1}{2}\sum_f \int \text{d}\Pi_f\ \ \mathcal{M}^*(R' \to f)\mathcal{M}(R \to f)\,, \tag{2.65}$$

where $f = DD^*\pi, \chi_{c0}\omega, J/\psi\eta$ and $X(3872)\gamma$ are all final states with significant contributions from both $\psi(4160)$ and $Y(4230)$ studied in this work. Note that the sum runs over all allowed final states with the given particle content — accordingly, $f = [DD^*\pi]$ should be understood as

$$\begin{aligned}[DD^*\pi] =&\{D^-D^{*0}\pi^+, D^-D^{*+}\pi^0, D^+\bar{D}^{*0}\pi^-,\\ &D^+D^{*-}\pi^0, D^0D^{*+}\pi^-, D^0D^{*0}\pi^0,\\ &D^0D^{*-}\pi^+, D^0\bar{D}^{*0}\pi^0\}\,.\end{aligned} \tag{2.66}$$

Since all those channels are connected via isospin symmetry, they can be included via a proper multiplicity factor — clearly for that we need to neglect, e.g., the mass differences between the different channels. For example, for $DD^*\pi$ we denote decay amplitudes for the transition of $Y(4230)$ and $\psi(4160)$ to the experimentally measured channel $D^0D^{*-}\pi^+$ as A and B, respectively,

$$\begin{aligned}\mathcal{M}(Y \to D^0D^{*-}\pi^+) =&A\\ \mathcal{M}(\psi \to D^0D^{*-}\pi^+) =&B\,,\end{aligned} \tag{2.67}$$

where in accordance to Eq. (2.64) A and B do not contain the resonance propagators, but only the decay vertices. Summing over all channels one therefore obtains

$$\begin{aligned}\operatorname{Im}\mathcal{M}_{\text{mix}}^{Y(4230)\psi(4160)} &= \frac{1}{2}\sum_f \int \mathrm{d}\Pi_f\, \mathcal{M}^*(\psi \to f)\mathcal{M}(Y \to f)\\ &= \frac{1}{2}\int \mathrm{d}\Pi \quad 4\left(B^*A + \frac{1}{2}B^*A\right)\\ &= \frac{1}{2}\int \mathrm{d}\Pi \quad 6B^*A\,,\end{aligned} \tag{2.68}$$

where $f \in [DD^*\pi]$ was defined in Eq. (2.66). The factor 4 in Eq. (2.68) arises from the four different decay modes of the $Y(4230)$ wave function given in Eq. (2.5). For each mode the subsequent D_1 decay can produce a charged or a neutral pion, e.g. D_1^0 can decay into $D^{*\,0}\pi^0$ and $D^{*\,+}\pi^-$, where the amplitudes scale as 1 and $1/\sqrt{2}$, respectively, due to the isospin factors. The additional factors arising in the other channels are 3/2 for $J/\psi\pi\pi$ and 1 for $\chi_{c0}\omega, J/\psi\eta$ and $X(3872)\gamma$. The real part of $\mathcal{M}_{\text{mix}}^{RR'}$ can in principle also be constructed dispersively, however, there is still freedom in the subtraction constant. So for now we just approximate it via a real constant

$$\mathcal{M}_{\text{mix}}^{RR'} = \frac{c_{\text{mix}}}{2} + \frac{i}{2}\sum_f \int \mathrm{d}\Pi_f \mathcal{M}^*(R' \to f)\mathcal{M}(R \to f)\,. \tag{2.69}$$

2.6. Fit Strategy, Results and Discussion

In 2022 and 2023 BESIII published new XYZ data sets for $J/\psi\pi^+\pi^-$ [67] and $D^0D^{*-}\pi$ [121] with very impressive statistics. Those data clearly highlight the asymmetric lineshapes of the total cross sections in these two channels. It turns out that from those channels most of the parameters specific for the $Y(4230)$ are fixed. The $Z_c(3900)$ shows up prominently only in the $D\bar{D}^*$ [133] and $J/\psi\pi^\pm$ [134] subsystems of those channels. To get a better constraint on the light quark SU(3) singlet and octet components (for details see Appendix 2.4) we also include $J/\psi K^+K^-$ in the first fit. This may overestimate the contributions of the contact term in $J/\psi K^+K^-$ to some extend as it needs to compensate for a possible contribution from the missing $Z_{cs}(4000)$ triangle, but allows us to reduce the correlation of the parameters. We do not include the data for the $J/\psi\pi^0\pi^0$ channel in the fit, due to their reduced statistics in comparison to $J/\psi\pi^+\pi^-$. Since $\mu^+\mu^-$ is the only channel showing a clear separation of the $Y(4230)$ and $\psi(4160)$ signals and their interference, it is also included in the first fit. This further allows us to properly separate photon and strong couplings, since in the hadronic channels they only appear as a product. With this in mind, our fit strategy is the following:

1. The resonance parameters of the $Y(4230)$ and $Z_c(3900)$, as well as the channel dependent parameters of $D^0D^{*-}\pi$, $J/\psi\pi^+\pi^-$, $J/\psi K^+K^-$ and $\mu^+\mu^-$ are fitted simultaneously to the $D^0D^{*-}\pi$, $J/\psi\pi^+\pi^-$, $J/\psi K^+K^-$ and $\mu^+\mu^-$ total cross sections, the $D\bar{D}^*$, $J/\psi\pi^\pm$ and $\pi^+\pi^-$ invariant mass distributions, and the pion Jackson angle extracted from $D^0D^{*-}\pi^+$.

2. With the resonance and channel dependent parameters of $D^0D^{*-}\pi^+$, $J/\psi\pi^+\pi^-$ and $\mu^+\mu^-$ being fixed, the remaining parameters in the channels $\chi_{c0}\omega, J/\psi\eta$ and $X(3872)\gamma$ are fitted to the corresponding cross sections data.

3. At last, the parameters obtained in the previous steps are used as initial parameters for a global fit to all observables.

If we were working with a complete formalism, with all relevant channels dynamical and unitarity imposed, all parameters would necessarily be real. However, here some ingredients are approximated. e.g. as shown in Ref. [135] the direct transition of a photon to the $D_1(2420)\bar{D}$ intermediate state that predominantly couples to the $Y(4230)$, if it is a hadronic molecule, is suppressed by heavy quark spin symmetry, since this narrow D_1 state has a light quark cloud with $j_\ell = 3/2$. On the other hand, there is no such suppression for the transition of the photon to $D_1(2430)\bar{D}$, where the broad $D_1(2430)$ has its light quark cloud with $j_\ell = 1/2$. The $D_1(2430)\bar{D}$ intermediate state may thus act as a doorway state to feed the production of the molecule. This effect can be included effectively via a complex coupling of the $Y(4230)$ to the photon.

Moreover, the $\psi(4160)$ production from a photon sits in the tail of the $\psi(4040)$ [74] — an effect which may also be included by allowing for a complex coupling. It is worth noting that, while all hadronic cross sections are sensitive to the difference of those two phases only, the leptonic cross section $e^+e^- \to \mu^+\mu^-$ probes the phases individually, as shall be discussed below. It turns out that all other parameters of the model can be chosen real valued.

The results of the fits are shown in Fig. 2.20 to Fig. 2.23, the parameters and statistical uncertainties that emerge from the fit are listed in Table 2.1 at the end of this section. We see that the interplay of the $\psi(4160)$ and $Y(4230)$ is important and shows a non-trivial impact in almost all final states. This naturally explains the large scatter of the resonance parameters of the $Y(4230)$ in the single channel analyses of BESIII — c.f. Fig. 2.1.

With the central values of the parameters fixed in the fits, the pole parameters of the $Y(4230)$ can be extracted from its propagator. We find

$$\sqrt{s_{\text{pole}}^{Y(4230)}} = \left(4227 \pm 4 - \frac{i}{2}\left(50^{+8}_{-2}\right)\right)\ \text{MeV}\,, \tag{2.70}$$

where the uncertainty estimation is described in section 2.7.

We now discuss the results for the various channels in some detail. The results for the $D^0D^{*-}\pi$ channel are shown in Fig. 2.20. The apparent peak structure around 4.22 GeV emerges in our study from the interplay of the $\psi(4160)$ and $Y(4230)$. Remarkably, this interplay manifests differently in the $D^0D^{*-}\pi$ and $J/\psi\pi\pi$ channels — we refer to Fig. 2.5 for an illustration. In addition to this, we find a strong enhancement at the $D_1\bar{D}$ threshold in the cross section, mainly driven by the prominent D_1 decay in D-wave. The deviations of our results from the data, starting around 4.35 GeV, are expected, as the molecular scenario predicts an additional bound state in the $D_2\bar{D}^*$ channel [82, 104, 105][2], which will be included in a subsequent study.

The peak at low $D\bar{D}^*$ invariant masses is generated by the interplay of the tree-level two-step decay $Y(4230) \to D_1\bar{D} \to D^*\pi\bar{D}$, the contact mechanism and the triangle operator. The last two mechanisms involve the rescattering of $D\bar{D}^*$ into the $Z_c(3900)$. The resonance parameters of the $Z_c(3900)$ are very poorly constrained. The fit seems to prefer masses slightly above the $D\bar{D}^*$ threshold, however, for the whole mass range of approximately $m_Z \in [3.86, 3.9]$ GeV, the data are described with similar quality. In the current fit the pole closest to the real axis of the $Z_c(3900)$ appears at the $+-$ sheet, respectively, with $\sqrt{s_{\text{p}}} = (3884 - i44/2)$ MeV. In comparison to Ref. [118] we find a slightly higher mass, however, double the width for the $Z_c(3900)$.

[2]Another bound state is expected in the $D_1\bar{D}^*$ channel, however, this channel does predominantly decay into $D^*\bar{D}^*\pi$ and not into the channel studied here, $D^*\bar{D}\pi$.

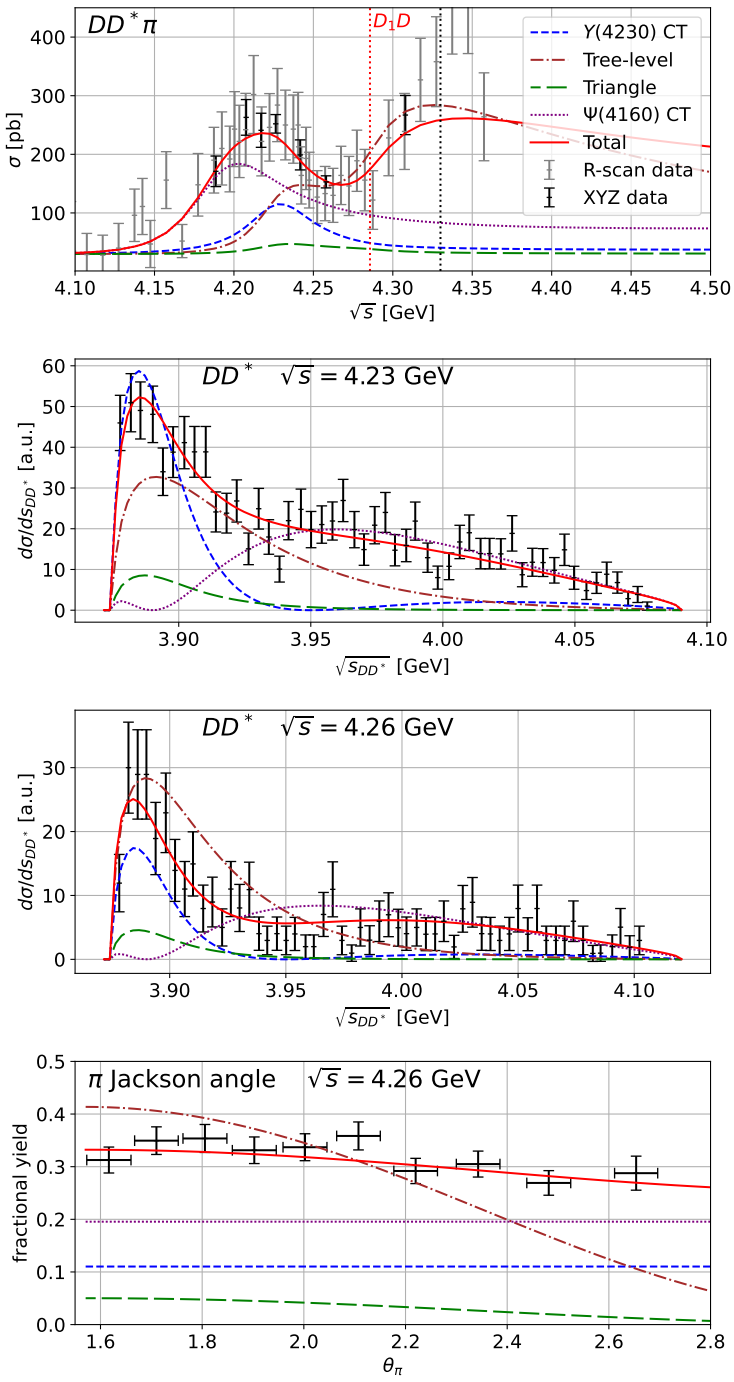

Figure 2.20.: Fit results for the $D^0D^{*-}\pi$ cross section, the D^0D^{*-} invariant mass distribution and the pion Jackson angle. $D^0D^{*-}\pi^+$ R-scan and XYZ data are from Ref. [121], D^0D^{*-} invariant mass distribution is from Ref. [133].

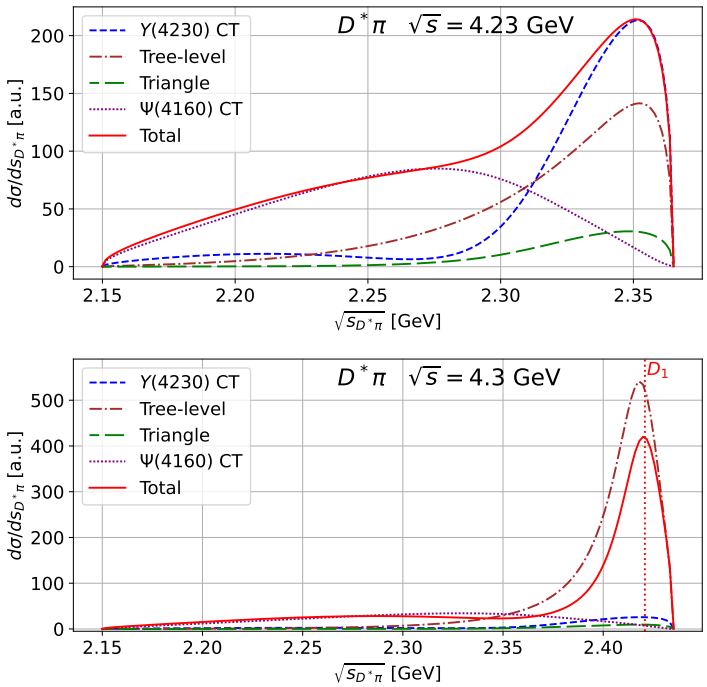

Figure 2.21.: Predictions for the $D^*\pi$ invariant mass distributions to be measured in $e^+e^- \to \bar{D}D^*\pi$. The left (right) panel shows our prediction at 4230 (4300) MeV.

It remains to be seen if this feature is caused by the incomplete $\pi\pi - K\bar{K}$ final state interaction used in this work. The data for the pion Jackson angle are also reproduced well. Contrary to Ref. [95], in this study the S-wave is more prominent due to the presence of the $\psi(4160)$ as well as the S-wave decay of the $D_1(2420)$.

Naturally, a prominent contribution from the $D_1\bar{D}$ intermediate state not only influences strongly the energy dependence of the total cross section but also the $D^*\pi$ invariant mass distributions. Our predictions for those at total energies near the $Y(4230)$ pole location and near the nominal $D_1\bar{D}$ threshold are shown in the left and right panel of Fig. 2.21, respectively. In both panels the peak from the D_1 is clearly visible at the upper end of the spectrum. While the data currently available do not allow us to provide an unambiguous determination of the various parameters leaving some freedom in the actual height of the D_1 signal, the presence of such a peak is a model independent prediction of the molecular scenario. Any model that does not account for the $D_1\bar{D}$ as a prominent component of the $Y(4230)$ wave function will not show such a structure — as such this invariant mass distribution is a crucial observable to either support or disprove the molecular picture.

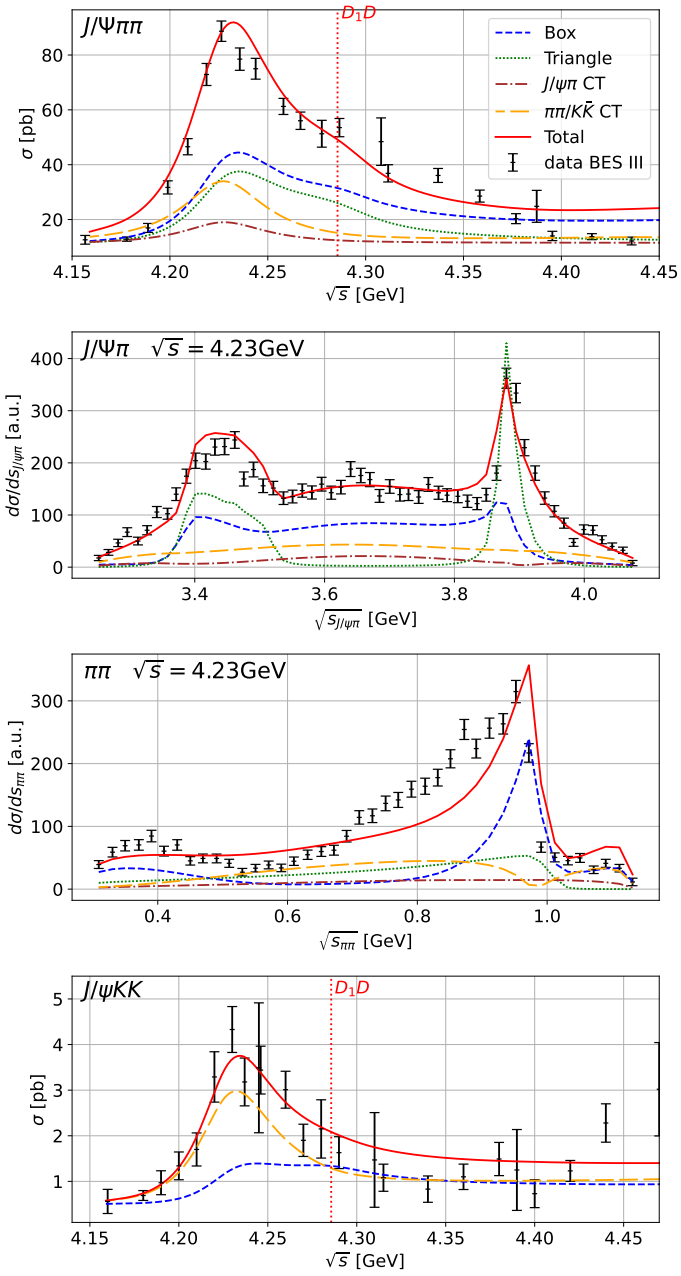

Figure 2.22.: Fit results for the $J/\psi\pi^+\pi^-$ cross section and the $J/\psi\pi^\pm$ and $\pi^+\pi^-$ invariant mass distributions, as well as results for the $J/\psi K^+K^-$ cross section. $J/\psi\pi^+\pi^-$ XYZ data from Ref. [67], $J/\psi\pi^\pm$ and $\pi^+\pi^-$ invariant mass distribution from Ref. [134]. The data for the $J/\psi K\bar{K}$ channel are taken from Ref. [76].

The results for the $J/\psi\pi\pi$ final state are shown in Fig. 2.22. A linear non-interfering background of 9 pb is added due to the presence of the $J/\psi\pi$ continuum. The loop contributions, dominant in the molecular scenario, enhance the cross section at the $D_1\bar{D}$ threshold, allowing for a description of the highly asymmetric lineshape with just a single pole — in the experimental analyses of Refs. [66, 67] this asymmetry was generated by the additional state $Y(4320)$ as described in the introduction. It should be noted that also in Ref. [108] an analysis is presented, where, in particular, the $J/\psi\pi\pi$ data is described with essentially the same resonance content as presented here, along with the addition of a $\psi(4415)$ state, but without including threshold effects. In this case, the asymmetry of the peak in the total cross section is driven by interferences, predominantly involving $\psi(4160)$ and $\psi(4415)$. While we regard our explanation of the data as more natural, since the data indicate some structure right at the $D_1\bar{D}$ threshold, at some point experiment will allow us to choose between the two explanations, not only since the energy dependences in the mentioned energy range are different (but not sufficiently to be distinguished given the current quality of the data), but also since an analysis of the type presented in Ref. [108] will provide completely different $D\bar{D}^*$ and $D^*\pi$ invariant mass distributions compared to the ones shown in Figs. 2.20 and 2.21, respectively.

The $J/\psi\pi^\pm$ invariant mass distribution shows a prominent peak, generated by the $Z_c(3900)$ pole, the $D^*\bar{D}$ threshold and the nearby triangle singularity, and its reflection. In principle, the $J/\psi\pi^\pm$ and D^0D^{*-} lineshape can also be described by just including the triangles and introducing a contact interaction for $D\bar{D}^* \to D\bar{D}^*$, where the cusp is then generated simply by kinematic effects of the $D\bar{D}^*$ rescattering without any resonance structure. However, we find that the strength of the $D\bar{D}^* \to D\bar{D}^*$ transition potential, necessary for producing the pronounced structure in the $D^*\bar{D}$ invariant mass distribution, becomes too large to justify a perturbative approach. We confirm the observation made in Ref. [136] that with this strength parameter the next order in $D\bar{D}^*$ scattering becomes larger than the perturbative rescattering; moreover, resumming the scattering series generates a pole in the subsystem. Based on this, we argue that the existing data calls for the presence of a $Z_c(3900)$ pole.

The fit result for $J/\psi K^+K^-$ is shown in the top right of Fig. 2.22. Note that the line shape emerging for this channel is closely linked to that of the $J/\psi\pi\pi$ channel and no new independent parameters are entering for this hidden strangeness channel. In our fit, the contact term is the dominant contribution. A possible reason is that it needs to absorb the effects of the $Z_{cs}(4000)$ and the corresponding triangle diagrams not included in this analysis, though their main effect is expected at the energies above those considered here. The boxes again show a very strong enhancement in the cross section at the $D_1\bar{D}$ threshold explaining the apparent asymmetry in the data. We find the $Y \to J/\psi\pi^+\pi^- \to J/\psi K^+K^-$ contribution generated by the

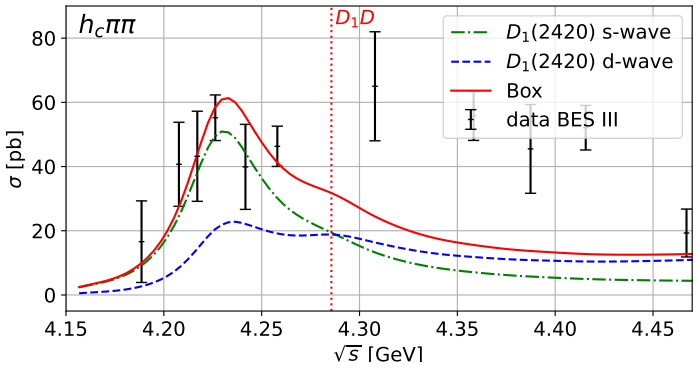

Figure 2.23.: Prediction for the $h_c\pi^+\pi^-$ cross section. The data are taken from Ref. [73].

$\pi\pi/K\bar{K}$ FSI to be by far dominant in the studied energy range, in comparison to the box with strange D-mesons, as shown in Fig. 2.13, where only the $D_1\bar{D}$ cut goes on-shell. At higher energies, above the $D_s^*\bar{D}K$ threshold at about 4.47 GeV, the $D_s^*\bar{D}K$ intermediate state in this box will go on shell. Consequently, we expect a more pronounced contribution from the strange source in this mass range. Starting from this energy also the $Z_{cs}(4000)$ generated via the triangle mechanism should contribute considerably.

It should be stressed that in our analysis the unusual energy dependences of the $J/\psi\pi\pi$ and $J/\psi K\bar{K}$ cross sections emerge from the same physics, which is natural given the approximate SU(3) flavor symmetry of QCD, while in the experimental analyses the former is driven by an interference of the $Y(4230)$ with the new resonance $Y(4320)$ [67] and the latter predominantly by the shifted threshold for $J/\psi\bar{K}K$ vs. $J/\psi\pi\pi$ with some small distortion from an interference with another new resonance, called $Y(4500)$ [76].

To complete the discussion of the final states with three hadrons, in Fig. 2.23 we show the cross sections with an h_c in the final state. These rates are of particular interest, since the h_c has its $\bar{c}c$ pair in the spin singlet state, which was originally produced in a spin triplet via its coupling to the photon. Thus, in this transition the heavy quark spin changes, at odds with heavy quark spin symmetry. However, besides violations of that symmetry due to the relatively small charm quark mass, spin symmetry conservation can also be circumvented by the presence of hadronic molecules: In the molecular picture it is natural to expect the $h_c\pi\pi$ and the $J/\psi\pi\pi$ cross sections of similar order of magnitude as is confirmed by the data, since only in the presence of a molecule the two-meson loops that decorrelate the heavy quark spins appear at leading order for both channels as explained above. Moreover, by using values for both the $J/\psi D^{(*)}\bar{D}^{(*)}$ and the $h_c D^{(*)}\bar{D}^{(*)}$ couplings available in

the literature (details on how the various couplings were determined are given in App. 1.5), we can describe the cross sections in both channels, providing additional support for the molecular picture. In the $h_c\pi\pi$ channel we observe a discrepancy between the data and our prediction starting already at around 4.3 GeV. We think this reflects the omission of the $D_1\bar{D}^*$ channel in our study: Only once this channel is incorporated we can include the $Z_c(4020)$ which might be responsible at least for some part of this discrepancy.

As pointed out in the introduction, the $\psi(4160)$ needs to be included to get a consistent simultaneous description of the $J/\psi\pi\pi$ and $D^*\bar{D}\pi$ final states. We allow this well established vector charmonium state to contribute to both of these channels (as well as to all other channels included in the analysis), however, the fit reveals that no significant coupling of the $\psi(4160)$ to the $J/\psi\pi\pi$ is needed. Indeed, the fit puts the parameter $\beta_1^{(2)}$, introduced in Eq. (2.50), for the production of the $\psi(4160)$ to a value consistent with zero.

The results for the $\mu^+\mu^-$ final state are shown in the upper panel of Fig. 2.24. The cross section is completely dominated by the real tree level amplitude, shown as the first diagram in Fig. 2.19. Accordingly, following Eq. (2.62), the signal of interest to us reads to very good approximation

$$\sigma_{e^+e^-\to\mu^+\mu^-} - \sigma^{\text{tree}}_{e^+e^-\to\mu^+\mu^-} \approx 2\sigma^{\text{tree}}_{e^+e^-\to\mu^+\mu^-}\text{Re}(\mathcal{A}_R + \mathcal{A}_{\text{mix}}) \ . \tag{2.71}$$

This quantity is shown in the lower panel of Fig. 2.24. As argued above, we allow for complex couplings at the resonance-photon vertices. Contrary to all observables studied so far, where only the relative phase of the $Y(4230)$ and $\psi(4160)$ contributions played a role, this leptonic cross section is sensitive to the individual phases of these resonance contributions. The phases of those couplings are thus fixed by the fit to the $\mu^+\mu^-$ cross section.
In Ref. [74] a sum of Breit-Wigner terms with complex couplings is used to parameterize the data including the $\psi(4040), \psi(4160), S(4220) \equiv Y(4230)$ (and the $\psi(4415)$, which is, however outside our energy range of interest). We find that the complex phase $\delta_{\psi\gamma}$ called for by the fit in the production vertex of the ψ to the photon agrees within uncertainties to the one of the experimental paper. With this phase included we can reproduce the $\mu^+\mu^-$ lineshape in the energy range studied. We see that the contribution of the $\psi(4160)$ is dominant in comparison to that of the $Y(4230)$ at least in the energy below 4.2 GeV, as expected in the molecular scenario, since the coupling of a photon to the $D_1\bar{D}$ channel violates spin symmetry [83]. One should, however, keep in mind that there should also be some suppression of the coupling of the $\psi(4160)$ to the photon, if it indeed is predominantly a D-wave charmonium state.

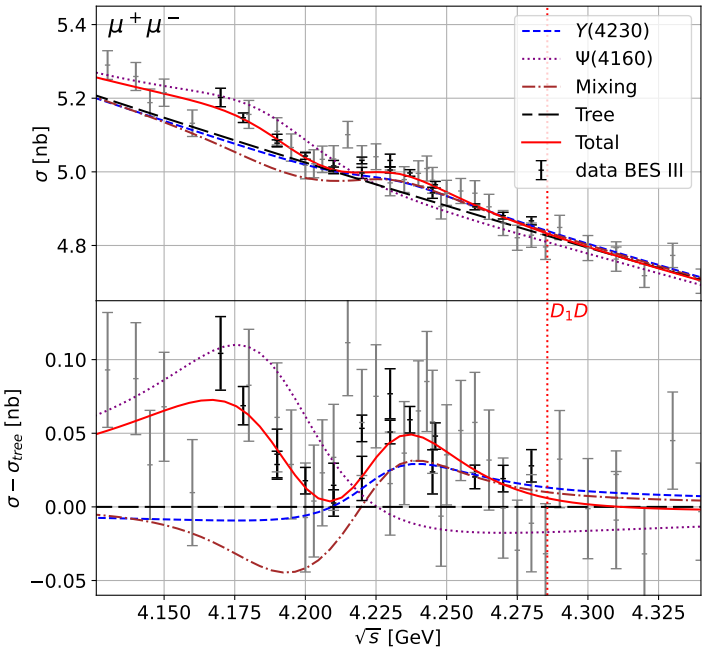

Figure 2.24.: Fit results for the $\mu^+\mu^-$ cross section. Upper panel: The measured born cross section; lower panel: The same, however, with the cross section from the tree level amplitude subtracted. The data are taken from Ref. [74], where the data points with an uncertainty smaller than 32 pb are shown in black to better highlight the structure in the data.

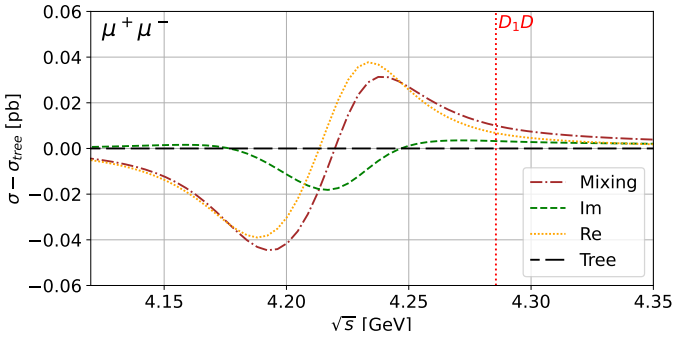

Figure 2.25.: Contributions to the cross section difference from the real and imaginary parts of the mixing of $Y(4230)$ and $\Psi(4160)$ in $e^+e^- \to \mu^+\mu^-$, denoted by $\mathcal{A}_{\text{mix}}$ in Eq. (2.64). The brown dash-dotted curves here and in Fig. 2.24 are identical.

The peak in the data near 4230 MeV in our fits emerges from both the interference of the two resonances and the $Y(4230)$ itself. The main contribution to the imaginary part of the pertinent mixing matrix element of the $\psi(4160)$ and the $Y(4230)$ is generated from the $D\bar{D}^*\pi$ intermediate state — this part is fixed completely by the data for $e^+e^- \to D\bar{D}^*\pi$. As outlined above, the corresponding real part is here taken as a free parameter that is adjusted in the fit. It is reassuring, however, that the real and the imaginary part of the mixing amplitude contribute with comparable strength, as shown in figure 2.25. Although the energy dependence emerging from the real and imaginary part of the mixing amplitude, $\mathcal{A}_{\text{mix}}$, resembles that of a single resonance structure, it emerges from an interplay of the different resonance propagators as well as the mixing amplitude, $\mathcal{M}_{\text{mix}}^{RR'}$, as outlined in Eq. (2.62) and below. One may naively expect that the imaginary part of the mixing matrix element does not contribute to the total cross section significantly, as only interferences of the strong amplitudes with the real tree level amplitude matter quantitatively. However, the phases of the resonance propagators in Eq. (2.62) non-trivially mix real and imaginary parts of the mixing amplitude, allowing both contributions to interfere with the tree level amplitude.

We now turn to a discussion of remaining hadronic two-particle final states, also included in Fig. 2.26. As one can read from the figure, the energy dependences of the $\chi_{c0}\omega$, the $J/\psi\eta$, and the $X(3872)\gamma$ cross section are rather different: While the first one shows a very narrow structure, the structure in the second is already a lot broader and the one in the last is more than four times as broad as the first — this is also reflected in the resonance parameters extracted in the single channel analyses of the BESIII collaboration collected in Fig. 2.1. In contrast to this, our model allows us to describe all three cross sections with consistent resonance parameters as a result of an interplay of the two vector resonances $\psi(4160)$and $Y(4230)$: the narrow peak in the $\chi_{c0}\omega$ channel emerges from a destructive interference of the triangle diagram shown in Fig. 2.16a and the $\psi(4160)$ contact term, shown in Fig. 2.16c, since the energy dependences of the two contributions are quite different, as can be clearly seen in Fig. 2.26 — we included the width of the ω by a convolution of the cross section with the omega spectral function as explained above which is the origin of the not vanishing cross section below the nominal $\chi_{c0}\omega$ cross section. The mechanism we propose here is different from that studied in Ref. [137], however, the energy dependence found there appears inconsistent with that of the newest data set for this channel measured at BESIII [70]. Also for the $J/\psi\eta$ and $X(3872)\gamma$ final states the interplay of the two resonances is crucial, but less dramatic.

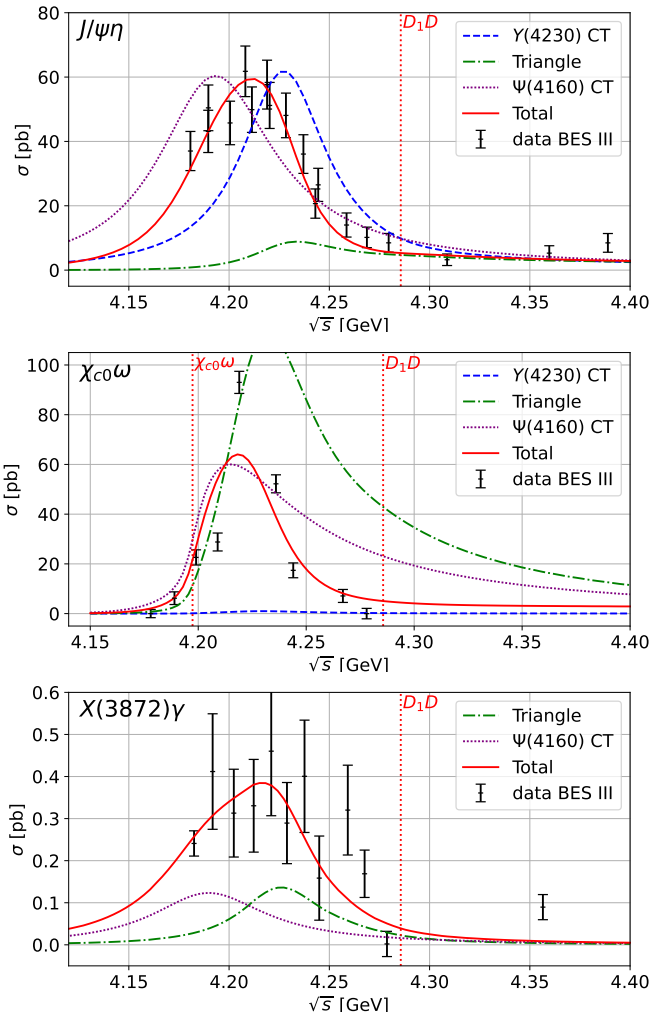

Figure 2.26.: Fit results for the $J/\psi\eta$, $\chi_{c0}\omega$ and $X(3872)\gamma$ cross section. The data sets are from Ref. [69], Ref. [70], and Ref. [72], respectively.

2.7. Pole uncertainty

Within our calculation the pole position is fixed by three parameters (see Eq. (2.11)): g_{Y0}, m_0 and Γ_{in}, with m_0 (Γ_{in}) influencing only the real (imaginary) part of the pole location and g_{Y0} influencing both. To estimate the uncertainty of the pole position we performed a χ^2 fit, however, with two approximations. First, we only allow the three resonance parameters m_0, g_{Y0} and Γ_{in} to vary. Second, as $J/\psi\pi\pi$ has the best statistics of all the available data and the fit suggests a negligible contribution of the $\psi(4160)$ to this channel, it is by far the most restrictive final state for the $Y(4230)$ pole location. Therefore, to estimate the uncertainty of the $Y(4230)$ pole location, we

focus solely on the $J/\psi\pi\pi$ channel. We checked that the inclusion of $D\bar{D}^*\pi$ yields no significant change to the uncertainty of the pole, supporting that the main influence on the pole position is driven by the data on the $J/\psi\pi\pi$ channel. In the analysis, we allow m_0 and Γ_{in} to vary within ± 10 MeV and g_{y0} by ± 0.2 MeV around their best fit values. These parameter ranges allow the pole to vary over a sufficiently wide range, including all values within the 1σ range around the best fit pole position. Within these ranges random combinations of the three parameters are picked under the requirement that for each parameter-set the change in the χ^2 value must lie within

$$\chi^2_{\text{best fit}} - \chi^2_{\text{random parameters}} \leq \Delta_{\chi^2}(p, 3)\,, \tag{2.72}$$

where the three in $\Delta_{\chi^2}(p, 3)$ indicates that three parameters are varied, and $p \approx 0.683$ corresponds to the 1σ band. To evaluate $\Delta_{\chi^2}(p, k)$ the χ^2 cumulative-distribution function needs to equate p

$$\frac{1}{\Gamma(k/2)}\gamma\left(\frac{k}{2}, \frac{\Delta_{\chi^2}}{2}\right) = p\,, \tag{2.73}$$

where Γ and γ denote the regular and lower incomplete Gamma functions, respectively

$$\gamma(x, a) = \int_0^a \mathrm{d}t\; t^{x-1}e^{-t}, \quad \mathrm{Re}\,(a) > 0\,. \tag{2.74}$$

Solving for $k = 3$ degrees of freedom, the 1σ deviation in the χ^2 value reads

$$\Delta_{\chi^2}(p = 1\sigma, k = 3) \approx 3.525\,.$$

The fits only included data from 4.2 to 4.35 GeV because this energy interval is expected to be under control due to the theoretical mechanisms considered in this work. As mentioned in the main text, deviations of our results from the data beyond this energy range are expected due to, in particular, the absence of contributions from the $D_1\bar{D}^*$ and $D_2\bar{D}^*$ channels. The results for $N \approx 300$ random generated parameter sets that fulfill the condition of Eq. (2.72) are shown in Fig. 2.27. The upper panel shows the obtained 1σ uncertainty band for the $J/\psi\pi\pi$ total cross section, while the bottom plot shows the corresponding spread of the pole position, which results in

$$\sqrt{s_{\text{pole}}^{Y(4230)}} = \left(4227 \pm 4 - \frac{i}{2}\left(50^{+8}_{-2}\right)\right)\ \text{MeV}\,. \tag{2.75}$$

In addition, the two plots in the middle of Fig. 2.27 demonstrate the effect of the 1σ uncertainty extracted from fits to the $J/\psi\pi\pi$ channel on the total cross sections in the $D\bar{D}^*\pi$ and $\mu^+\mu^-$ channels. As pointed out earlier, the variations in these channels are considerably less pronounced compared to those in the $J/\psi\pi\pi$ channel. Our error estimate in Eq. (2.75) is supported by the observation that the uncertainty we find using this method is of the same order of magnitude as that provided by the BESIII collaboration extracted from the $J/\psi\pi\pi$ channel.

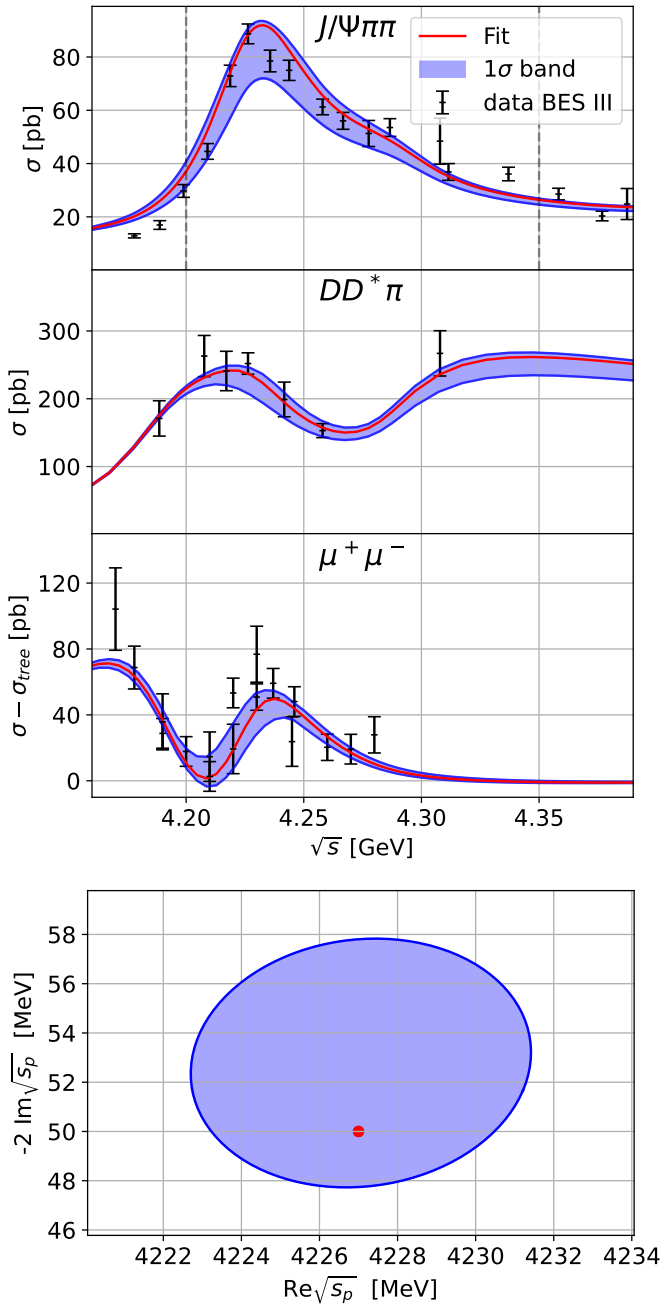

Figure 2.27.: Uncertainty estimate of the $Y(4230)$ pole position. Upper three panels: Total cross sections for $J/\psi\pi^+\pi^-, D^0D^{*-}\pi^+$ and $\mu^+\mu^-$ final states with the 1σ uncertainty band extracted from fits to the $J/\psi\pi\pi$ data and propagated to the other channels, as described in the text. Red line in all plots corresponds to the best global fit to all data considered in this study (see the main text for details). Lower panel: The best pole position of the $Y(4230)$ (red dot) and the 1σ uncertainty (blue ellipse) extracted from fits to the $J/\psi\pi\pi$ data.

	Name		Value
Y	m_Y		(4227 ± 0.4) MeV
	g_{Y0}	–	(10.4 ± 0.2) GeV
	Γ_{in}^Y		(54 ± 1) MeV
	$1/f_Y$	–	(0.012 ± 0.001)
	$\delta_{Y\gamma}$		$(17.1 \pm 0.1)^o$
ψ	$1/f_\psi$	–	(0.023 ± 0.003)
	$\delta_{\psi\gamma}$		$(67 \pm 2)^o$
Z_c	m_Z		(3884 ± 1) MeV
	g_{Z0}		(4.15 ± 0.06) GeV
	Γ_{in}^Z		(48 ± 1) MeV
$D\bar{D}^*\pi$	$\alpha_1^{(1)}$	–	(128 ± 12)
	$\alpha_2^{(1)}$	–	(3.95 ± 0.01) GeV
	$\beta_1^{(1)}$	–	(202 ± 18)
	$\beta_2^{(1)}$	–	(3.89 ± 0.1) GeV
$J/\psi\pi^+\pi^-$	$\alpha_1^{(2)}$	–	(133.9 ± 4)
	g_1	–	$(14.9 \pm 0.9)\,10^{-3}$
	g_8		$(24 \pm 1)\,10^{-3}$
	h_1	–	$(16.8 \pm 2.4)\,10^{-3}$
	h_8		$(15 \pm 0.7)\,10^{-3}$
	$\beta_1^{(2)}$		(0 ± 0.1)
	$c_{\text{CT}}^{\triangle}$	–	(0.4 ± 0.1) GeV^2
	$f_{J/\psi}$		456 MeV
$\chi_{c0}\omega$	$c_{\chi_{c0}\omega}^{\triangle}$		(1.469 ± 0.015) GeV^2
	$c_{\chi_{c0}\omega}^{Y}$		$(0.36 \pm 0.07)\,10^{-3}$
	$c_{\chi_{c0}\omega}^{\psi}$	–	$(16 \pm 0.5)\,10^{-3}$
$J/\psi\eta$	$c_{J/\psi\eta}^{Y}$		$(67.3 \pm 3.4)\,10^{-3}$ GeV^{-1}
	$c_{J/\psi\eta}^{\psi}$		$(298 \pm 11)\,10^{-3}$ GeV^{-1}
$X\gamma$	$c_{X\gamma}^{Y}$		(0.71 ± 0.15) GeV^2
	$c_{X\gamma}^{\psi}$		(0.017 ± 0.003) GeV
$\mu^+\mu^-$	c_{mix}		(0.6 ± 0.01)

Table 2.1.: Parameters of the model as determined in the fit. We find the value of $f_{J/\psi}$ to be strongly dependent on the fit range in $D^0D^{*-}\pi^+$, such that we did not assign an uncertainty to this quantity.

3. Coupled Channel $\{D_1, D_2\} - \{D, D^*\}$ Dynamics

3.1. Introduction

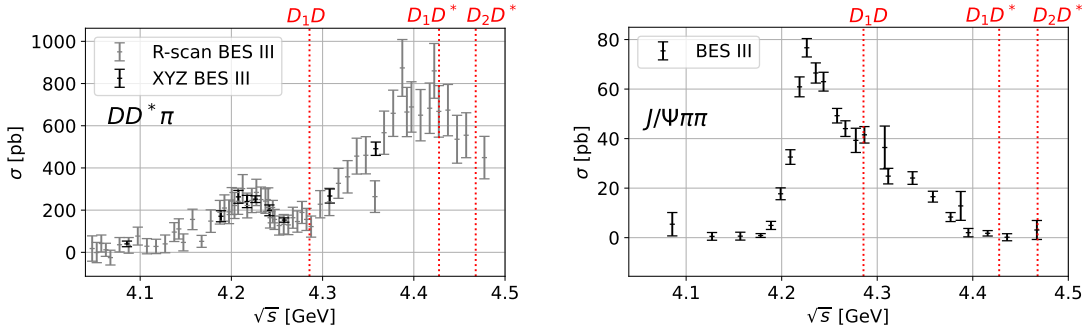

Figure 3.1.: Data for the total cross sections of $D^0D^{*-}\pi^*$ and $J/\psi\pi^+\pi^-$ showing the relevant thresholds for this study.

With the results of our initial study showing very promising results, in the next step we plan to turn to a more refined treatment to extend the energy range even further. While we focused so far solely on the $D_1\bar{D}$ intermediate state for the $Y(4230)$, heavy quark spin symmetry also calls for potential bound states in the $D_1\bar{D}^*$ and $D_2\bar{D}^*$ channel for $J^{PC} = 1^{--}$. Their respective thresholds in the $D^0D^{*-}\pi$ and $J/\psi\pi^+\pi^-$ channels are shown in Fig. 3.1. In the case of the $D^0D^{*-}\pi$ final state, the $D_1\bar{D}^*$ channel decouples, which is also reflected in the derivation of the coupled channel potential below. Potential experimentally observed candidates are the $Y(4360)$ as well as the $\psi(4415)$, which are located roughly 50 MeV below the $D_1\bar{D}^*$ and $D_2\bar{D}^*$ threshold, respectively. The remaining resonance of the vector channel, namely $\psi(4660)$, is also hypothesized to be a molecular state of $\psi' f_0(980)$ [138]. The improvements compared to our previous study planned for the follow up work are:

- Inclusion of the HQSS spin partners of $D_1\bar{D}$, namely $D_1\bar{D}^*$ and $D_2\bar{D}^*$. This not only allows us to study the full coupled channel dynamics and significantly

extend the energy range considered but also to include additional resonances like the $Z_c(4020)$, which plays a significant role in the $h_c\pi$ invariant mass distribution for $e^+e^- \to h_c\pi\pi$.

- Contact terms derived from HQSS will be considered non-perturbatively in a coupled channel Lippmann-Schwinger equation.
- In regards to the previous point, a proper study on the effect of the one-pion exchange makes it also necessary to include the momentum-dependent width of the D_1 and D_2 consistent with unitarity. The width of the D^* from its decay to $D\pi$ is with approximately 80 keV still insignificant for our present study, such that it is well approximated by a constant or even neglected completely.
- Full SU(3) flavor symmetry is considered, which allows us to extend our study in $e^+e^- \to J/\psi\bar{K}K$ with the inclusion of the $Z_{cs}(4000)$.
- The conventional charmonium state $\psi(4160)$, as well as $\psi(4040)$ and potential others are included unitarized in a K-matrix formalism. This also allows us to study the P-wave channels $D\bar{D}, D\bar{D}^*$ and $D^*\bar{D}^*$.

The effect of the most important inelastic channels, which are not related to a direct (tree-level like) decay of $D_1\bar{D}$, $D_1\bar{D}^*$ and $D_2\bar{D}^*$, can be effectively included by adding an imaginary part to the contact interaction. This imaginary part is fixed by the intermediate loops of the inelastic channels, such that the construction is consistent with unitarity as presented in Refs. [139–141]. We automatically include inelastic channels of the kind $D^*\bar{D}\pi, D^*\bar{D}^*\pi, ...$ through the resonant contributions of D_1 and D_2. As demonstrated in Sec. 2.5, a resonance propagator captures the final state interaction, and as a consequence of unitarity, tree-level amplitudes will cancel. Consequently, the effects of $D\pi$ and $D^*\pi$, corresponding to the tree-level decays of the resonances D_1 and D_2, are included via the momentum-dependent width in the propagators, as demonstrated later in Fig 3.5. The effect of multi-body channels containing more than 4 particles like $D^*\bar{D}\pi\pi, D\bar{D}\pi\pi\pi, ...$ are strongly suppressed by their corresponding phase space and as such, can be safely neglected.

3.2. Definitions

With the wavefunction of the $Y(4230)$ given in Eq. (2.5), we can follow an analogous construction for the wavefunction of a $D_1\bar{D}^*$ and $D_2\bar{D}^*$ bound state. The C-convention of the lagrangian in Eq. (1.73)

$$\begin{aligned} C|D\rangle &= |\bar{D}\rangle, \quad C|D^*\rangle = -|\bar{D}^*\rangle \\ C|D_1\rangle &= |\bar{D}_1\rangle, \quad C|D_2\rangle = -|\bar{D}_2\rangle \end{aligned} \tag{3.1}$$

results in

$$\begin{aligned} |Y_1(C=-1)\rangle &= \frac{1}{\sqrt{2}}\left(|D_1\bar{D}\rangle - |D\bar{D}_1\rangle\right) \\ |Y_2(C=-1)\rangle &= \frac{1}{\sqrt{2}}\left(|D_1\bar{D}^*\rangle - |D^*\bar{D}_1\rangle\right) \\ |Y_3(C=-1)\rangle &= \frac{1}{\sqrt{2}}\left(|D_2\bar{D}^*\rangle - |D^*\bar{D}_1\rangle\right) , \end{aligned} \tag{3.2}$$

where we expect a large overlap of the $Y(4230)$ with Y_1. Although, the convention of the C-operator acting on D^* suggests the same relative sign for the 2 components of the $|Y_2\rangle$ wave function, the vector vector axial-vector coupling of $Y_2 \to D_1\bar{D}^*$ must scale with the levi-civita tensor and may be expressed by

$$\mathcal{L}_{Y_2 D_1 D^*} \propto \epsilon^{ijk}\left(\bar{D}^{*\,i\,\dagger} Y_2^j D_1^{k\,\dagger} - \bar{D}_1^{k\,\dagger} Y_2^j D^{*\,i\,\dagger}\right) + \text{h.c.} , \tag{3.3}$$

such that the exchange of $|\bar{D}_1 D^*\rangle = -|D^*\bar{D}_1\rangle$ generates an additional minus sign. Possible partial waves of the two-meson systems for total $J^{PC} = 1^{--}$ are

$$\begin{aligned} &\alpha,\beta = D_1\bar{D} && \{^3S_1,\ ^3D_1\} \\ &\alpha,\beta = D_1\bar{D}^* && \{^3S_1,\ ^3D_1,\ ^5D_1\} \\ &\alpha,\beta = D_2\bar{D}^* && \{^3S_1,\ ^3D_1,\ ^5D_1,\ ^7D_1,\ ^7F_1\} , \end{aligned} \tag{3.4}$$

where the individual partial waves of the two-meson states are labeled as $^{2S+1}L_J$, with S, L, and J denoting the spin, relative angular momentum and total angular momentum of the two-meson system, respectively.

3.3. Potential

3.3.1. Contact interaction

In our initial study, where we only considered the $D_1\bar{D}$ channel, it was sufficient to describe the S-wave contact interaction with a single constant. To properly describe the contact terms of the complete $\{D_1, D_2\} \otimes \{D, D^*\}$ multiplet, we employ a more sophisticated ansatz consistent with heavy quark spin symmetry. As the interaction is independent of heavy quark spin $s_\mathrm{h} = s_{\mathrm{h}1} + s_{\mathrm{h}2}$ and J, we may choose the following eigenbasis for the interaction Hamiltonian

$$|s_{\mathrm{h}1}, s_{\mathrm{h}2}, s_\mathrm{h}; j_{\ell 1}, j_{\ell 2}, j_\ell; J\rangle = |s_\mathrm{h}; j_{\ell 1}, j_{\ell 2}, j_\ell\rangle . \tag{3.5}$$

Consequently, at leading order in the heavy quark limit, four independent contact interactions F emerge for isospin $I = 0$ and $I = 1$ [25], denoted by

$$\begin{aligned} F &= \langle s_\mathrm{h}; j_{\ell 1}, j_{\ell 2}, j_\ell | H_I | s_\mathrm{h}; j'_{\ell 1}, j'_{\ell 2}, j_\ell \rangle \\ F^\mathrm{d}_{j_\ell} &= \langle s_\mathrm{h}; \tfrac{1}{2}, \tfrac{3}{2}, j_\ell | H_I | s_\mathrm{h}; \tfrac{1}{2}, \tfrac{3}{2}, j_\ell \rangle \\ F^\mathrm{c}_{j_\ell} &= \langle s_\mathrm{h}; \tfrac{1}{2}, \tfrac{3}{2}, j_\ell | H_I | s_\mathrm{h}; \tfrac{3}{2}, \tfrac{1}{2}, j_\ell \rangle \,. \end{aligned} \tag{3.6}$$

In the current basis, the light- and heavy-quark spins are coupled for each meson individually. We can also choose to couple the light- and heavy degrees between the two mesons to a total $s_{\mathrm{h}1} \otimes s_{\mathrm{h}2} = s_\mathrm{h}$ and $j_{\ell 1} \otimes j_{\ell 2} = j_\ell$, with $J = s_\mathrm{h} \otimes j_\ell$ denoting the total angular momentum of the complete system. To relate the two bases we can use the transformation [25]

$$\begin{aligned} |s_{\mathrm{h}1}, j_{\ell 1}, j_1; s_{\mathrm{h}2}, j_{\ell 2}, j_2; J\rangle = &\sum_{s_\mathrm{h}, j_\ell} \sqrt{(2j_1+1)(2j_2+1)(2j_\ell+1)(2s_\mathrm{h}+1)} \\ &\times \begin{Bmatrix} s_{\mathrm{h}1} & s_{\mathrm{h}2} & s_\mathrm{h} \\ j_{\ell 1} & j_{\ell 2} & j_\ell \\ j_1 & j_2 & J \end{Bmatrix} |s_{\mathrm{h}1}, s_{\mathrm{h}2}, s_\mathrm{h}; j_{\ell 1}, j_{\ell 2}, j_\ell, J\rangle \,, \end{aligned} \tag{3.7}$$

with $\{...\}$ denoting the Wigner-9j-symbol [142]. For a physics-related application of the Wigner-9j-symbol see Refs. [143, 144]. Following the convention of Eq. (3.2), the resulting states for the $D_1\bar{D}$, $D_1\bar{D}^*$ and $D_2\bar{D}^*$ channels are

$$\begin{aligned} |D_1\bar{D}\rangle &= \tfrac{1}{2}|0; \tfrac{3}{2}, \tfrac{1}{2}, 1\rangle + \tfrac{\sqrt{2}}{4}|1; \tfrac{3}{2}, \tfrac{1}{2}, 1\rangle + \tfrac{\sqrt{10}}{4}|1; \tfrac{3}{2}, \tfrac{1}{2}, 2\rangle \\ |D\bar{D}_1\rangle &= \tfrac{1}{2}|0; \tfrac{1}{2}, \tfrac{3}{2}, 1\rangle - \tfrac{\sqrt{2}}{4}|1; \tfrac{1}{2}, \tfrac{3}{2}, 1\rangle + \tfrac{\sqrt{10}}{4}|1; \tfrac{1}{2}, \tfrac{3}{2}, 2\rangle \\ \\ |D_1\bar{D}^*\rangle &= \tfrac{\sqrt{2}}{4}|0; \tfrac{3}{2}, \tfrac{1}{2}, 1\rangle + \tfrac{3}{4}|1; \tfrac{3}{2}, \tfrac{1}{2}, 1\rangle - \tfrac{\sqrt{5}}{4}|1; \tfrac{3}{2}, \tfrac{1}{2}, 2\rangle \\ |D^*\bar{D}_1\rangle &= -\tfrac{\sqrt{2}}{4}|0; \tfrac{1}{2}, \tfrac{3}{2}, 1\rangle + \tfrac{3}{4}|1; \tfrac{1}{2}, \tfrac{3}{2}, 1\rangle + \tfrac{\sqrt{5}}{4}|1; \tfrac{1}{2}, \tfrac{3}{2}, 2\rangle \\ \\ |D_2\bar{D}^*\rangle &= \tfrac{\sqrt{10}}{4}|0; \tfrac{1}{2}, \tfrac{3}{2}, 1\rangle - \tfrac{\sqrt{5}}{4}|1; \tfrac{1}{2}, \tfrac{3}{2}, 1\rangle - \tfrac{1}{4}|1; \tfrac{1}{2}, \tfrac{3}{2}, 2\rangle \\ |D^*\bar{D}_2\rangle &= \tfrac{\sqrt{10}}{4}|0; \tfrac{1}{2}, \tfrac{3}{2}, 1\rangle + \tfrac{\sqrt{5}}{4}|1; \tfrac{1}{2}, \tfrac{3}{2}, 1\rangle - \tfrac{1}{4}|1; \tfrac{1}{2}, \tfrac{3}{2}, 2\rangle \,. \end{aligned} \tag{3.8}$$

Realizing that the total spin of the heavy quark and anti-quark s_h must be conserved at leading order in HQSS and using the orthogonality of the states in Eq. (3.8), we

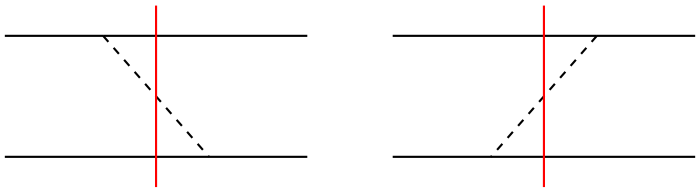

Figure 3.2.: Contributions to the one-pion exchange potential derived from time-ordered perturbation theory. The solid lines label D, D^*, D_1, D_2 mesons and the dashed line label the pion.

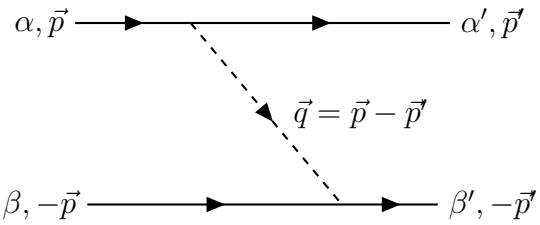

Figure 3.3.: Kinematics of the one-pion exchange for in the center of mass frame for incoming particles α, β with momentum p and outgoing particles α', β' with momentum p'.

can calculate the S-wave potential V_c according to Eq. (3.6), resulting in

$$\begin{aligned}
(V_{\mathrm{C}})_{11} &= \tfrac{1}{8}(3F_1^{\mathrm{d}} + 5F_2^{\mathrm{d}} - F_1^{\mathrm{c}} - 5F_2^{\mathrm{c}}) \\
(V_{\mathrm{C}})_{22} &= \tfrac{1}{16}(11F_1^{\mathrm{d}} + 5F_2^{\mathrm{d}} - 7F_1^{\mathrm{c}} + 5F_2^{\mathrm{c}}) \\
(V_{\mathrm{C}})_{33} &= \tfrac{1}{16}(15F_1^{\mathrm{d}} + F_2^{\mathrm{d}} - 5F_1^{\mathrm{c}} - F_2^{\mathrm{c}}) \\
(V_{\mathrm{C}})_{12} &= 0 \\
(V_{\mathrm{C}})_{13} &= \tfrac{\sqrt{10}}{16}(F_1^{\mathrm{d}} - F_2^{\mathrm{d}} - 3F_1^{\mathrm{c}} + F_2^{\mathrm{c}}) \\
(V_{\mathrm{C}})_{23} &= 0\,,
\end{aligned} \tag{3.9}$$

with $F_1^{\mathrm{c}}, F_2^{\mathrm{c}}, F_1^{\mathrm{d}}, F_2^{\mathrm{d}}$ being free parameters to be determined in a fit. We ordered the channel indices by their respective thresholds, i.e. $1 : D_1\bar{D}, 2 : D_1\bar{D}^*$, and $3 : D_2\bar{D}^*$. The effect of the most prominent inelastic channels is included by adding an imaginary part to $F_1^{\mathrm{c}}, F_2^{\mathrm{c}}, F_1^{\mathrm{d}}, F_2^{\mathrm{d}}$ analogous to Refs.[139–141], however, no new parameters are introduced.

3.3.2. One-Pion Exchange

As discussed in section 1.4, the inclusion of the momentum-dependent width for the D_1 and D_2 makes it necessary to treat the one-pion exchange non-perturbative.

Furthermore, the study of the T_{cc} showed a significant influence of the one-pion exchange on the resulting pole position of the resonance.

The two contributions of the one-pion exchange in time-ordered perturbation theory as well as the chosen kinematics are shown in Fig.3.3 and Fig.3.2, respectively. The resulting potential for the different channels read:

$$\begin{aligned}
\bar{V}_{11}^{\text{OPE}} &= 0 \\
\bar{V}_{22}^{\text{OPE}} &= \left(\epsilon^*_{D_1}\right)^i_a \left(\epsilon^*_{\bar{D}^*}\right)^k_c O^{ij}_{1\,ab} O^{kl}_{1\,cd} \left(\epsilon_{D^*}\right)^j_b \left(\epsilon_{\bar{D}_1}\right)^l_d \left(\frac{1}{\mathcal{D}_{D^*,\bar{D}^*,\pi}(\vec{p},\vec{p}')} + \frac{1}{\mathcal{D}_{D_1,\bar{D}_1,\pi}(\vec{p},\vec{p}')}\right) \\
\bar{V}_{33}^{\text{OPE}} &= \left(\epsilon^*_{D_2}\right)^{ik}_a \left(\epsilon^*_{\bar{D}^*}\right)^m_c O^{ijk}_{3\,ab} O^{lmn}_{3\,cd} \left(\epsilon_{D^*}\right)^j_b \left(\epsilon_{\bar{D}_2}\right)^{ln}_d \left(\frac{1}{\mathcal{D}_{D^*,\bar{D}^*,\pi}(\vec{p},\vec{p}')} + \frac{1}{\mathcal{D}_{D_2,\bar{D}_2,\pi}(\vec{p},\vec{p}')}\right) \\
\bar{V}_{12}^{\text{OPE}} &= 0 \\
\bar{V}_{13}^{\text{OPE}} &= \left(\epsilon^*_{D_1}\right)^i_a O^{ij}_{1\,ab} O^{kl}_{2\,cd} \left(\epsilon_{D^*}\right)^j_b \left(\epsilon_{\bar{D}_2}\right)^{kl}_d \left(\frac{1}{\mathcal{D}_{D^*,\bar{D},\pi}(\vec{p},\vec{p}')} + \frac{1}{\mathcal{D}_{D_1,\bar{D}_2,\pi}(\vec{p},\vec{p}')}\right) \\
\bar{V}_{23}^{\text{OPE}} &= 0\,,
\end{aligned} \tag{3.10}$$

where we introduced the following abbreviations for the Lorentz structure of the vertex functions

$$\begin{aligned}
O^{ij}_{1\,ab} &= \frac{\tau_{ab}}{f_\pi}\sqrt{m_{D_1} m_{D^*}} \left[\sqrt{\frac{2}{3}} h'(3q^i q^j - \delta^{ij} q^2) - \frac{1}{\sqrt{6}} h'_s \omega_\pi \delta^{ij}\right] \\
O^{ij}_{2\,ab} &= i\frac{\tau_{ab}}{f_\pi}\sqrt{m_{D_2} m_D}\sqrt{2} h' q^i q^j \\
O^{ijk}_{3\,ab} &= -\frac{\tau_{ab}}{f_\pi}\sqrt{m_{D_2} m_{D^*}}\sqrt{2} i h' \epsilon^{ijl} q^l q^k\,.
\end{aligned} \tag{3.11}$$

The propagators are derived from time-ordered perturbation theory, resulting in

$$\mathcal{D}_{A,B,C}(p,p') = E - \sqrt{m_A^2 + p^2} - \sqrt{m_B^2 + p'^2} - \sqrt{m_C^2 + p^2 + p'^2 - 2pp'z} \tag{3.12}$$

for the denominator of the intermediate 3 meson system, where z denotes the cosine of the scattering angle between $\vec{p}$ and $\vec{p}'$. There is an additional set of OPE potentials once we consider vertices of the kind $\{D_1, D_2\} \to \{D_1, D_2\}\,\Phi$ as shown in Fig. 3.4. As the intermediate 3 body cut of both time-orderings contains a heavy $\{D_1, D_2\}$ field, they will go on-shell at significantly higher energies than those presented in Eq.(3.10). Furthermore, due to the width of the $\{D_1, D_2\}$, the corresponding pole of the propagator is shifted into the complex plane. However, if these kinds of diagrams are sub-leading can only be confirmed after the fitting, such that we additionally to

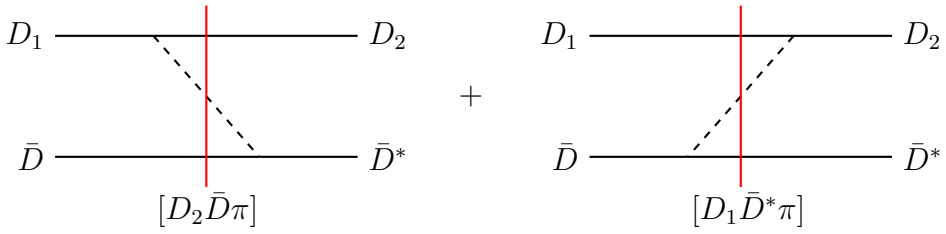

Figure 3.4.: Contribution $\tilde{V}_{13}$ to the one-pion exchange potential to $D_1\bar{D} \to D_2\bar{D}^*$. Both time-orderings contain a heavy $j_\ell^P = \frac{3}{2}^+$ field in the intermediate 3-body cut.

Eq (3.10) consider the contributions $\tilde{V}^{\text{OPE}}$ to the OPE potential

$$\begin{aligned}
\tilde{V}_{13}^{\text{OPE}} &= \left(\epsilon^*_{D_1}\right)^i_a O^{ijk}_{6\,ab} O^l_{4\,cd} \left(\epsilon_{D_2}\right)^{jk}_b \left(\epsilon_{\bar{D}^*}\right)^l_d \left(\frac{1}{\mathcal{D}_{D_2,\bar{D},\pi}(\vec{p},\vec{p}')} + \frac{1}{\mathcal{D}_{D_1,\bar{D}^*,\pi}(\vec{p},\vec{p}')}\right) \\
\tilde{V}_{33}^{\text{OPE}} &= \left(\epsilon^*_{D_2}\right)^{ij}_a \left(\epsilon^*_{\bar{D}^*}\right)^m_c O^{ijkl}_{7\,ab} O^{mn}_{5\,cd} \left(\epsilon_{D_2}\right)^{kl}_b \left(\epsilon_{\bar{D}^*}\right)^n_d \frac{2}{\mathcal{D}_{D_2,\bar{D}^*,\pi}(\vec{p},\vec{p}')} \,,
\end{aligned} \tag{3.13}$$

with the additional vertex functions

$$\begin{aligned}
O^i_{4\,ab} &= \frac{\sqrt{2} g \tau_{ab}}{f_\pi} p^i_\pi \sqrt{m^*_D m_D} \\
O^{ij}_{5\,ab} &= \frac{\sqrt{2} g \tau_{ab}}{f_\pi} p^k_\pi \epsilon^{ijk} m_{D^*} \\
O^{ijk}_{6\,ab} &= -i \frac{8 g_{3/2} \tau_{ab}}{\sqrt{3} f_\pi} \delta^{ik} p^j \sqrt{m_{D_1} m_{D_2}} \\
O^{ijkl}_{7\,ab} &= -\frac{\sqrt{2} g_{3/2} \tau_{ab}}{f_\pi} \delta^{ik} p^k \epsilon^{jkl} m_{D_2} \,.
\end{aligned} \tag{3.14}$$

Therefore, the full one-pion exchange potential is given by adding Eq. (3.10) and Eq. (3.13), i.e.

$$V_{ij}^{\text{OPE}} = \bar{V}_{ij}^{\text{OPE}} + \tilde{V}_{ij}^{\text{OPE}} \,. \tag{3.15}$$

The inclusion of the one-pion exchange only preserves HQSS if both S-waves and all relevant D-waves are considered [25]. In contrast to the partial wave projection in the $\pi\pi - \bar{K}K$ system, we need to generalize the formula in Eq. (2.31) to account for the spin of the D mesons. The partial wave projected OPE potentials can be calculated using the formulas of Refs. [145, 146],

$$V_{LL'}^{\text{OPE}}(p,p') = \frac{1}{2J+1} \int \frac{\mathrm{d}\Omega_p}{4\pi} \frac{\mathrm{d}\Omega_{p'}}{4\pi} \, \text{Tr}\left[P^\dagger(JLS;\vec{n}) V^{\text{OPE}}(\vec{p},\vec{p}') P(JL'S';\vec{n}')\right] \,, \tag{3.16}$$

where $\vec{n} = \vec{p}/p$ and $P(JLS, \vec{n})$ denotes a projection operator for the spin coupling. These projectors are normalized to

$$1 = \frac{1}{2J+1} \int \frac{\mathrm{d}\Omega_n}{4\pi} P^\dagger(\alpha, \vec{n}) P(\alpha, \vec{n}) \,. \tag{3.17}$$

A list of all relevant projectors considering the $j_\ell^P = \frac{1}{2}^-$ particles is listed in Ref. [141].

Note that it is not immediately obvious, that the amplitudes $\bar{V}_{23}^{\mathrm{OPE}}$ and $\tilde{V}_{13}^{\mathrm{OPE}}, \tilde{V}_{23}^{\mathrm{OPE}}$ vanish for the studied system. The Lorentz structure of the amplitude $\tilde{V}_{13}^{\mathrm{OPE}}$ for the transition $D_1\bar{D} \to D_1\bar{D}^*$ can be written as

$$\tilde{V}_{13}^{\mathrm{OPE}} \propto \epsilon_{D_1}^{*i}(\lambda) \epsilon^{ijk} p^j p^l \epsilon_{D_1}^j(\lambda_1') \epsilon_{D^*}^l(\lambda_2') \,, \tag{3.18}$$

where λ and λ_f' denote the incoming and outgoing polarizations, respectively. For a general J^{PC} this term does not vanish. However, once we consider the coupling of the final $D_1\bar{D}^*$ into e.g. the partial wave ${}^3S_1$ for $J^{PC} = 1^{--}$, where the projector is given by

$$P(D_1\bar{D}^*({}^3S_1))^j = \frac{i}{\sqrt{3}} \epsilon^{jkl} \epsilon_{D_1}^k \epsilon_{D^*}^l \,, \tag{3.19}$$

it follows

$$\tilde{V}_{13}^{\mathrm{OPE}} \propto \epsilon^{ijk} p^j p^l \epsilon^{jli'} = p^k p^l (\delta^{li}\delta^{ki'} - \delta^{kl}\delta^{ii'}) = p^i p^{i'} - p^2 \delta^{ii'} \,, \tag{3.20}$$

which is zero for an S-wave, as the initial and final polarization i and i' are the same. The same reasoning results in $\bar{V}_{23}^{\mathrm{OPE}} = 0$ and $\tilde{V}_{23}^{\mathrm{OPE}} = 0$.

3.4. Coupled-channel Lippman-Schwinger equation

With the full potential fixed by $V^{\mathrm{eff}} = V_{\mathrm{C}} + V_{\mathrm{OPE}}$, the coupled-channel Lippman-Schwinger equation for a system with definite J^{PC} is given by

$$T_{\alpha\beta}(E, p, p') = V_{\alpha,\beta}^{\mathrm{eff}}(\vec{p}, \vec{p}') - \sum_\gamma \int \frac{\mathrm{d}^3 q}{(2\pi)^3} V_{\alpha\gamma}^{\mathrm{eff}}(p, q) G_\gamma(q) T_{\gamma\beta}(q, p') \,, \tag{3.21}$$

where α, β, γ label the basis vectors for the different partial waves defined in Eq. (3.4). We now consider the momentum-dependent width of the D_1 and D_2 in the propagation G_γ of the multi-meson states. In Ref. [147], Faddeev describes a framework that extends the principles of two-body unitarity to the three-body case. In general, three particles can interact via two- or three-body forces. If we assume the interaction to be of finite range, it follows that beyond a certain distance away from the center of mass, the three-particle force drops to zero, although two-body forces may remain.

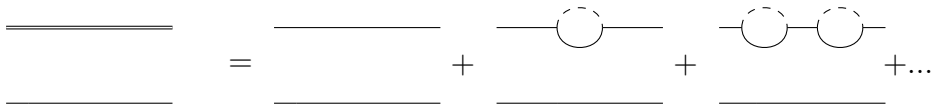

Figure 3.5.: Feynman diagrams for the dressed propagator of $D_1\bar{D}, D_1\bar{D}^*$ and $D_2\bar{D}^*$ on the left hand side given by the series of diagrams intermediate containing $D^{(*)}\pi$ loops.

These two-body systems might form resonances, while the third particle acts as an observer. In general, there are three so-called two-body fragmentation channels, where the two-body subsystem can be unitarized by standard Lippman-Schwinger equation

$$t_\alpha = V_\alpha + V_\alpha G_0 t_\alpha \,, \tag{3.22}$$

with alpha denoting the index of the corresponding two-body fragmentation channel. The full 3-body problem shown in Fig. 3.5 can not simply be resumed, as the kernel is disconnected. Faddeev derived a set of equations that reiterate the two-body t-matrices t_α into a connected Faddeev kernel, where the defining equation for the scattering channel $|\psi_1\rangle$ may be written as

$$\begin{pmatrix} |\psi_1\rangle \\ |\psi_2\rangle \\ |\psi_3\rangle \end{pmatrix} = \begin{pmatrix} |\phi_1\rangle \\ 0 \\ 0 \end{pmatrix} + G_0 \begin{pmatrix} 0 & t_1 & t_1 \\ t_2 & 0 & t_2 \\ t_3 & t_3 & 0 \end{pmatrix} \begin{pmatrix} |\psi_1\rangle \\ |\psi_2\rangle \\ |\psi_3\rangle \end{pmatrix} , \tag{3.23}$$

with $|\phi_1\rangle$ denoting the resonance wave function of channel 1.

For the present study, we consider the proper inclusion of D_1 and D_2, as the widths of D and D^* are neglectable. For e.g. the first channel $D_1\bar{D}$, the dominant contribution in the 3-body channel $D^*\bar{D}\pi$ is generated by the resonant $D^*\pi \to D_1$ interaction in the studied energy range. We do not explicitly parameterize the 3-body propagator G_0, but absorb it into V by considering the resonances of the two-body subsystems in the OPE of the potential. As a result, we can map the Faddeev equation onto the Lippmann-Schwinger equation given in Eq. (3.21), where the full unitarized three body propagator in time-ordered perturbation theory may be written as

$$G_\gamma = \frac{1}{E - \omega_{\gamma 1} - \omega_{\gamma 2} + i\Gamma_\gamma/2} \,. \tag{3.24}$$

Here $\Gamma_\gamma/2$ corresponds to the imaginary part of the intermediate loops, as shown in Fig. 3.5.

Inserting the spin-averaged matrix elements into Eq. (1.95) and Eq. (1.93) yields

$$\begin{aligned}\Gamma_{D_1} &= \frac{1}{3}\frac{\rho_{\pi D^*}(m_{D_1}^2)}{m_{D_1}}\left[\frac{h_s'^2\omega_\pi^2}{4{f_\pi}^2}m_{D_1}m_{D^*} + \frac{h'^2}{{f_\pi}^2}p_{D^*\pi}(m_{D_1})^4 m_{D_1}m_{D^*}\right]\\ \Gamma_{D_2} &= \frac{1}{5}\frac{\rho_{\pi D^*}(m_{D_2}^2)}{m_{D_2}}\frac{3h'^2}{{f_\pi}^2}p_{\pi D^*}(m_{D_2})^4 m_{D_2}m_{D^*} + \frac{1}{5}\frac{\rho_{\pi D}(m_{D_2}^2)}{m_{D_2}}\frac{2h'^2}{{f_\pi}^2}p_{\pi D}(m_{D_2})^4 m_{D_2}m_{D}\,,\end{aligned} \tag{3.25}$$

from which we can derive the energy dependent width generated for a given channel $\gamma = \{1, 2, 3\}$

$$\begin{aligned}\Gamma_1(E,l) &= \frac{p_{DD^*\pi}(E,l)}{24\pi m_{D_1}}\left[\frac{h_s'^2\omega_\pi(E,l)^2}{4{f_\pi}^2}m_{D^*} + \frac{h'^2}{{f_\pi}^2}p_{DD^*\pi}(E,l)^4 m_{D^*}\right]\\ \Gamma_2(E,l) &= \frac{p_{D^*D^*\pi}(E,l)}{24\pi m_{D_1}}\left[\frac{h_s'^2\omega_\pi(E,l)^2}{4{f_\pi}^2}m_{D^*} + \frac{h'^2}{{f_\pi}^2}p_{D^*D^*\pi}(E,l)^4 m_{D^*}\right]\\ \Gamma_3(E,l) &= \frac{1}{40\pi m_{D_2}}\left[\frac{3h'^2}{{f_\pi}^2}m_{D^*}p_{DD^*\pi}(E,l)^5 + \frac{2h'^2}{{f_\pi}^2}m_D p_{D^*D^*\pi}(E,l)^5\right].\end{aligned} \tag{3.26}$$

Here $q_{ABC}(E,l)$ denotes the center of mass momentum of the particles B and C embedded in the three body system of particles A, B, C

$$q_{ABC}(E,l) = \frac{\lambda^{1/2}(\omega_{BC}^2, m_B^2, m_C^2)}{2(\omega_{BC})} \quad \text{with} \quad \omega_{BC}^2 = \left(E - \sqrt{m_A^2 + l^2}\right)^2 - l^2\,. \tag{3.27}$$

4. Summary and outlook

In this thesis we presented a path towards a systematic analysis of the $J^{PC} = 1^{--}$ channels in the range from 4.2 to 4.5 GeV, building on the results of our study of the $Y(4230)$. We present insight into the exotic vector states $Y(4230)$ and $Z_c(3900)$ and demonstrate the issues arising from simple Breit-Wigner fits omitting the relevant threshold effects.

In our initial study, we simultaneously analyzed the lineshapes of seven hadronic final state cross sections and invariant mass distributions as well as data from $e^+e^- \to \mu^+\mu^-$ in the energy range from 4.2 to 4.35 GeV. We demonstrate that even with a single exotic state, it is possible to describe all those final states with consistent resonance parameters. This was made possible by including the effects of the $D_1\bar{D}$ channel as well as allowing for interference between the conventional charmonium state $\psi(4160)$ with the exotic $Y(4230)$. Furthermore, this is substantial in explaining the $\mu^+\mu^-$ lineshape, where the mixing of the two states constrained by the hadronic final states, is in fact consistent with the description of the leptonic final state. This may be interpreted as additional support for the scenario suggested in this thesis.

The inclusion of the intermediate $D_1\bar{D}$ is necessary if the $Y(4230)$ is a hadronic molecule formed in this channel. One of the implications of this scenario is the distortion of the lineshape near the $D_1\bar{D}$ threshold, which is especially prominent in the $D^0D^{*-}\pi^+$ and the $J/\psi\pi^+\pi^-$ cross sections. In contrast to the experimental analyses, which extract two states from the data for the $J/\psi\pi^+\pi^-$ channel, the molecular scenario presented here naturally explains the asymmetric lineshapes. Furthermore, we are able to describe the energy dependences of the cross sections for $e^+e^- \to J/\psi\pi^+\pi^-$ and $e^+e^- \to J/\psi K^+K^-$ simultaneously in line with the approximate SU(3) flavor symmetry of QCD, which is completely disregarded in the BESIII analysis. Our fits also reproduce the expected hierarchy in the production of conventional charmonium states in comparison to molecular states in e^+e^- collisions. The production of the $Y(4230)$ from a photon is suppressed in heavy quark effective theory, which is reflected in the individual contributions of the $Y(4230)$ and $\psi(4160)$ in $e^+e^- \to \mu^+\mu^-$, with the latter being significantly larger.

For the other two-body finals states, the lineshape of the $\chi_{c0}\omega$ total cross section emerges from the interference of the non-trivial energy dependence of the triangle diagram, which emerges from a non-trivial interplay of a triangle contribution

featuring the $D_1\bar{D}$ intermediate state with the $\psi(4160)$. In addition, our analysis allows us to describe the very different lineshapes of e.g. $J/\psi\eta$ and $X(3872)\gamma$ cross sections simultaneously via the interference of the $\psi(4160)$ and $Y(4230)$.

With the results of this exploratory study showing very promising results, we also present the next logical step with the inclusion of the spin partners $D_1\bar{D}^*$ and $D_2\bar{D}^*$ called for by HQSS. This will allow us to properly study the coupled channel dynamics via a Lippmann-Schwinger equation and extend the studied energy range significantly. With the inclusion of the $Z_c(4020)$, a candidate for a $D^*\bar{D}^*$ molecule, we can analyze the $h_c\pi$ invariant mass spectra. The study of the strange partners of the Z_c states, e.g. the $Z_{cs}(4000)$, allows us to probe the $J/\psi K^+K^-$ cross section and its subsystems in more detail. With the full coupled channel dynamics, we can also turn to the $\psi(2S)\pi^+\pi^-$ final state, which was the only channel omitted in our previous study of the $Y(4230)$. Since our analysis includes both hadronic and leptonic final states, we are in the position to disentangle the strong and electromagnetic coupling of the Y states. Thus we will also be able to improve the current limits and uncertainties on the corresponding branching fractions to the different final states.

In conclusion, the non-trivial insights gained in this thesis were only possible because we studied multiple final states simultaneously. This appears unavoidable to get access to reliable resonance parameters, as single-channel Breit-Wigner analyses tend to extract resonance parameters with large scatter as shown in Fig. 2.1.

A. The relativistic three-body phase space

The differential cross section for a scattering process of two initial into n-final particles is given by [4]

$$\mathrm{d}\sigma = \frac{(2\pi)^4}{4\sqrt{(k_1 \cdot k_2)^2 - m_1^2 m_2^2}} \left|\bar{\mathcal{M}}\right|^2 \mathrm{d}\Phi_n(k_1 + k_2; p_1, p_2, ..., p_n)\,, \tag{A.1}$$

where $\left|\bar{\mathcal{M}}\right|^2$ is the spin averaged matrix element squared and the factor in front the so-called initial flux. The the n-body phase space element is defined as

$$\mathrm{d}\Phi_n(P; p_1, p_2, ..., p_n) = \delta^4(P - \sum_{i=1}^{n} p_i) \prod_{i=1}^{n} \frac{\mathrm{d}^3 p_i}{(2\pi)^3 2\omega_i}\,, \tag{A.2}$$

with incoming $P = k_1 + k_2$ and outgoing p_i momenta. It can be decomposed recursively via

$$\mathrm{d}\Phi_n(P; p_1, ..., p_n) = \mathrm{d}\Phi_j(q; p_1, ..., p_j)\, \mathrm{d}\Phi_{n-j+1}(P, p_{j+1}, ..., p_n)\, \mathrm{d}q^2 (2\pi)^3\,. \tag{A.3}$$

In the following we explicitly derive the 3-body phase space element. For a more general review of the relativistic kinematics of particle reactions, we recommend Ref. [148]. Analogous to the Mandelstam variables in $2 \to 2$ scattering it is useful to define the invariant energies of the two-particle subsystems in a $1 \to 3$ decay

$$\begin{aligned} s_{12} = s_1 &= (p_1 + p_2)^2 = (P - p_3)^2 \\ s_{23} = s_2 &= (p_2 + p_3)^2 = (P - p_1)^2 \\ s_{13} = s_3 &= (p_1 + p_3)^2 = (P - p_2)^2\,, \end{aligned} \tag{A.4}$$

which further fulfill the relation

$$s_1 + s_2 + s_3 = s + \sum_i m_i^2\,. \tag{A.5}$$

A. The relativistic three-body phase space

In the center of mass of the decaying particle, the energies E_i^* and 3-momenta p_i^* of the final particles can be expressed

$$\begin{aligned} E_1^* &= \frac{s + m_1^2 - s_2}{2\sqrt{s}}, & p_1^* &= \frac{\lambda^{1/2}(s, m_1^2, s_2)}{2\sqrt{s}} \\ E_2^* &= \frac{s + m_2^2 - s_3}{2\sqrt{s}}, & p_2^* &= \frac{\lambda^{1/2}(s, m_2^2, s_3)}{2\sqrt{s}} \\ E_3^* &= \frac{s + m_3^2 - s_1}{2\sqrt{s}}, & p_3^* &= \frac{\lambda^{1/2}(s, m_3^2, s_1)}{2\sqrt{s}}\,. \end{aligned} \tag{A.6}$$

Following Eq. A.2 the three body phase space element Φ_3 is given by

$$\Phi_3(s) = \frac{1}{(2\pi)^9} \int \prod_{i=1}^{3} \frac{\mathrm{d}^3 p_i}{2\omega_i} \delta^4(P - p_1 - p_2 - p_3)\,, \tag{A.7}$$

where the δ function ensures energy and momentum conservation from the incoming 4-vector P decaying into p_i. Using the δ function to integrate over p_2 we obtain

$$\Phi_3(s) = \frac{1}{(2\pi)^9} \int \frac{\mathrm{d}^3 p_1\, \mathrm{d}^3 p_3}{8\omega_1\omega_2\omega_3} \delta(\sqrt{s} - \omega_1 - \omega_2 - \omega_3)\,. \tag{A.8}$$

Now we can rewrite the integrand

$$\begin{aligned} \mathrm{d}^3 p_1\, \mathrm{d}^3 p_3 =& p_1^2 \mathrm{d}p_1 \mathrm{d}\Omega_1 p_3^2 \mathrm{d}p_3 \mathrm{d}\Omega_3 \\ & p_1\omega_1 \mathrm{d}\omega_1 \mathrm{d}\Omega_1 p_3 \omega_3 \mathrm{d}\omega_3 \mathrm{d}\Omega_3\,, \end{aligned} \tag{A.9}$$

where $\Omega_3 = (\cos\theta_{13}, \phi_3)$ describes the orientation of the 3-momentum $\vec{p}_3$ with respect to $\vec{p}_1$. From the relation $E_2^2 = (p_1 + p_3)^2 + m_2^2 = p_1^2 + p_3^2 + 2p_1p_3\cos\theta_{13} + m_2^2$ we get

$$\frac{\mathrm{d}\omega_2}{\mathrm{d}\cos\theta_{13}} = \frac{p_1 p_3}{E_2}\,, \tag{A.10}$$

such that we can integrate over $\cos\theta_{13}$

$$\Phi_3(s) = \frac{1}{(2\pi)^9} \frac{1}{8} \int \mathrm{d}\omega_1 \mathrm{d}\omega_3 \mathrm{d}\Omega_1 \mathrm{d}\phi_3 \Theta(1 - \cos^2\theta_{13})\,, \tag{A.11}$$

where the heaviside function ensures physical values for θ_{13}. Here $\Omega_3 = (\cos\theta_{13}, \phi_3)$ describes the orientation of $\vec{p}_3$ with respect to $\vec{p}_1$, and Ω_1 the orientation of $\vec{p}_1$ with respect to some axis.
At last with the Jacobian

$$\frac{\partial\omega_1, \omega_3}{\partial s_1, s_3} = \frac{1}{4s}\,, \tag{A.12}$$

we get the final expression

$$\Phi_3(s) = \frac{1}{(2\pi)^9 32s} \int \mathrm{d}s_1 \, \mathrm{d}s_2 \, \mathrm{d}\Omega_1 \mathrm{d}\phi_3 \, . \tag{A.13}$$

In the center of mass frame of the decaying particle the two azimuthal integrations are trivial, yielding

$$\Phi_3 = \frac{1}{(2\pi)^7 32s} \int \mathrm{d}s_1 \, \mathrm{d}s_2 \, \mathrm{d}\theta_1 \, , \tag{A.14}$$

such that the total cross section is given by

$$\sigma = \frac{1}{4\sqrt{(k_1 \cdot k_2)^2 - m_1^2 m_2^2}} \, \frac{1}{(2\pi)^3 32s} \int \left|\bar{\mathcal{M}}\right|^2 \mathrm{d}s_1 \, \mathrm{d}s_2 \, \mathrm{d}\theta_1 \, . \tag{A.15}$$

The integration border of s_1 can be expressed in terms of s_2

$$s_1^{\pm} = m_1^2 + m_2^2 - \frac{1}{2s_2} \left[(s_2 - s + m_1^2)(s_2 + m_2^2 - m_3^2) \mp \lambda^{1/2}(s_2, s, m_1^2) \lambda^{1/2}(s_2, m_2^2, m_3^2) \right] \, . \tag{A.16}$$

Consequently, the borders of the s_2 integration are trivially given by

$$(m_2 + m_3)^2 \leq s_2 \leq (\sqrt{s} - m_1)^2 \, . \tag{A.17}$$

B. Numerical integration

In numerical analysis, quadrature rules allow to compute approximations of definite integrals. For a more complete review, we refer to Ref. [149]. A function $f(x)$ is evaluated at certain abscissas x_i with corresponding weights w_i, allowing us to write the integral as a sum

$$\int_a^b f(x) \approx \sum_i f(x_i) w_i \,. \tag{B.1}$$

In its simplest form, n equally spaced abscissas x_i are chosen in the interval $[a, b]$, such that a quadrature rule like the Newton-Cotes Formula is able to reproduce a polynomial of order n. As the goal is to obtain an integral as accurately as possible while keeping the number of evaluations of the integrand to a minimum, more complex algorithms were developed.

With Gaussian Quadrature one effectively doubles the reproducible degree of freedom by not only choosing the weights w_i but also the abscissas x_i, making use of orthogonal function systems. In this sense, higher order does only imply higher accuracy for very smooth analytic integrands. However, with a variable choice of the abscissas and weights we can effectively circumvent integrable singularities in the integrand, demonstrated later in this section.

In this thesis we rely on the Gauss-Legendre-Quadrature which is defined on the interval $[-1, 1]$ as

$$\int_{-1}^1 f(x) \approx \sum_i^n f(x_i) \omega_i \,, \tag{B.2}$$

where the nodes x_i are given by the roots n-th Legendre polynomial and the weights can be calculated via

$$\omega_i = \frac{2}{(1 - x_i^2)(P_n'(x_i))^2} \,. \tag{B.3}$$

This choice of abscissas and weights allows us to integrate polynomials of order $2n-1$ exactly. To adapt the integration range, we simply perform a linear mapping from $[-1, 1] \mapsto [a, b]$, resulting in

$$\int_a^b f(x) \approx \frac{b-a}{2} \sum_i f\left(\frac{(b-a)x_i + a + b}{2}\right) \omega_i \,. \tag{B.4}$$

B.1. Triangle topologies

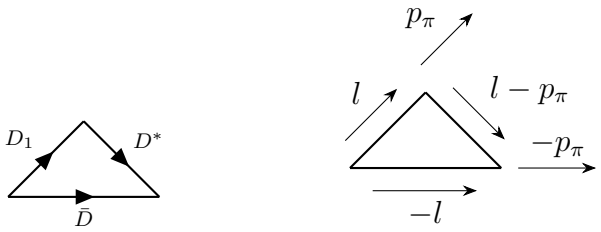

Figure B.1.: Momentum assignment of the triangle loop.

The triangle diagram shown in figure B.1 only has one time ordering, such that it can be expressed as

$$\mathcal{T}_{D_1 D D^*} = \int \frac{\mathrm{d}^3 l}{(2\pi)^3} \frac{1}{8\omega_D \omega_{D_1} \omega_{D^*}} \frac{1}{E - \omega_{D_1} - \omega_D} \frac{1}{E - \omega_\pi - \omega_{D^*} - \omega_D}\,, \tag{B.5}$$

with $\omega_i = \sqrt{m_i^2 + p_i^2}$

$$\begin{aligned} \omega_D &= \sqrt{m_D^2 + l^2} \\ \omega_{D^*} &= \sqrt{m_{D^*}^2 + l^2 + p_\pi^2 - 2 l p_\pi z} \\ \omega_{D_1} &= \sqrt{(m_{D_1} - i\Gamma_{D_1}/2)^2 + l^2} \\ \omega_\pi &= \sqrt{m_\pi^2 + p_\pi^2}\,. \end{aligned} \tag{B.6}$$

In the center of mass frame of the $Y(4230)$ one can choose the momenta in a way that only the D^* has an angular dependency, where $\vec{p_\pi} = p_\pi (0,0,1)^{\mathrm{T}}$, such that $z = \cos\theta$ denotes the cosine of the polar angle of the loop momentum $\vec{l}$. Due to the width of the D_1 only the last propagator in eq. (B.5) has poles on the real axis, as in comparison the D^* width is negligible small. We define

$$f(E, l) = \frac{l^2}{8\omega_D \omega_{D_1}} \frac{1}{E - \omega_{D_1} - \omega_D}\,, \tag{B.7}$$

such that f is regular in l. The integral can now be rewritten as

$$\mathcal{T}_{D_1 D D^*} = \frac{1}{(2\pi)^2} \int_0^\Lambda \mathrm{d}l f(E, l) \int_{-1}^1 \mathrm{d}z \frac{1}{\omega_{D^*}} \frac{1}{E - \omega_\pi - \omega_{D^*} - \omega_D}\,, \tag{B.8}$$

where the trivial integration over the loop momentums azimuthal angle is performed. Doing a variable transformation

$$\mathrm{d}\omega_{D^*} = \frac{l p_\pi}{\omega_{D^*}} \mathrm{d}z \,, \tag{B.9}$$

the angular integration becomes

$$\int_{-1}^{1} \mathrm{d}\omega_{D^*} \frac{1}{p_\pi l} \frac{1}{E - \omega_\pi - \omega_D^* - \omega_D} \,. \tag{B.10}$$

The inverse factor of l is canceled by $f(E,l)$, while p_π is canceled by the phase space integration.
With the relation

$$\frac{1}{x - x_0 \pm i\epsilon} = \mathcal{P}\left(\frac{1}{x - x_0}\right) \mp i\pi\delta(x - x_0) \,, \tag{B.11}$$

where $\mathcal{P}$ denotes the Cauchy principal value, Eq. (B.10) becomes

$$\begin{aligned} \frac{1}{E - \omega_\pi - \omega_{D^*} - \omega_D + i\epsilon} = &-\mathcal{P}\left(\frac{1}{\omega_{D^*} - (E - \omega_D - \omega_\pi)}\right) \\ &- i\pi\delta(\omega_{D^*} - (E - \omega_\pi - \omega_D)) \,. \end{aligned} \tag{B.12}$$

The δ function can be rewritten as

$$\delta(\omega_{D^*} - (E - \omega_\pi - \omega_D)) = \frac{\omega_{D^*}}{l p_\pi} \delta(z - z_0) \,, \tag{B.13}$$

with

$$z_0 = -\frac{l^2 + p_\pi^2 + m_{D^*}^2 - (E - \omega_\pi - \omega_D)^2}{2 l p_\pi} \,. \tag{B.14}$$

Now Eq. (B.8) takes the form

$$I = \frac{1}{(2\pi)^2} \int_0^\infty \mathrm{d}l \frac{f(E,l)}{l p_\pi} \int_{-1}^{1} \mathrm{d}z \left[-\mathcal{P}\left(\frac{1}{\omega_{D^*} - (E - \omega_\pi - \omega_D)}\right) - i\pi\delta(z - z_0) \right] , \tag{B.15}$$

with

$$\mathcal{P}\left(\int_{\omega_{D^*}(z=-1)}^{\omega_{D^*}(z=1)} \mathrm{d}\omega_{D^*} \frac{1}{\omega_{D^*} - (E - \omega_\pi - \omega_D)} \right) = \log\left[\frac{E - \omega_{D^*}|_{z=1} - \omega_\pi - \omega_D}{E - \omega_{D^*}|_{z=-1} - \omega_\pi - \omega_D} \right] . \tag{B.16}$$

Finally, we arrive at

$$I(E) = \int_0^\Lambda \mathrm{d}l \frac{\tilde{f}(E,l)}{p_\pi} \left[\log\left(\left| \frac{E - \omega_{D^*}|_{z=1} - \omega_\pi - \omega_D}{E - \omega_{D^*}|_{z=-1} - \omega_\pi - \omega_D} \right| \right) + i\pi\Theta\left(\frac{E - \omega_{D^*}|_{z=1} - \omega_\pi - \omega_D}{E - \omega_{D^*}|_{z=-1} - \omega_\pi - \omega_D} \right) \right] , \tag{B.17}$$

where the remaining radial integration can be performed numerically. In case of the $J/\psi D^{(*)}\bar{D}^{(*)}$ vertex, which scales with the loop-momentum itself, the integrand is modified accordingly

$$\mathcal{T}(C, \mathrm{Num}) = C \int \frac{\mathrm{d}^3 l}{2\pi^3} \frac{\mathrm{Num}(l, p_1, p_2)}{8\omega_1\omega_2\omega_3} G_1 G_2 \,, \tag{B.18}$$

with Num denoting the momentum factors in the numerator and C being a constant.

To decrease the number of sample points needed to achieve a stable result, it is useful to further split the l integration at the poles of the propagator, as the distribution of Gauss-Legendre sample points is more dense at the integration borders

$$\int_0^\Lambda \mathrm{d}l = \int_0^{l_0^\mathrm{P}} \int_{l_0^\mathrm{P}}^{l_1^\mathrm{P}} ... \int_{l_n^\mathrm{P}}^\Lambda \mathrm{d}l \,, \tag{B.19}$$

where the l_i^P correspond to the poles of the propagator in l, which can be calculated analytically for each propagator.

B.2. Box topologies

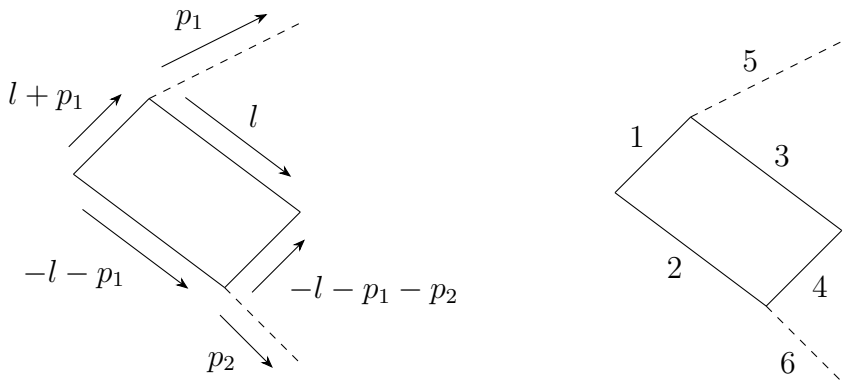

Figure B.2.: One time ordering of the first Feynman diagram shown in Fig. 2.11.

The Integral for the scalar box shown in figure B.2 is given by

$$I = \int \frac{\mathrm{d}^3 l}{(2\pi)^3} \frac{\mathrm{Num}(l, p_1, p_2)}{16\omega_1\omega_2\omega_3\omega_4} \frac{1}{E - \omega_1 - \omega_2} \frac{1}{E - \omega_5 - \omega_3 - \omega_2} \frac{1}{E - \omega_4 - \omega_3 - \omega_5 - \omega_6} \,. \tag{B.20}$$

In this work the second cut corresponds for most box topologies to $\bar{D}D^*\pi$, which can go on-shell. Analogous to the triangle we isolate the singularity and define the remaining part in a function $f(E, l, \varphi, z, p_1, p_2)$ that is regular in l and z. However, different to the triangle, it is not possible to to perform the integration of the polar angle analytically as f is also dependent on z, such that we perform a numerical subtraction

$$\begin{aligned} I &= \int \frac{\mathrm{d}^3 l}{(2\pi)^3} f(E, l, \varphi, z, p_1, p_2) \frac{1}{E - \omega_5 - \omega_3 - \omega_2} \\ &= \int_0^\Lambda \mathrm{d}l \; l^2 \int_0^{2\pi} \mathrm{d}\varphi \left[\int_{-1}^{1} \mathrm{d}z \, \frac{f(E, l, \varphi, z, p_1, p_2) - f(E, l, \varphi, z_0, p_1, p_2)}{E - \omega_5 - \omega_3 - \omega_2} \right. \\ &\qquad \left. + f(E, l, \varphi, z_0, p_1, p_2) \int_{-1}^{1} \mathrm{d}z \, \frac{1}{E - \omega_5 - \omega_3 - \omega_2} \right] , \end{aligned} \tag{B.21}$$

where z_0 is the pole of the propagator. The integration of the second summand con now be done analytically, resulting in

$$\int_{-1}^{1} \mathrm{d}z \, \frac{1}{E - \omega_5 - \omega_3 - \omega_2} = \log\left[\frac{(E - \omega_5 - \omega_3 - \omega_2)|_{z=1}}{(E - \omega_5 - \omega_3 - \omega_2)|_{z=-1}}\right] . \tag{B.22}$$

The remaining φ and l integration are performed numerically using Gauss-Legendre integration. Analogous to the triangle loops, one should split the integration at the integrable singularities in l to reduce the number of sample points needed. The general notation used in this work is

$$\mathcal{B}(C, \mathrm{Num}) = \sum_T C \int \frac{\mathrm{d}^3 l}{2\pi^3} \frac{\mathrm{Num}(l, p_1, p_2)}{16\omega_1\omega_2\omega_3\omega_4} G_1 G_2 G_3 \,, \tag{B.23}$$

where $\sum_T$ stands for the sum over the different time orderings and G_i denotes the propagators for the different cuts, e.g. $G_1 = 1/(E - w_{D_1} - \omega_D)$.

The input values given in table B.1 were used in the numerical calculations of this thesis.

Parameter	Value [MeV]
m_π^0	135
$m_\pi^\pm$	139.6
$m_K^\pm$	493.7
m_η	547.9
m_ω	782.7
m_D^0	1864.8
$m_D^\pm$	1869.7
m_D^{*0}	2006.9
$m_D^{*\pm}$	2010.3
m_{D_1}	2420.8
$m_{J/\psi}$	3096.9
$m_{\chi_{c0}}$	3414.7
m_{h_c}	3525.9
$m_{X(3872)}$	3871.7
$m_{\psi(4160)}$	4191
Γ_{D^*}	83.4×10^{-3}
Γ_{D_1}	31.7
$\Gamma_{\psi(4160)}$	70

Table B.1.: Input values for masses and widths used in this work, taken from the central value of the Review of Particle Physics by the Particle Data Group [51].

C. Remarks on the numerical evaluation of loops - Wigner rotation

The numerical integration of certain loop topologies can be quite demanding. A suitable choice of reference frame simplifies the calculation. In the center of mass frame for a $2 \to n$ scattering process there is one external angle as a degree of freedom. While it is possible to include this angle in the calculations explicitly, one can alternatively work in a certain reference frame for the decay tensor and subsequently rotate it around the initial (leptonic) tensor. We will focus on $2 \to 3$ scattering processes relevant for this work.
Following the convention of Ref. [150], we denote the transition amplitude in the aligned frame by $\mathcal{O}^{\nu}_{\{\lambda\}}$, with $\{\lambda\} = (\lambda_1, \lambda_2, \lambda_3)$ collecting the individual helicities of the three final state particles. In the aligned configuration, we choose one of the particles momenta $\vec{p}_1 = p_1(0, 0, 1)^{\mathrm{T}}$ to be oriented along the z axis. The amplitude $\mathcal{M}^{\Lambda}_{\lambda}$ in the space-fixed frame, where we fixed the spin projection Λ of the initial e^+e^- state along the z axis, may now be written as

$$\mathcal{M}^{\Lambda}_{\lambda} = \sum_{\nu} D^{J*}_{\Lambda,\nu}(\alpha, \beta, \gamma)\mathcal{O}^{\nu}_{\{\lambda\}}\,, \tag{C.1}$$

where $D^{J*}_{\Lambda,\nu}$ denotes the Wigner D-function for a $(2J+1)$-dimensional representation of the rotation group

$$D^{j}_{m'm}(\alpha, \beta, \gamma) = \langle jm'|e^{-i\alpha J_z}e^{-i\beta J_y}e^{-i\gamma J_z}|jm\rangle\,. \tag{C.2}$$

The vectors of the aligned configuration are first rotated around the z axis by γ, followed by a rotation around the y axis by β, and at last rotated around the z axis by α, into the space-fixed configuration. Here β and α denote the polar and azimuthal angles of the space-fixed p_1 momentum, respectively. The Wigner D-function is related to the spherical harmonics $Y^l_m(\theta, \phi)$ via

$$D^{l*}_{m,0}(\phi, \theta, 0) = \sqrt{\frac{4\pi}{2l+1}}Y^l_m(\theta, \phi) \tag{C.3}$$

and are by definition unitary

$$\sum_k D^j_{m'k}(R) D^{j*}_{km}(R) = \delta_{m'm} \,. \tag{C.4}$$

We can re-express the rotation matrix as given in Ref. [151] via

$$D^j_{m'm}(\alpha, \beta, \gamma) = e^{-im'\alpha} d^j_{m'm}(\beta) e^{-im\gamma} \,. \tag{C.5}$$

For our intention to reproduce the angular degree of freedom of the phase space integral in Eq. (A.14), we need to rotate around the polar angle β of $\vec{p}_1$. The relevant $d-$functions in spherical basis for total spin $j = 1$ are given in the appendix of Ref. [152]:

$$\begin{aligned} d^{(j=1)}_{11}(\beta) &= \frac{1}{2}(1 + \cos\beta) \\ d^{(j=1)}_{1-1}(\beta) &= \frac{1}{2}(1 - \cos\beta) \\ d^{(j=1)}_{01}(\beta) &= \frac{1}{\sqrt{2}} \sin\beta \\ d^{(j=1)}_{00}(\beta) &= \cos\beta \,, \end{aligned} \tag{C.6}$$

which fulfill the relations

$$\begin{aligned} d^j_{m'm}(\beta) &= (-1)^{m-m'} d^j_{-m'-m}(\beta) \\ d^j_{m'm}(\beta) &= (-1)^{m-m'} d^j_{mm'}(\beta) \,. \end{aligned} \tag{C.7}$$

With Eq.(C.6) and (C.7) we can express the rotation matrix in the spherical basis, i.e. $\chi^+ : m = 1, \chi^- : m = -1, \chi^0 : m = 0$, as

$$d^{(j=1)}_{m'm}(\beta) = \begin{pmatrix} d_{11}(\beta) & d_{1-1}(\beta) & d_{10}(\beta) \\ d_{-11}(\beta) & d_{-1-1}(\beta) & d_{-10}(\beta) \\ d_{01}(\beta) & d_{0-1}(\beta) & d_{00}(\beta) \end{pmatrix} = \begin{pmatrix} d_{11}(\beta) & d_{1-1}(\beta) & -d_{01}(\beta) \\ d_{1-1}(\beta) & d_{11}(\beta) & d_{01}(\beta) \\ d_{01}(\beta) & -d_{01}(\beta) & d_{00}(\beta) \end{pmatrix} , \tag{C.8}$$

which also must be unitary $\sum_k d_{m'k}(\beta) d^\dagger_{km}(\beta) = \delta_{m'm}$. As we are working in the Cartesian basis for the decay processes, we perform a basis transformation for the d-matrix. The spherical basis $\vec{\chi} = (\chi^+, \chi^-, \chi^0)^{\mathrm{T}}$ can be expressed in terms of the Cartesian basis $\vec{x} = (x, y, z)^{\mathrm{T}}$ via

$$\vec{\chi} = \begin{pmatrix} \chi^+ \\ \chi^- \\ \chi^0 \end{pmatrix} = \begin{pmatrix} -\frac{1}{\sqrt{2}}(x + iy) \\ \frac{1}{\sqrt{2}}(x - iy) \\ z \end{pmatrix} ,$$

such that

$$\vec{x} = T\vec{\chi} \quad \text{with} \quad T = \begin{pmatrix} -\frac{1}{\sqrt{2}} & \frac{1}{\sqrt{2}} & 0 \\ \frac{i}{\sqrt{2}} & \frac{i}{\sqrt{2}} & 0 \\ 0 & 0 & 1 \end{pmatrix} .$$

With $T = T_{\chi\to x}$ the basis transformation for a general rotation matrix R is simply given by

$$\begin{aligned} R_{\{\chi\}} &= T^{-1}_{\chi\to x} R_{\{x\}} T_{\chi\to x} \\ R_{\{x\}} &= T_{\chi\to x} R_{\{\chi\}} T^{-1}_{\chi\to x} \,. \end{aligned} \tag{C.9}$$

The spin averaged squared matrix element

$$|\bar{\mathcal{M}}|^2 = \sum_{\Lambda\Lambda'} L_{\Lambda,\Lambda'} \sum_{\{\lambda\}} \mathcal{M}^{*\,\Lambda}_{\{\lambda\}} \mathcal{M}^{\Lambda'}_{\{\lambda\}} \,, \tag{C.10}$$

may now be expressed in terms of

$$|\bar{\mathcal{M}}|^2 = \sum_{\Lambda\Lambda'} L_{\Lambda,\Lambda'} \sum_{\mu,\nu} R^*_{\Lambda\mu} R_{\Lambda'\nu} \sum_{\{\lambda\}} \mathcal{O}^{*\,\mu}_{\{\lambda\}} \mathcal{O}^{\nu}_{\{\lambda\}} \,. \tag{C.11}$$

In the context of this work, the spin density matrix $L_{\Lambda,\Lambda'}$ corresponds to the leptonic tensor discussed around Eq. (2.20). As we are working in the Cartesian basis, the rotation matrix is given by $R = T_{\chi\to x} d^{(j=1)}(\beta) T^{-1}_{\chi\to x}$. Depending on the chosen reference frame, the amplitudes $\mathcal{O}^{\mu}$ correspond to the decay amplitudes presented in section 2.5. In this work the, this formalism was mostly used for the $J/\psi\pi^+\pi^-$ final state presented in section 2.5.2. Due to the numerous loop topoliges, it was easier to define the amplitude in the aligned frame, and subsequently rotate them according to Eq. (C.11).

Bibliography

[1] S. L. Glashow. "Partial Symmetries of Weak Interactions".
In: *Nucl. Phys.* 22 (1961), pp. 579–588.
DOI: 10.1016/0029-5582(61)90469-2.

[2] S. Weinberg. "A Model of Leptons".
In: *Phys. Rev. Lett.* 19 (1967), pp. 1264–1266.
DOI: 10.1103/PhysRevLett.19.1264.

[3] H. Fritzsch, M. Gell-Mann, and H. Leutwyler.
"Advantages of the Color Octet Gluon Picture".
In: *Phys. Lett. B* 47 (1973), pp. 365–368.
DOI: 10.1016/0370-2693(73)90625-4.

[4] R. L. Workman et al. "Review of Particle Physics".
In: *PTEP* 2022 (2022), p. 083C01. DOI: 10.1093/ptep/ptac097.

[5] P. W. Higgs. "Broken Symmetries and the Masses of Gauge Bosons".
In: *Phys. Rev. Lett.* 13 (1964). Ed. by J. C. Taylor, pp. 508–509.
DOI: 10.1103/PhysRevLett.13.508.

[6] Z. Maki, M. Nakagawa, and S. Sakata.
"Remarks on the unified model of elementary particles".
In: *Prog. Theor. Phys.* 28 (1962), pp. 870–880. DOI: 10.1143/PTP.28.870.

[7] D. J. Gross and F. Wilczek. "Asymptotically Free Gauge Theories - I".
In: *Phys. Rev. D* 8 (1973), pp. 3633–3652. DOI: 10.1103/PhysRevD.8.3633.

[8] M. D. Schwartz. *Quantum Field Theory and the Standard Model*.
Cambridge University Press, Mar. 2014.
ISBN: 978-1-107-03473-0, 978-1-107-03473-0.

[9] K. Ottnad et al. "New insights into the neutron electric dipole moment".
In: *Phys. Lett. B* 687 (2010), pp. 42–47.
DOI: 10.1016/j.physletb.2010.03.005. arXiv: 0911.3981 [hep-ph].

[10] S. Weinberg. "Phenomenological Lagrangians".
In: *Physica A* 96.1-2 (1979). Ed. by S. Deser, pp. 327–340.
DOI: 10.1016/0378-4371(79)90223-1.

[11] A. Manohar and H. Georgi.
"Chiral Quarks and the Nonrelativistic Quark Model".
In: *Nucl. Phys. B* 234 (1984), pp. 189–212.
DOI: 10.1016/0550-3213(84)90231-1.

[12] J. Gasser and H. Leutwyler.
"Chiral Perturbation Theory: Expansions in the Mass of the Strange Quark".
In: *Nucl. Phys. B* 250 (1985), pp. 465–516.
DOI: 10.1016/0550-3213(85)90492-4.

[13] U. G. Meissner. "Low-Energy Hadron Physics from Effective Chiral Lagrangians with Vector Mesons". In: *Phys. Rept.* 161 (1988), p. 213.
DOI: 10.1016/0370-1573(88)90090-7.

[14] V. Bernard, N. Kaiser, and U.-G. Meissner.
"Chiral dynamics in nucleons and nuclei".
In: *Int. J. Mod. Phys. E* 4 (1995), pp. 193–346.
DOI: 10.1142/S0218301395000092. arXiv: hep-ph/9501384.

[15] S. Scherer. "Introduction to chiral perturbation theory".
In: *Adv. Nucl. Phys.* 27 (2003). Ed. by J. W. Negele and E. W. Vogt, p. 277.
arXiv: hep-ph/0210398.

[16] M. D. Schwartz. *Quantum Field Theory and the Standard Model*.
Cambridge University Press, Mar. 2014.
ISBN: 978-1-107-03473-0, 978-1-107-03473-0.

[17] N. Isgur and M. B. Wise.
"Weak Decays of Heavy Mesons in the Static Quark Approximation".
In: *Phys. Lett. B* 232 (1989), pp. 113–117.
DOI: 10.1016/0370-2693(89)90566-2.

[18] H. Georgi. "An Effective Field Theory for Heavy Quarks at Low-energies".
In: *Phys. Lett. B* 240 (1990), pp. 447–450.
DOI: 10.1016/0370-2693(90)91128-X.

[19] M. B. Wise.
"Chiral perturbation theory for hadrons containing a heavy quark".
In: *Phys. Rev. D* 45.7 (1992), R2188. DOI: 10.1103/PhysRevD.45.R2188.

[20] M. Neubert. *Heavy-Quark Effective Theory*. Oct. 1996.

[21] J. S. Bell and R. Jackiw. "A PCAC puzzle: $\pi^0 \to \gamma\gamma$ in the σ model".
In: *Nuovo Cim. A* 60 (1969), pp. 47–61. DOI: 10.1007/BF02823296.

[22] C. Vafa and E. Witten.
"Restrictions on symmetry breaking in vector-like gauge theories".
In: *Nuclear Physics B* 234.1 (1984), pp. 173–188. ISSN: 0550-3213.
DOI: https://doi.org/10.1016/0550-3213(84)90230-X. URL: https://www.sciencedirect.com/science/article/pii/055032138490230X.

[23] M. Gell-Mann, R. J. Oakes, and B. Renner.
"Behavior of current divergences under SU(3) x SU(3)".
In: *Phys. Rev.* 175 (1968), pp. 2195–2199. DOI: 10.1103/PhysRev.175.2195.

[24] A. F. Falk, B. Grinstein, and M. E. Luke.
"Leading mass corrections to the heavy quark effective theory".
In: *Nucl. Phys. B* 357 (1991), pp. 185–207.
DOI: 10.1016/0550-3213(91)90464-9.

[25] F.-K. Guo et al. "Hadronic molecules".
In: *Rev. Mod. Phys.* 90.1 (2018), p. 015004.
DOI: 10.1103/RevModPhys.90.015004. arXiv: 1705.00141 [hep-ph].

[26] N. Brambilla et al.
"The XYZ states: experimental and theoretical status and perspectives".
In: *Phys. Rept.* 873 (2020), pp. 1–154.
DOI: 10.1016/j.physrep.2020.05.001. arXiv: 1907.07583 [hep-ex].

[27] M. Mai, U.-G. Meißner, and C. Urbach.
"Towards a theory of hadron resonances".
In: *Phys. Rept.* 1001 (2023), pp. 1–66.
DOI: 10.1016/j.physrep.2022.11.005. arXiv: 2206.01477 [hep-ph].

[28] J. R. Peláez. "From controversy to precision on the sigma meson: A review on the status of the non-ordinary f0(500) resonance". In: *Physics Reports* 658 (2016). From controversy to precision on the sigma meson: A review on the status of the non-ordinary f0(500) resonance, pp. 1–111. ISSN: 0370-1573.
DOI: https://doi.org/10.1016/j.physrep.2016.09.001. URL: https://www.sciencedirect.com/science/article/pii/S0370157316302952.

[29] S. Coleman. *Aspects of Symmetry: Selected Erice Lectures*.
Cambridge University Press, 1985.

[30] S. Weinberg. "Elementary Particle Theory of Composite Particles".
In: *Phys. Rev.* 130 (2 Apr. 1963), pp. 776–783.
DOI: 10.1103/PhysRev.130.776.
URL: https://link.aps.org/doi/10.1103/PhysRev.130.776.

[31] S. Weinberg. "Evidence That the Deuteron Is Not an Elementary Particle".
In: *Phys. Rev.* 137 (1965), B672–B678. DOI: 10.1103/PhysRev.137.B672.

[32] V. Baru et al.
"Evidence that the a0(980) and f0(980) are not elementary particles".
In: *Physics Letters B* 586.1–2 (Apr. 2004), pp. 53–61. ISSN: 0370-2693.
DOI: 10.1016/j.physletb.2004.01.088.
URL: http://dx.doi.org/10.1016/j.physletb.2004.01.088.

[33] I. Matuschek et al.
"On the nature of near-threshold bound and virtual states".
In: *Eur. Phys. J. A* 57.3 (2021), p. 101.
DOI: 10.1140/epja/s10050-021-00413-y. arXiv: 2007.05329 [hep-ph].

[34] S. Weinberg. "Quasiparticles and the Born Series".
In: *Phys. Rev.* 131 (1 July 1963), pp. 440–460.
DOI: 10.1103/PhysRev.131.440.
URL: https://link.aps.org/doi/10.1103/PhysRev.131.440.

[35] S. Weinberg. "Elementary particle theory of composite particles".
In: *Phys. Rev.* 130 (1963), pp. 776–783. DOI: 10.1103/PhysRev.130.776.

[36] C. Hanhart, Y. S. Kalashnikova, and A. V. Nefediev.
"Lineshapes for composite particles with unstable constituents".
In: *Phys. Rev. D* 81 (2010), p. 094028. DOI: 10.1103/PhysRevD.81.094028.
arXiv: 1002.4097 [hep-ph].

[37] T. Hyodo. "Structure of Near-Threshold¡mml:math
xmlns:mml="http://www.w3.org/1998/Math/MathML"
display="inline"¿¡mml:mi¿s¡/mml:mi¿¡/mml:math¿-Wave Resonances".
In: *Physical Review Letters* 111.13 (Sept. 2013). ISSN: 1079-7114.
DOI: 10.1103/physrevlett.111.132002.
URL: http://dx.doi.org/10.1103/PhysRevLett.111.132002.

[38] V. Baru et al. "Interplay of quark and meson degrees of freedom in a
near-threshold resonance".
In: *The European Physical Journal A* 44.1 (Feb. 2010), pp. 93–103.
ISSN: 1434-601X. DOI: 10.1140/epja/i2010-10929-7.
URL: http://dx.doi.org/10.1140/epja/i2010-10929-7.

[39] E. Braaten and M. Lu. "Line shapes of the X(3872)".
In: *Phys. Rev. D* 76 (2007), p. 094028. DOI: 10.1103/PhysRevD.76.094028.
arXiv: 0709.2697 [hep-ph].

[40] D. B. Kaplan, M. J. Savage, and M. B. Wise.
"A New expansion for nucleon-nucleon interactions".
In: *Phys. Lett. B* 424 (1998), pp. 390–396.
DOI: 10.1016/S0370-2693(98)00210-X. arXiv: nucl-th/9801034.

[41] S. Fleming et al. “Pion interactions in the $X(3872)$”.
In: *Phys. Rev. D* 76 (2007), p. 034006. DOI: 10.1103/PhysRevD.76.034006.
arXiv: hep-ph/0703168.

[42] S. Weinberg. “Effective Gauge Theories”.
In: *Phys. Lett. B* 91 (1980), pp. 51–55.
DOI: 10.1016/0370-2693(80)90660-7.

[43] E. Epelbaum, H.-W. Hammer, and U.-G. Meissner.
“Modern Theory of Nuclear Forces”.
In: *Rev. Mod. Phys.* 81 (2009), pp. 1773–1825.
DOI: 10.1103/RevModPhys.81.1773. arXiv: 0811.1338 [nucl-th].

[44] R. Aaron, R. D. Amado, and J. E. Young.
“Relativistic Three-Body Theory with Applications to $\pi - N$ Scattering”.
In: *Phys. Rev.* 174 (5 Oct. 1968), pp. 2022–2032.
DOI: 10.1103/PhysRev.174.2022.
URL: https://link.aps.org/doi/10.1103/PhysRev.174.2022.

[45] M.-L. Du et al.
“Coupled-channel approach to Tcc+ including three-body effects”.
In: *Phys. Rev. D* 105.1 (2022), p. 014024.
DOI: 10.1103/PhysRevD.105.014024. arXiv: 2110.13765 [hep-ph].

[46] R. Casalbuoni et al.
“Hadronic transitions among quarkonium states in a soft exchange approximation. Chiral breaking and spin symmetry breaking processes”.
In: *Phys. Lett. B* 309 (1993), pp. 163–173.
DOI: 10.1016/0370-2693(93)91521-N. arXiv: hep-ph/9304280.

[47] S. R. Coleman, J. Wess, and B. Zumino.
“Structure of phenomenological Lagrangians. 1.”
In: *Phys. Rev.* 177 (1969), pp. 2239–2247. DOI: 10.1103/PhysRev.177.2239.

[48] B. Grinstein et al.
“Chiral perturbation theory for f D(s) / f D and B B(s) / B B”.
In: *Nucl. Phys. B* 380 (1992), pp. 369–376.
DOI: 10.1016/0550-3213(92)90248-A. arXiv: hep-ph/9204207.

[49] A. F. Falk and M. E. Luke.
“Strong decays of excited heavy mesons in chiral perturbation theory”.
In: *Phys. Lett. B* 292 (1992), pp. 119–127.
DOI: 10.1016/0370-2693(92)90618-E. arXiv: hep-ph/9206241.

[50] P. Colangelo, F. De Fazio, and R. Ferrandes. "Bounding effective parameters in the chiral Lagrangian for excited heavy mesons".
In: *Phys. Lett. B* 634 (2006), pp. 235–239.
DOI: 10.1016/j.physletb.2006.01.021. arXiv: hep-ph/0511317.

[51] R. L. Workman et al. "Review of Particle Physics".
In: *PTEP* 2022 (2022), p. 083C01. DOI: 10.1093/ptep/ptac097.

[52] V. Baru et al. "Double-J/ψ system in the spotlight of recent LHCb data".
In: *SciPost Phys. Proc.* 6 (2022), p. 007.
DOI: 10.21468/SciPostPhysProc.6.007.

[53] F. Bernardoni et al.
"Precision lattice QCD computation of the $B^*B\pi$ coupling".
In: *Phys. Lett. B* 740 (2015), pp. 278–284.
DOI: 10.1016/j.physletb.2014.11.051. arXiv: 1404.6951 [hep-lat].

[54] F.-K. Guo. "Triangle Singularities and Charmonium-like XYZ States".
In: *Nucl. Phys. Rev.* 37.3 (2020), pp. 406–413.
DOI: 10.11804/NuclPhysRev.37.2019CNPC52.
arXiv: 2001.05884 [hep-ph].

[55] P. Colangelo, F. De Fazio, and T. N. Pham. "Nonfactorizable contributions in B decays to charmonium: The Case of B- —> K- h(c)".
In: *Phys. Rev. D* 69 (2004), p. 054023. DOI: 10.1103/PhysRevD.69.054023.
arXiv: hep-ph/0310084.

[56] F.-K. Guo et al. "Effect of charmed meson loops on charmonium transitions".
In: *Phys. Rev. D* 83 (2011), p. 034013. DOI: 10.1103/PhysRevD.83.034013.
arXiv: 1008.3632 [hep-ph].

[57] P. Colangelo, F. De Fazio, and T. N. Pham.
"B- —> K- (chi(c0)) decay from charmed meson rescattering".
In: *Phys. Lett. B* 542 (2002), pp. 71–79.
DOI: 10.1016/S0370-2693(02)02306-7. arXiv: hep-ph/0207061.

[58] J. F. Donoghue. "Dispersion relations and effective field theory".
In: *Advanced School on Effective Theories*. June 1996.
arXiv: hep-ph/9607351.

[59] K. M. Watson. "Some general relations between the photoproduction and scattering of pi mesons". In: *Phys. Rev.* 95 (1954), pp. 228–236.
DOI: 10.1103/PhysRev.95.228.

[60] R. Omnes. "On the Solution of certain singular integral equations of quantum field theory". In: *Nuovo Cim.* 8 (1958), pp. 316–326.
DOI: 10.1007/BF02747746.

[61] L. von Detten et al. “How many vector charmonium(-like) states sit in the energy range from 4.2 to 4.35 GeV?” In: (Feb. 2024). arXiv: 2402.03057 [hep-ph].

[62] R. F. Lebed, R. E. Mitchell, and E. S. Swanson. “Heavy-Quark QCD Exotica”. In: *Prog. Part. Nucl. Phys.* 93 (2017), pp. 143–194. DOI: 10.1016/j.ppnp.2016.11.003. arXiv: 1610.04528 [hep-ph].

[63] A. Esposito, A. Pilloni, and A. D. Polosa. “Multiquark Resonances”. In: *Phys. Rept.* 668 (2017), pp. 1–97. DOI: 10.1016/j.physrep.2016.11.002. arXiv: 1611.07920 [hep-ph].

[64] S. L. Olsen, T. Skwarnicki, and D. Zieminska. “Nonstandard heavy mesons and baryons: Experimental evidence”. In: *Rev. Mod. Phys.* 90.1 (2018), p. 015003. DOI: 10.1103/RevModPhys.90.015003. arXiv: 1708.04012 [hep-ph].

[65] H.-X. Chen et al. “An updated review of the new hadron states”. In: *Rept. Prog. Phys.* 86.2 (2023), p. 026201. DOI: 10.1088/1361-6633/aca3b6. arXiv: 2204.02649 [hep-ph].

[66] M. Ablikim et al. “Precise measurement of the $e^+e^- \to \pi^+\pi^- J/\psi$ cross section at center-of-mass energies from 3.77 to 4.60 GeV”. In: *Phys. Rev. Lett.* 118.9 (2017), p. 092001. DOI: 10.1103/PhysRevLett.118.092001. arXiv: 1611.01317 [hep-ex].

[67] M. Ablikim et al. “Study of the resonance structures in the process $e^+e^+ \to \pi^+\pi^- J/\psi$”. In: *Phys. Rev. D* 106.7 (2022), p. 072001. DOI: 10.1103/PhysRevD.106.072001. arXiv: 2206.08554 [hep-ex].

[68] M. Ablikim et al. “Study of the process $e^+e^- \to \pi^0\pi^0 J/\psi$ and neutral charmonium-like state $Z_c(3900)^0$”. In: *Phys. Rev. D* 102.1 (2020), p. 012009. DOI: 10.1103/PhysRevD.102.012009. arXiv: 2004.13788 [hep-ex].

[69] M. Ablikim et al. “Observation of the $Y(4220)$ and $Y(4360)$ in the process $e^+e^- \to \eta J/\psi$”. In: *Phys. Rev. D* 102.3 (2020), p. 031101. DOI: 10.1103/PhysRevD.102.031101. arXiv: 2003.03705 [hep-ex].

[70] M. Ablikim et al. “Cross section measurements of $e^+e^- \to \omega\chi_{c0}$ form $\sqrt{s} =$ 4.178 to 4.278 GeV”. In: *Phys. Rev. D* 99.9 (2019), p. 091103. DOI: 10.1103/PhysRevD.99.091103. arXiv: 1903.02359 [hep-ex].

[71] M. Ablikim et al. "Evidence of a resonant structure in the $e^+e^- \to \pi^+ D^0 D^{*-}$ cross section between 4.05 and 4.60 GeV".
In: *Phys. Rev. Lett.* 122.10 (2019), p. 102002.
DOI: 10.1103/PhysRevLett.122.102002. arXiv: 1808.02847 [hep-ex].

[72] M. Ablikim et al.
"Study of $e^+e^- \to \gamma\omega J/\psi$ and Observation of $X(3872) \to \omega J/\psi$".
In: *Phys. Rev. Lett.* 122.23 (2019), p. 232002.
DOI: 10.1103/PhysRevLett.122.232002. arXiv: 1903.04695 [hep-ex].

[73] M. Ablikim et al.
"Evidence of Two Resonant Structures in $e^+e^- \to \pi^+\pi^- h_c$".
In: *Phys. Rev. Lett.* 118.9 (2017), p. 092002.
DOI: 10.1103/PhysRevLett.118.092002. arXiv: 1610.07044 [hep-ex].

[74] "Measurement of cross sections for $e^+e^- \to \mu^+\mu^-$ at center-of-mass energies from 3.80 to 4.60 GeV". In: *Phys. Rev. D* 102 (2020), p. 112009.
DOI: 10.1103/PhysRevD.102.112009. arXiv: 2007.12872 [hep-ex].

[75] M. Ablikim et al. "Cross section measurement of $e^+e^- \to \pi^+\pi^-(3686)$ from $\sqrt{S} = 4.0076$ to 4.6984 GeV". In: *Phys. Rev. D* 104.5 (2021), p. 052012.
DOI: 10.1103/PhysRevD.104.052012. arXiv: 2107.09210 [hep-ex].

[76] M. Ablikim et al. "Observation of the Y(4230) and a new structure in *".
In: *Chin. Phys. C* 46.11 (2022), p. 111002.
DOI: 10.1088/1674-1137/ac945c. arXiv: 2204.07800 [hep-ex].

[77] J. P. Lees et al. "Study of the reaction $e^+e^- \to \psi(2S)\pi^-\pi^-$ via initial-state radiation at BaBar". In: *Phys. Rev. D* 89.11 (2014), p. 111103.
DOI: 10.1103/PhysRevD.89.111103. arXiv: 1211.6271 [hep-ex].

[78] X. L. Wang et al.
"Measurement of $e^+e^- \to \pi^+\pi^-\psi(2S)$ via Initial State Radiation at Belle".
In: *Phys. Rev. D* 91 (2015), p. 112007. DOI: 10.1103/PhysRevD.91.112007.
arXiv: 1410.7641 [hep-ex].

[79] G.-J. Ding.
"Are Y(4260) and Z+(2) are D(1) D or D(0) D* Hadronic Molecules?"
In: *Phys. Rev. D* 79 (2009), p. 014001. DOI: 10.1103/PhysRevD.79.014001.
arXiv: 0809.4818 [hep-ph].

[80] Q. Wang, C. Hanhart, and Q. Zhao.
"Decoding the riddle of $Y(4260)$ and $Z_c(3900)$".
In: *Phys. Rev. Lett.* 111.13 (2013), p. 132003.
DOI: 10.1103/PhysRevLett.111.132003. arXiv: 1303.6355 [hep-ph].

[81] S. Dubynskiy and M. B. Voloshin. "Hadro-Charmonium".
In: *Phys. Lett. B* 666 (2008), pp. 344–346.
DOI: 10.1016/j.physletb.2008.07.086. arXiv: 0803.2224 [hep-ph].

[82] Q. Wang et al.
"Y(4260): hadronic molecule versus hadro-charmonium interpretation".
In: *Phys. Rev. D* 89.3 (2014), p. 034001.
DOI: 10.1103/PhysRevD.89.034001. arXiv: 1309.4303 [hep-ph].

[83] X. Li and M. B. Voloshin.
"$Y(4260)$ and $Y(4360)$ as mixed hadrocharmonium".
In: *Mod. Phys. Lett. A* 29.12 (2014), p. 1450060.
DOI: 10.1142/S0217732314500606. arXiv: 1309.1681 [hep-ph].

[84] M. Cleven et al. "Employing spin symmetry to disentangle different models for the XYZ states". In: *Phys. Rev. D* 92.1 (2015), p. 014005.
DOI: 10.1103/PhysRevD.92.014005. arXiv: 1505.01771 [hep-ph].

[85] F. E. Close and P. R. Page.
"Gluonic charmonium resonances at BaBar and BELLE?"
In: *Phys. Lett. B* 628 (2005), pp. 215–222.
DOI: 10.1016/j.physletb.2005.09.016. arXiv: hep-ph/0507199.

[86] E. Kou and O. Pene.
"Suppressed decay into open charm for the Y(4260) being an hybrid".
In: *Phys. Lett. B* 631 (2005), pp. 164–169.
DOI: 10.1016/j.physletb.2005.09.013. arXiv: hep-ph/0507119.

[87] Y. S. Kalashnikova and A. V. Nefediev.
"Spectra and decays of hybrid charmonia".
In: *Phys. Rev. D* 77 (2008), p. 054025. DOI: 10.1103/PhysRevD.77.054025.
arXiv: 0801.2036 [hep-ph].

[88] M. Berwein et al.
"Quarkonium Hybrids with Nonrelativistic Effective Field Theories".
In: *Phys. Rev. D* 92.11 (2015), p. 114019.
DOI: 10.1103/PhysRevD.92.114019. arXiv: 1510.04299 [hep-ph].

[89] N. Brambilla et al. "Heavy hybrid decays to quarkonia".
In: *Phys. Rev. D* 107.5 (2023), p. 054034.
DOI: 10.1103/PhysRevD.107.054034. arXiv: 2212.09187 [hep-ph].

[90] A. Ali et al.
"A new look at the Y tetraquarks and Ω_c baryons in the diquark model".
In: *Eur. Phys. J. C* 78.1 (2018), p. 29.
DOI: 10.1140/epjc/s10052-017-5501-6. arXiv: 1708.04650 [hep-ph].

[91] T. Bhavsar et al. "Masses of tetraquark states in the hidden charm sector above $D - D^*$ threshold". In: *Nucl. Phys. A* 1000 (2020), p. 121856. DOI: 10.1016/j.nuclphysa.2020.121856. arXiv: 2002.06363 [hep-ph].

[92] R. F. Lebed. "Spectroscopy of Exotic Hadrons Formed from Dynamical Diquarks". In: *Phys. Rev. D* 96.11 (2017), p. 116003. DOI: 10.1103/PhysRevD.96.116003. arXiv: 1709.06097 [hep-ph].

[93] S. Coito and F. Giacosa. "On the Origin of the $Y(4260)$". In: *Acta Phys. Polon. B* 51.8 (2020), pp. 1713–1737. DOI: 10.5506/APhysPolB.51.1713. arXiv: 1902.09268 [hep-ph].

[94] D.-Y. Chen et al. "Unified Fano-like interference picture for charmoniumlike states Y(4008), Y(4260) and Y(4360)". In: *Phys. Rev. D* 93 (2016), p. 014011. DOI: 10.1103/PhysRevD.93.014011. arXiv: 1512.04157 [hep-ph].

[95] M. Cleven et al. "$Y(4260)$ as the first S-wave open charm vector molecular state?" In: *Phys. Rev. D* 90.7 (2014), p. 074039. DOI: 10.1103/PhysRevD.90.074039. arXiv: 1310.2190 [hep-ph].

[96] W. Qin, S.-R. Xue, and Q. Zhao. "Production of $Y(4260)$ as a hadronic molecule state of $\bar{D}D_1 + c.c.$ in e^+e^- annihilations". In: *Phys. Rev. D* 94.5 (2016), p. 054035. DOI: 10.1103/PhysRevD.94.054035. arXiv: 1605.02407 [hep-ph].

[97] Y.-H. Chen et al. "Effect of Z_b states on $\Upsilon(3S) \to \Upsilon(1S)\pi\pi$ decays". In: *Phys. Rev. D* 93.3 (2016), p. 034030. DOI: 10.1103/PhysRevD.93.034030. arXiv: 1512.03583 [hep-ph].

[98] Y.-H. Chen et al. "Effects of Z_b states and bottom meson loops on $\Upsilon(4S) \to \Upsilon(1S, 2S)\pi^+\pi^-$ transitions". In: *Phys. Rev. D* 95.3 (2017), p. 034022. DOI: 10.1103/PhysRevD.95.034022. arXiv: 1611.00913 [hep-ph].

[99] V. Baru et al. "Insights into $Z_b(10610)$ and $Z_b(10650)$ from dipion transitions from $\Upsilon(10860)$". In: *Phys. Rev. D* 103.3 (2021), p. 034016. DOI: 10.1103/PhysRevD.103.034016. arXiv: 2012.05034 [hep-ph].

[100] D. A. S. Molnar, I. Danilkin, and M. Vanderhaeghen. "The role of charged exotic states in $e^+e^- \to \psi(2S)\ \pi^+\pi^-$". In: *Phys. Lett. B* 797 (2019), p. 134851. DOI: 10.1016/j.physletb.2019.134851. arXiv: 1903.08458 [hep-ph].

[101] I. Danilkin, D. A. S. Molnar, and M. Vanderhaeghen.
"Simultaneous description of the $e^+e^- \to J/\psi\,\pi\pi\,(K\bar{K})$ processes".
In: *Phys. Rev. D* 102.1 (2020), p. 016019.
DOI: 10.1103/PhysRevD.102.016019. arXiv: 2004.13499 [hep-ph].

[102] M. Ablikim et al. "Measurement of $e^+e^- \to \pi^0\pi^0\psi(3686)$ at $\sqrt{s}$ from 4.009 to 4.600 GeV and observation of a neutral charmoniumlike structure".
In: *Phys. Rev. D* 97.5 (2018), p. 052001.
DOI: 10.1103/PhysRevD.97.052001. arXiv: 1710.10740 [hep-ex].

[103] S.-R. Xue et al. "Disentangling the role of the $Y(4260)$ in $e^+e^- \to D^*\bar{D}^*$ and $D_s^*\bar{D}_s^*$ via line shape studies". In: *Phys. Lett. B* 779 (2018), pp. 402–408.
DOI: 10.1016/j.physletb.2018.02.027. arXiv: 1708.06961 [hep-ph].

[104] F.-Z. Peng et al. "Light- and heavy-quark symmetries and the Y(4230), Y(4360), Y(4500), Y(4620), and X(4630) resonances".
In: *Phys. Rev. D* 107.1 (2023), p. 016001.
DOI: 10.1103/PhysRevD.107.016001. arXiv: 2205.13590 [hep-ph].

[105] T. Ji et al. "Prediction of a Narrow Exotic Hadronic State with Quantum Numbers JPC=0–". In: *Phys. Rev. Lett.* 129.10 (2022), p. 102002.
DOI: 10.1103/PhysRevLett.129.102002. arXiv: 2205.10994 [hep-ph].

[106] L. von Detten, C. Hanhart, and V. Baru. "The Y(4230) as a D1D molecule".
In: *EPJ Web Conf.* 291 (2024), p. 03006.
DOI: 10.1051/epjconf/202429103006. arXiv: 2309.11970 [hep-ph].

[107] S. X. Nakamura et al. "Global coupled-channel analysis of $e^+e^- \to c\bar{c}$ processes in $\sqrt{s} = 3.75 - 4.7$ GeV". In: (Dec. 2023).
arXiv: 2312.17658 [hep-ph].

[108] D.-Y. Chen, X. Liu, and T. Matsuki. "Interference effect as resonance killer of newly observed charmoniumlike states $Y(4320)$ and $Y(4390)$".
In: *Eur. Phys. J. C* 78.2 (2018), p. 136.
DOI: 10.1140/epjc/s10052-018-5635-1. arXiv: 1708.01954 [hep-ph].

[109] V. Baru et al. "Interplay of quark and meson degrees of freedom in a near-threshold resonance". In: *Eur. Phys. J. A* 44 (2010), pp. 93–103.
DOI: 10.1140/epja/i2010-10929-7. arXiv: 1001.0369 [hep-ph].

[110] V. Baru et al.
"Effective range expansion for narrow near-threshold resonances".
In: *Phys. Lett. B* 833 (2022), p. 137290.
DOI: 10.1016/j.physletb.2022.137290. arXiv: 2110.07484 [hep-ph].

[111] F. E. Close and E. S. Swanson.
"Dynamics and decay of heavy-light hadrons".
In: *Phys. Rev. D* 72 (2005), p. 094004. DOI: 10.1103/PhysRevD.72.094004.
arXiv: hep-ph/0505206.

[112] Z. Q. Liu et al. "Study of $e^+e^-ß\pi^+\pi^- J/\psi$ and Observation of a Charged Charmoniumlike State at Belle". In: *Phys. Rev. Lett.* 110 (2013). [Erratum: Phys.Rev.Lett. 111, 019901 (2013)], p. 252002.
DOI: 10.1103/PhysRevLett.110.252002. arXiv: 1304.0121 [hep-ex].

[113] K. Chilikin et al. "Observation of a new charged charmoniumlike state in $\bar{B}^0ßJ/\psi K^-\pi^+$ decays". In: *Phys. Rev. D* 90.11 (2014), p. 112009.
DOI: 10.1103/PhysRevD.90.112009. arXiv: 1408.6457 [hep-ex].

[114] M. Ablikim et al. "Observation of a Charged Charmoniumlike Structure in $e^+e^- \to \pi^+\pi^- J/\psi$ at $\sqrt{s}$ =4.26 GeV".
In: *Phys. Rev. Lett.* 110 (2013), p. 252001.
DOI: 10.1103/PhysRevLett.110.252001. arXiv: 1303.5949 [hep-ex].

[115] M. Ablikim et al. "Observation of $Z_c(3900)^0$ in $e^+e^- \to \pi^0\pi^0 J/\psi$".
In: *Phys. Rev. Lett.* 115.11 (2015), p. 112003.
DOI: 10.1103/PhysRevLett.115.112003. arXiv: 1506.06018 [hep-ex].

[116] W. Chen et al.
"Mass spectra of Zc and Zb exotic states as hadron molecules".
In: *Phys. Rev. D* 92.5 (2015), p. 054002.
DOI: 10.1103/PhysRevD.92.054002. arXiv: 1505.05619 [hep-ph].

[117] A. E. Bondar et al. "Heavy quark spin structure in Z_b resonances".
In: *Phys. Rev. D* 84 (2011), p. 054010. DOI: 10.1103/PhysRevD.84.054010.
arXiv: 1105.4473 [hep-ph].

[118] Y.-H. Chen, M.-L. Du, and F.-K. Guo.
"Precise determination of the pole position of the exotic $Z_c(3900)$".
In: (Oct. 2023). arXiv: 2310.15965 [hep-ph].

[119] M. Bayar et al. "Triangle Singularities in the $\Lambda_b \to J/\Psi K^- p$ Reaction".
In: *PoS* Hadron2017 (2018), p. 133. DOI: 10.22323/1.310.0133.

[120] S. Coleman and R. E. Norton. "Singularities in the physical region".
In: *Nuovo Cim.* 38 (1965), pp. 438–442. DOI: 10.1007/BF02750472.

[121] M. Ablikim et al. "Observation of Three Charmoniumlike States with JPC=1– in e+e-→D*0D*-π+". In: *Phys. Rev. Lett.* 130.12 (2023), p. 121901.
DOI: 10.1103/PhysRevLett.130.121901. arXiv: 2301.07321 [hep-ex].

[122] Z.-Y. Zhou, C.-Y. Li, and Z. Xiao. "A new look at $\psi(4160)$ and $\psi(4230)$".
In: (Apr. 2023). arXiv: 2304.07052 [hep-ph].

[123] J. T. Daub, C. Hanhart, and B. Kubis.
"A model-independent analysis of final-state interactions in $\overline{B}^0_{d/s} \to J/\psi\pi\pi$".
In: *JHEP* 02 (2016), p. 009. DOI: 10.1007/JHEP02(2016)009.
arXiv: 1508.06841 [hep-ph].

[124] S. Ropertz, C. Hanhart, and B. Kubis.
"A new parametrization for the scalar pion form factors".
In: *Eur. Phys. J. C* 78.12 (2018), p. 1000.
DOI: 10.1140/epjc/s10052-018-6416-6. arXiv: 1809.06867 [hep-ph].

[125] Y.-H. Chen et al. "Nature of the $Y(4260)$: A light-quark perspective".
In: *Phys. Rev. D* 99.7 (2019), p. 074016.
DOI: 10.1103/PhysRevD.99.074016. arXiv: 1902.10957 [hep-ph].

[126] T. Mannel and R. Urech. "Hadronic decays of excited heavy quarkonia".
In: *Z. Phys. C* 73 (1997), pp. 541–546. DOI: 10.1007/s002880050344.
arXiv: hep-ph/9510406.

[127] Q. Wang, C. Hanhart, and Q. Zhao.
"Systematic study of the singularity mechanism in heavy quarkonium decays".
In: *Phys. Lett. B* 725.1-3 (2013), pp. 106–110.
DOI: 10.1016/j.physletb.2013.06.049. arXiv: 1305.1997 [hep-ph].

[128] K. M. Watson.
"The Effect of final state interactions on reaction cross-sections".
In: *Phys. Rev.* 88 (1952), pp. 1163–1171. DOI: 10.1103/PhysRev.88.1163.

[129] X. Zhang et al. "Remarks on non-perturbative three–body dynamics and its application to the $KK\bar{K}$ system". In: *Eur. Phys. J. A* 58.2 (2022), p. 20.
DOI: 10.1140/epja/s10050-021-00661-y. arXiv: 2107.03168 [hep-ph].

[130] V. Baru et al. "Emergence of heavy quark spin symmetry breaking in heavy quarkonium decays". In: *Phys. Rev. D* 107.1 (2023), p. 014027.
DOI: 10.1103/PhysRevD.107.014027. arXiv: 2211.08038 [hep-ph].

[131] C. Hanhart, A. Sibirtsev, and J. Speth.
"The Reaction pi N —> omega N revisited: The omega-N scattering length".
In: (July 2001). arXiv: hep-ph/0107245.

[132] F.-K. Guo et al. "Production of the X(3872) in charmonia radiative decays".
In: *Phys. Lett. B* 725 (2013), pp. 127–133.
DOI: 10.1016/j.physletb.2013.06.053. arXiv: 1306.3096 [hep-ph].

[133] M. Ablikim et al. "Confirmation of a charged charmoniumlike state $Z_c(3885)^\mp$ in $e^+e^- \to \pi^\pm(D\bar{D}^*)^\mp$ with double D tag".
In: *Phys. Rev. D* 92.9 (2015), p. 092006.
DOI: 10.1103/PhysRevD.92.092006. arXiv: 1509.01398 [hep-ex].

[134] M. Ablikim et al. "Determination of the Spin and Parity of the $Z_c(3900)$". In: *Phys. Rev. Lett.* 119.7 (2017), p. 072001. DOI: 10.1103/PhysRevLett.119.072001. arXiv: 1706.04100 [hep-ex].

[135] X. Li and M. B. Voloshin. "Suppression of the S-wave production of $(3/2)^+ + (1/2)^-$ heavy meson pairs in e^+e^- annihilation". In: *Phys. Rev. D* 88.3 (2013), p. 034012. DOI: 10.1103/PhysRevD.88.034012. arXiv: 1307.1072 [hep-ph].

[136] F.-K. Guo et al. "Could the near-threshold XYZ states be simply kinematic effects?" In: *Phys. Rev. D* 91.5 (2015), p. 051504. DOI: 10.1103/PhysRevD.91.051504. arXiv: 1411.5584 [hep-ph].

[137] M. Cleven and Q. Zhao. "Cross section line shape of $e^+e^- \to \chi_{c0}\omega$ around the $Y(4260)$ mass region". In: *Phys. Lett. B* 768 (2017), pp. 52–56. DOI: 10.1016/j.physletb.2017.02.041. arXiv: 1611.04408 [hep-ph].

[138] F.-K. Guo et al. "Reconciling the X(4630) with the Y(4660)". In: *Phys. Rev. D* 82 (2010), p. 094008. DOI: 10.1103/PhysRevD.82.094008. arXiv: 1005.2055 [hep-ph].

[139] F. .-. Guo et al. "Interplay of quark and meson degrees of freedom in near-threshold states: A practical parametrization for line shapes". In: *Phys. Rev. D* 93.7 (2016), p. 074031. DOI: 10.1103/PhysRevD.93.074031. arXiv: 1602.00940 [hep-ph].

[140] Q. Wang et al. "Line shapes of the $Z_b(10610)$ and $Z_b(10650)$ in the elastic and inelastic channels revisited". In: *Phys. Rev. D* 98.7 (2018), p. 074023. DOI: 10.1103/PhysRevD.98.074023. arXiv: 1805.07453 [hep-ph].

[141] V. Baru et al. "Spin partners W_{bJ} from the line shapes of the $Z_b(10610)$ and $Z_b(10650)$". In: *Phys. Rev. D* 99.9 (2019), p. 094013. DOI: 10.1103/PhysRevD.99.094013. arXiv: 1901.10319 [hep-ph].

[142] L. C. Biedenharn, J. D. Louck, and P. A. Carruthers. *Angular Momentum in Quantum Physics: Theory and Application.* Encyclopedia of Mathematics and its Applications. Cambridge University Press, 1984. DOI: 10.1017/CBO9780511759888.

[143] S. Ohkoda et al. "Decays and productions via bottomonium for Z_b resonances and other $B\bar{B}$ molecules". In: *Phys. Rev. D* 86 (2012), p. 117502. DOI: 10.1103/PhysRevD.86.117502. arXiv: 1210.3170 [hep-ph].

[144] C. W. Xiao, J. Nieves, and E. Oset.
"Combining heavy quark spin and local hidden gauge symmetries in the dynamical generation of hidden charm baryons".
In: *Phys. Rev. D* 88 (2013), p. 056012. DOI: 10.1103/PhysRevD.88.056012.
arXiv: 1304.5368 [hep-ph].

[145] V. Baru et al.
"Heavy-quark spin symmetry partners of the X (3872) revisited".
In: *Phys. Lett. B* 763 (2016), pp. 20–28.
DOI: 10.1016/j.physletb.2016.10.008. arXiv: 1605.09649 [hep-ph].

[146] V. Baru et al. "Spin partners of the Z_b (10610) and Z_b (10650) revisited".
In: *JHEP* 06 (2017), p. 158. DOI: 10.1007/JHEP06(2017)158.
arXiv: 1704.07332 [hep-ph].

[147] L. D. Faddeev. "Scattering theory for a three particle system".
In: *Zh. Eksp. Teor. Fiz.* 39 (1960), pp. 1459–1467.

[148] E. Byckling and K. Kajantie. *Particle Kinematics: (Chapters I-VI, X).*
Jyvaskyla, Finland: University of Jyvaskyla, 1971.

[149] W. H. Press et al.
Numerical Recipes in FORTRAN 77: The Art of Scientific Computing.
2nd ed. Cambridge University Press, Sept. 1992. ISBN: 052143064X.

[150] M. Mikhasenko et al. "Dalitz-plot decomposition for three-body decays".
In: *Phys. Rev. D* 101.3 (2020), p. 034033.
DOI: 10.1103/PhysRevD.101.034033. arXiv: 1910.04566 [hep-ph].

[151] S. U. Chung. "SPIN FORMALISMS". In: (Mar. 1971).
DOI: 10.5170/CERN-1971-008.

[152] S. M. Berman and M. Jacob. "SYSTEMATICS OF ANGULAR POLARIZATION DISTRIBUTIONS IN THREE-BODY DECAYS".
In: *Phys. Rev.* 139 (1965), B1023–B1038.
DOI: 10.1103/PhysRev.139.B1023.